Fusion Based Automatic Segmentation of Brain Tumour from MRI Images

A thesis submitted in fulfilment of the requirements

for the degree of

Doctor of Philosophy

in the Faculty of Engineering,

University of Calicut

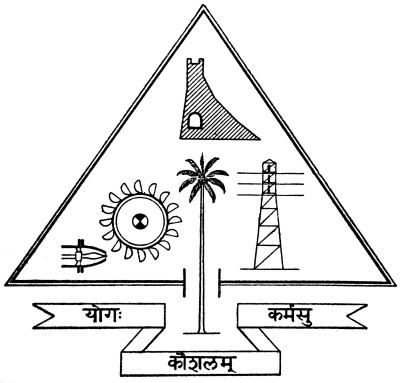

by

Maya U.C

Under the Guidance of

Dr.K. Meenakshy

Department of Electrical and Electronics Engineering

Govt. Engineering College, Thrissur

University of Calicut

August 2019

Certificate

This is to certify that the thesis entitled **Fusion Based Automatic Segmentation of Brain Tumour from MRI Images** is the record of bonafide research work done by **Ms.Maya U.C** under my supervision and guidance at Department of Electrical and Electronics Engineering, Govt. Engineering College, Thrissur in partial fulfilment of the requirement for the Degree of Doctor of Philosophy under Faculty of Engineering, University of Calicut.

Dr.K.Meenakshy
Professor(NC)
Dept. of Electrical and Electronics Engg.
Govt. Engineering College, Thrissur

August, 2019

The suggestions / corrections from the adjudicators as per Ref.No.159464/ RESEARCH-C-ASST-1/2019/Admn Dated 03-01-2020 from the Director of Research, University of Calicut, have been incorporated in this thesis.

Dr.K.Meenakshy
Professor(NC)
Dept. of Electrical and Electronics Engg.
Govt. Engineering College, Thrissur

February 2020

Declaration

I, MAYA U.C., declare that this thesis titled, 'Fusion Based Automatic Segmentation of Brain Tumour from MRI Images' and the work presented in it are my own. I confirm that:

- This work was done wholly or mainly while in candidature for a research degree at this University.
- Where any part of this thesis has previously been submitted for a degree or any other qualification at this University or any other institution, this has been clearly stated.
- Where I have consulted the published work of others, this is always clearly attributed.
- Where I have quoted from the work of others, the source is always given. With the exception of such quotations, this thesis is entirely my own work.
- I have acknowledged all main sources of help.
- Where the thesis is based on work done by myself jointly with others, I have made clear exactly what was done by others and what I have contributed myself.

Signed:

August 2019

Abstract

Name of the student: **Maya U.C**

Degree for which submitted: **Ph.D**

Department: **Electrical and Electronics Engineering**

Thesis title: **Fusion Based Automatic Segmentation of Brain Tumour from MRI Images**

Thesis supervisor: **Dr. K. Meenakshy**

Month and year of thesis submission: **August 2019**

A brain tumour is an unmanageable growth of brain cells causing the formation of masses of tissues inside the rigid skull. Visually analysing the tumour affected brain MRI will not provide much information regarding the disease. Analysis using image processing techniques will aid the diagnosis process. Segmentation of tumour and its related sub-regions from the MRI is a challenging task. Literature survey reveals that classification based techniques are more suitable than contour based techniques for this segmentation, as the size and shape of tumour are unpredictable. Hierarchical Agglomerative Clustering (HAC) based classifier is developed in this work to automatically segment the tumour and its related sub-regions from MRI. This classifier uses a set of features which include a newly developed Multi Spectral Pattern based Texture Features (MSPTF) and conventional features. MSPTF is derived from a fusion of four different MRI modalities. The conventional features considered are GLCM, GLRLM, GLDM, LTP, LBP, Laws texture energy, FPS and

SMRT. From this exhaustive feature set, optimized features are identified. The developed HAC based classifier incorporates optimization along with segmentation. A refinement technique, which improves the result of segmentation from HAC classifier is also developed. This is based on the knowledge of the pattern of occurrences of the tumour and its subregions. The data for the study is taken from BraTS 2015, BraTS 2016 data sets, Govt. Medical College, Thrissur and Lakeshore Hospital, Cochin. The efficiency of the developed method was compared with the state of the art methods and showed promising results.

Acknowledgements

First and above all, I bow my head before the **Almighty** Lord whose grace has been with me always throughout the research work.

I would like to express my wholehearted gratitude to my supervising guide, **Dr. K. Meenakshy**, Professor, Department of Electrical and Electronics Engineering, Govt. Engineering College, Thrissur, for her valuable guidance, understanding, support and most importantly her friendly relationship during the whole period of research. I also acknowledge her patience and guidance during the documentation process.

I would like to place on record my gratitude to The Director, Department of Higher Education, Govt. of Kerala for giving me an opportunity to do research on full time basis and for providing the research scholarship.

I would like to express my gratitude to **Dr.K.P.Indira Devi**, Director, Department of Technical Education for providing facilities to successfully carry out this research. My sincere thanks to **Dr.Sheeba V.S.**, The Principal, Government Engineering College, Thrissur, also the internal Doctoral Committee member for her valuable suggestions and support. I am grateful to **Prof. (Dr.) R.Gopikakumari**, Professor, Division of Electronics Engineering, School of Engineering, Cochin University of Science and Technology (CUSAT), for her valuable guidance as the external Doctoral Committee member.

I must express my gratitude to **Dr. P. Reji**, Head of the Department, Electrical and Electronics Engineering, Government Engineering College, Thrissur, for her support. I also thank all the faculty members, technical staff in Electrical and Electronics Engineering Department. I also thank all office staff of Government Engineering College Thrissur, for their help during the period of research.

I would like to thank **Dr.B.Jayanand**, Professor, Department of Electrical Engineering, Government Engineering College, Thrissur and **Dr.M. Nandakumar**, Former Head, Department of Electrical and Electronics Engineering, for providing valuable comments and suggestions at the time of interim presentations of research work.

I express my sincere gratitude to all the faculties and technical staff of the Department of Computer Engineering, Govt. Polytechnic College, Chelakkara for their support and encouragement. I extend my gratitude to **Prof.B.Manju**, Associate Professor, Department of Electrical Engineering for providing timely help. I also thank my fellow researchers, **Dr. Benzy V.K.**, **Mr. R. Anilkumar**, **Mrs. Remya George**, **Mrs. Shwetha C.**, **Mrs. Jeeva K.A.** and **Mrs. Renukadevi V**. for their support, encouragement, timely help and suggestions.

I gratefully acknowledge the efforts put by **Dr. Jinu C.S**, Radiologist, Hindlab MRI Scan Center, Govt. Medical College, Thrissur and **Dr. Thara Prathap**, Dept. of Radiology, Lakeshore Hospital, Cochin for providing data and other details.

I am highly indebted to my **Parents and in-laws** for their support. I thank my husband **Mr. Subhash Raghuram S.** for the consistent encouragement and absolute support. I also thank my daughter **Aditi Subhash** and my son **Avyukt Subhash** for patiently co-operating with me to complete the work successfully.

Thrissur

Maya U.C

August 2019

Contents

List of Figures

List of Tables

Abbreviations

ANN	**A**rtificial **N**eural **N**etwork
BPN	**B**ack **P**ropagation **N**etwork
CNN	**C**onvolution **N**eural **N**etwork
CNS	**C**entral **N**ervous **S**ystem
CSF	**C**erebro **S**pinal **F**luid
CT	**C**omputed **T**omography
DNN	**D**eep **N**eural **N**etwork
DV	**D**istance **V**ector
EDV	**E**xtended **D**istance **V**ector
ET	**E**nhancing **T**umour
FCM	**F**uzzy **C** **M**eans
FLAIR	**FL**uid **A**ttenuated **I**nversion **R**ecovery
FN	**F**alse **N**egative
FP	**F**alse **P**ositive
FPS	**F**ourier **P**ower **S**pectrum
GA	**G**enetic **A**lgorithm
GLCM	**G**ray **L**evel **C**o-occurrence **M**atrix
GLDM	**G**ray **L**evel **D**ifference **M**atrix
GLRLM	**G**ray **L**evel **R**un **L**ength **M**atrix
GM	**G**ray **M**atter
HAC	**H**ierarchical **A**gglomerative **C**lustering
KNN	**K** **N**earest **N**eighbour

LBP	**L**ocal **B**inary **P**attern
LTP	**L**ocal **T**ernary **P**attern
MSPTF	**M**ulti **S**pectral **P**attern based **T**exture **F**eature
MRI	**M**agnetic **R**esonance **I**maging
NET	**N**on **E**nhancing **T**umour
NC	**N**ecrotic **C**ore
PSO	**P**article **S**warm **O**ptimization
PTBE	**P**eri **T**umoural **B**rain **E**dema
RF	**R**adio **F**requency
ROI	**R**egion **O**f **I**nterest
SMRT	**S**equency **M**apped **R**eal **T**ransform
SVM	**S**upport **V**ector **M**achine
TE	**E**cho **T**ime
TN	**T**rue **N**egative
TP	**T**rue **P**ositive
TR	**R**epetition **T**ime
WM	**W**hite **M**atter
WSS	**W**rong **S**equence **S**earch

Dedicated to My Teachers...

Chapter 1

Introduction

1.1 Human Brain

The most complex organ in the human body is the brain. It is made up of more than 100 billion nerves and trillions of interconnections called synapses for communication.

The brain is divided into several lobes

1. The frontal lobes are responsible for problem solving, judgement and motor function.
2. The parietal lobes manage sensation, handwriting, and body position.
3. The temporal lobes are involved with memory and hearing.
4. The occipital lobes contain the brain's visual processing system.

The brain is surrounded by a layer of tissue called meninges. The skull (cranium) helps to protect the brain from injury [1]. Fig. 1.1 shows the different lobes of human brain [1]. Brain tumour is one of the most common brain disorder. It is found to be more common in children than adults [2].

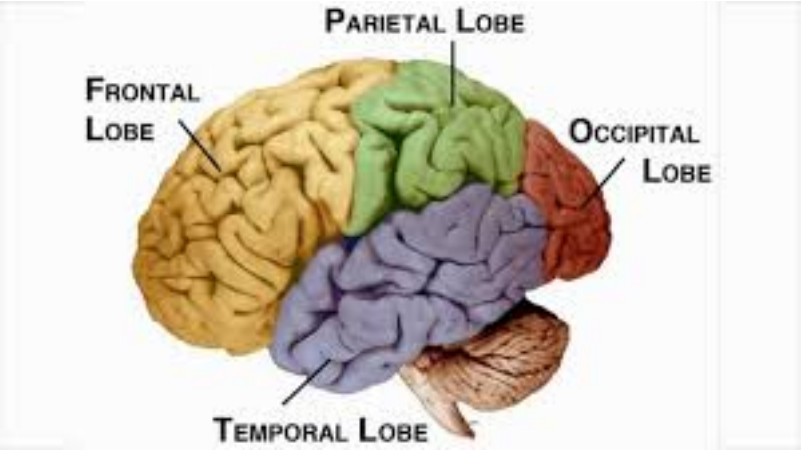

FIG. 1.1. Different Lobes of Human Brain

1.2 Brain Tumour

A Brain Tumour is an unmanageable growth of brain cells causing the formation of masses of tissue inside the rigid skull. A brain tumour can be malignant (cancerous) or benign (non-cancerous). Unlike any other body part, a benign tumour in brain may cause trouble if it is located in an important functional part of the brain. Cancerous tumour cells ignore signals that instruct cells to stop dividing and influence the normal cells, molecules, and blood vessels that surround and feed a tumour which is otherwise known as the micro-environment [3]. Another classification of brain tumour is primary brain tumour (originates in the brain or nearby tissues) and secondary brain tumour (originates elsewhere and spread to brain).

1.2.1 Brain Tumour Diagnosis

The diagnosis of brain tumour starts from analysing the symptoms of the patient. Most common symptoms include recurrent headache, seizure, vision problem, etc. But they may vary from person to person. At this stage the person with suspected brain tumour undergoes medical diagnosis.

Nowadays imaging techniques are an unavoidable part of medical diagnosis. Imaging modalities that are most common in brain imaging are Computed Tomography (CT) and Magnetic Resonance Imaging (MRI). Both these techniques are explained in detail in the following sections.

1.3 Computed Tomography

Compared to MRI, CT takes less time and it is suitable for imaging hard tissues.

1.3.1 Working Principle

Unlike conventional X-ray imaging which uses a fixed X-ray tube as a source and a film at the other end for constructing the image, Computed Tomography uses X-ray tubes that rotates around the patient, shooting narrow beams of X-ray through the body. CT scanners use special digital X-ray detectors that are placed directly opposite to the source. A 2-D image slice of the patient is generated using complex mathematical equation after the X-ray source completes one full rotation. The thickness of the tissue in 2-D slice depends on the CT machine and usually it varies from 1 to 10 millimeters. After a full rotation of the X-ray tube and 2-D image construction, the motorized bed is moved incrementally into the gantry and the process is repeated. After the complete scan, 2-D images can be stacked together to form a 3-D image [4]. Fig. 1.2 is a CT scanner [5].

FIG. 1.2. CT Scanner

The generation of 2-D image slices and reconstruction of the 3-D image from 2-D slices is based on the Fourier Slice Theorem, which states that the Fourier Transform of the projection of an N-D function onto an M-D linear submanifold is equal to M-D slice of N-D Fourier Transform of that function. The tomographic reconstruction process becomes a series of one dimensional Fourier Transform followed by a two dimensional Inverse Fourier Transform [6].

1.3.2 Drawbacks of CT

During CT scan, patient is exposed to harmful ionizing radiation. CT scans can have 100 to 1000 times higher dose of radiation than conventional X-ray. Radiation in CT damages the cells including DNA. Studies reveal that exposure to radiation as a major cause of cancer especially in children.

CT is good in imaging hard tissues. A CT scan is particularly useful when imaging complex fractures, severely eroded joints or bone tumours. Soft tissues have low ability in stopping X-rays. Thus a CT scanner generates a low quality image while imaging soft tissues especially the brain tissues. In such cases intravenous contrast agents are used which contain elements that are helpful in stopping X-rays. In some patients, contrast agent may cause allergic reactions and in rare cases it causes temporary kidney failure [7].

1.4 Magnetic Resonance Imaging

MRI is a strong tool in examining the human body. Strong magnetic fields and radio waves are used in MRI scanners. Usually the magnetic power used in MRI scanners vary from 1.5 Tesla to 7 Tesla. Unlike other common imaging techniques, during MRI scan the subject is not exposed to harmful radiations. This makes MRI a better choice in medical imaging.

1.4.1 Basic Principle of MRI

The most abundant atom in the human body is hydrogen because a normal human body contains around 60% of water and 20% of fat and both water and fat consist of hydrogen atoms. An atom consists of a nucleus and electrons orbiting around the nucleus. The basic principle of MRI relies on the spinning motion of nuclei present in biological tissues [8]. In an atom, half of the nucleons (protons + neutrons) spin in one direction and another half in opposite direction. Thus the nuclei of atoms with even atomic number has no net spin due to the cancellation of the forces of rotation. Atoms with odd atomic numbers are known as MR-Active because the

forces of rotation of nucleons does not cancel out and they have a net spin. MRI scanner makes use of the highly abundant MR-Active hydrogen nuclei in the human body. Randomly oriented magnetic moments of hydrogen nuclei gets aligned when a strong external magnetic field (B_0) is applied.

Larmor frequency of a nucleus is the natural frequency of its magnetic moment. A nucleus gains energy from an external source only when the oscillation of that source is equal to the larmor frequency of the nucleus. The transmit coil in MRI scanner transmits RF excitation pulse and hydrogen nuclei gets the energy since its larmor frequency is in RF band. RF excitation pulse produces an oscillating magnetic field B_1 which is very weak compared to B_0 [8]. When RF excitation pulse is stopped the nuclei in high energy return to their previous stage by releasing energy. The receiving coil in the MRI machine captures that energy to generate images. An MRI-scanner is shown in Fig. 1.3 [9] .

FIG. 1.3. MRI Scanner

1.4.2 MRI Planes

In the anatomical position, X-axis would go from front to back, Y-axis from left to right and Z-axis from top to bottom. Fig. 1.4 shows different axes of the anatomical position [10] .

According to the anatomical position, an MRI scanning can be carried out in axial/transverse plane or coronal plane or sagittal plane. The three planes are shown in Fig. 1.5 [10].

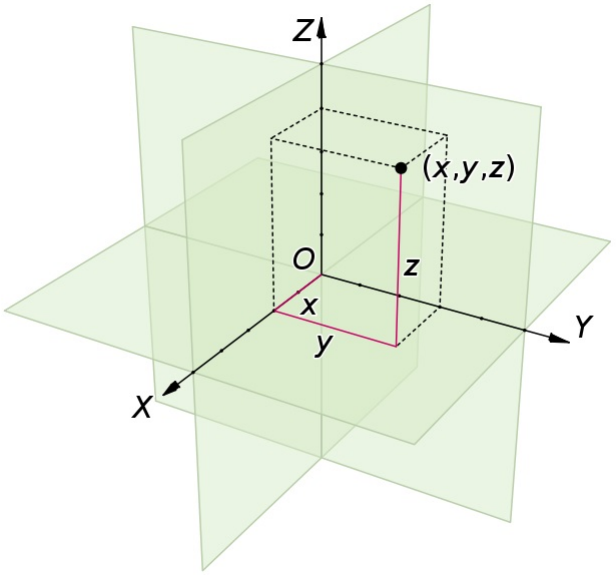

FIG. 1.4. Cartesian Coordinates of Anatomical Position

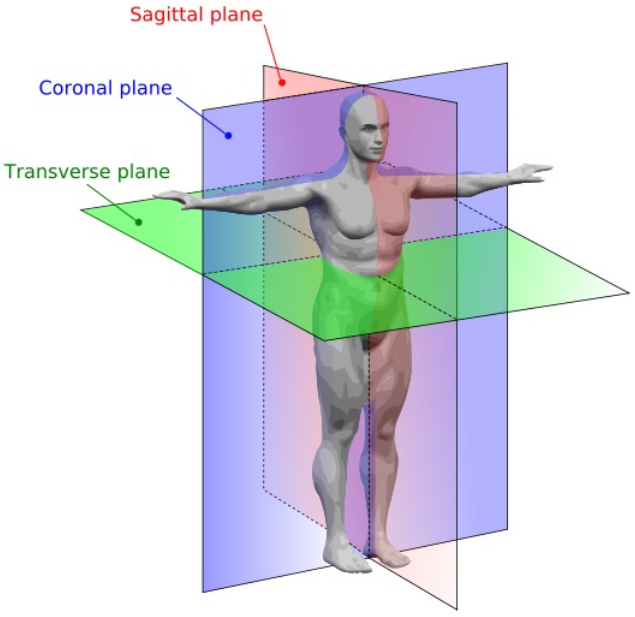

FIG. 1.5. MRI Planes

1.4.3 Different MRI Modalities

The contrast of the MRI image depends on many parameters which can be broadly classified as intrinsic and extrinsic. Intrinsic parameters such as T1 recovery time and T2 decay time cannot be changed since they are inherent to body's tissue. Extrinsic parameters can be varied to obtain different MRI modalities.

RF pulse timing parameters comes under extrinsic category. There are two RF pulse timing parameters, Repetition Time (TR) and Echo Time (TE).

TR is the time gap between the application of two consecutive RF excitation pulses. It is usually measured in milliseconds.

TE is the time from the application of RF excitation pulse to the peak of the signal induced in the coil. Like TR, TE is also measured in milliseconds.

Different MRI modalities can be obtained by varying RF pulse timing parameters. In T2 weighted MRI modality, the water contents are made brighter than fatty parts by keeping TE long enough. But in T1 weighted sequence, the reverse happens by using shorter TE and TR [8]. T1 weighted imaging can also be performed with the help of paramagnetic contrast enhancement agents. Most widely used agent is Gadolinium (Gad). Gad enhanced T1 weighted images are especially useful in looking at vascular structures and breakdown in the blood-brain barrier. Another commonly used MRI modality is Fluid Attenuated Inversion Recovery (FLAIR). In FLAIR, brighter abnormalities and Cerebro Spinal Fluid (CSF) suppression are achieved by selecting a much longer TE and TR [11].

Most commonly used TR and TE values for T1 weighted, T2 weighted and FLAIR MRI are shown in Table 1.1. The contrast variations of different components of brain in various MRI modalities are summed up in Table 1.2.

MRI images, using the above mentioned four modalities of a tumour affected brain are shown in Fig. 1.6

TABLE 1.1: Most Common MRI Modalities and Their Approximate TR and TE Times

	TR (ms)	**TE (ms)**
T1 Weighted (Short TR and TE)	**500**	**14**
T2 Weighted (Long TR and TE)	**4000**	**90**
FLAIR (Very long TR and TE)	**9000**	**114**

TABLE 1.2: Contrast of Various Brain Tissues in Different MRI Modalities

Tissue	**T1 Weighted**	**T2 Weighted**	**FLAIR**
CSF	Dark	Bright	Dark
Fat	Bright	Light	Light
Inflammation /Infection	Dark	Bright	Bright

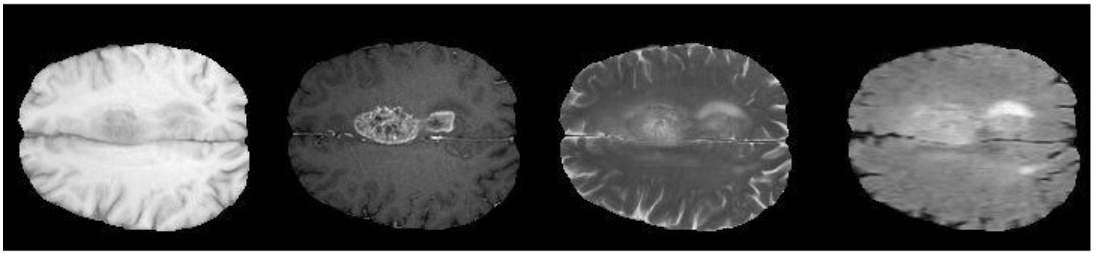

FIG. 1.6. T1, T1 Contrast, T2 and FLAIR MRI of a Tumour Affected Brain

1.5 Tumour Affected Brain MRI

Although initial diagnosis of a brain tumour starts from the analysis of symptoms, detection of the suspected tumour is done with the aid of imaging techniques. High contrast in soft tissues and non-invasive characteristics make MRI a better choice for brain tumour diagnosis than CT scan [12].

The presence of abnormality and its vague location can be viewed using MRI image. But the exact spread area or contours and different components are not much visible to the naked eye. Despite the histological differences, most of the brain

tumours are associated with a PeriTumoural Brain Edema (PTBE), which is a primary reason for the patient's mortality [13]. Water flow disturbances in the brain, especially from blood vessels into the parenchyma, causes edema [14]. These blood vessels show blood-tumour barrier that is different from the blood-brain barrier in the healthy brain [15]. A tumour affected brain may have developed a necrosis which consists of the dead cells. Two common forms of cell deaths are encountered in biology: apoptosis (i.e., programmed cell death) and necrosis (i.e., accidental cell death). In a tumour affected brain, the presence of necrosis is an important diagnostic feature, and clinical studies indicate that as the degree of necrosis advances, the patient's prognosis worsens [16]. Tumour affected brain has regions of cells that are in a quiescent state and areas where cells proliferate rapidly. The decision of a cell to become quiescent or proliferating depend on both nutrient and oxygen availability and on an element produced by necrotic cells that somehow inhibits the further growth of the tumor [17]. Isolating all these sub-regions in a tumour affected MRI have apparent clinical relevance [18]. Locating and segmenting complete tumour and its various sub-regions has an enormous impact on the treatment planning as well as monitoring the effectiveness of treatment. Various sub-regions of the tumour affected brain MRI are shown in Fig. 1.7.

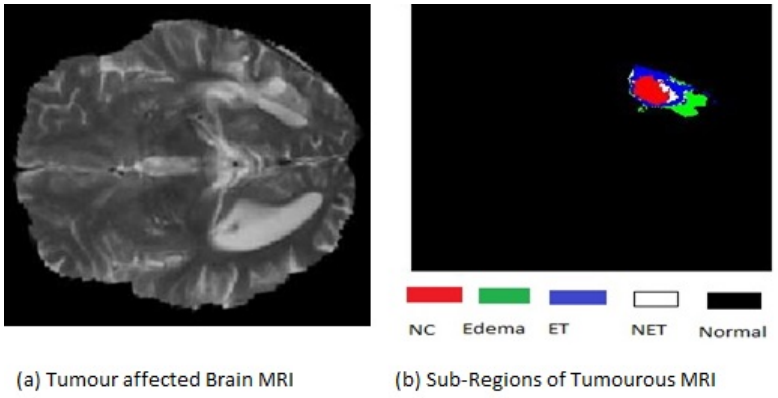

FIG. 1.7. The Sub-Regions Present in a Tumour Affected Brain MRI

Different sub-regions present in a tumour affected brain MRI image are listed below.

- Normal
- Edema

- Necrotic Core (NC)
- Enhancing Tumour (ET)
- Non Enhancing Tumour (NET)

Edema, NC, ET and NET together form the complete tumour. NC, ET and NET together is known as Tumour Core. ET is otherwise called active tumour.

The proper segmentation of these parts contributes a lot in brain tumour treatment plan and after treatment monitoring. An automated segmentation aids the physician in the decision making process.

1.6 Segmentation

Segmentation of an image is the process of isolating a Region Of Interest (ROI) from other parts of the image. Segmentation can be done manually with much accuracy if the contours of the part to be segmented is sharp and visible to the naked eye. But in the case of images with vague or invisible contours, manual segmentation is not an easy task. In such cases contour based or model based segmentation techniques may work well if we have an idea about the size or shape or both of the area to be segmented. But if both are unknown there is a high probability of contour based technique to become a failure in segmentation. Classification techniques can be applied to segment the required region/regions in such cases [19].

1.7 Motivation

Irrespective of the grade, a tumour in brain may cause death if its not treated properly. Even a benign tumour may become hazardous if it lies in the vital part of brain. Unlike malignant tumours, benign tumours do not spread into nearby tissues. But contradictory to benign tumours elsewhere in the body, a benign tumour in the brain can be life-threatening since it grows inside the rigid skull.

Literature shows that among many cancers, brain cancer (malignant brain tumour) has a low survival rate [20]. The rate of survival depends on many factors including how fast and accurate the diagnosis and treatment planning processes are. All the treatment may go in vain if the location of the tumour is not identified properly. Locating and segmenting the tumour and associated sub-regions are important for a successful diagnosis and after treatment monitoring [21]. Segmentation of tumour in an affected brain MRI is considered as a challenging job because of the unpredictability of tumour shape and size.

The worldwide cancer statistics reveals that brain and nervous system cancers constitute 1.8% (17^{th} position in the list of most common cancers) of total cancer incidence [20]. However, due to several reasons, the survival rate of Central Nervous System (CNS) cancer is meagre compared to other common cancers. Fig. 1.8 shows the five-year net survival rate of different types of cancers [22].

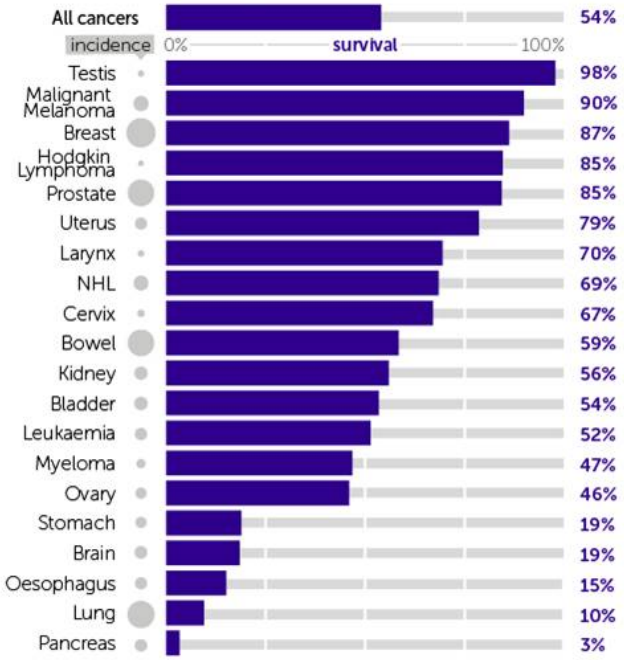

FIG. 1.8. Survival Rate of Different Types of Cancers

A faster and accurate diagnosis and a proper treatment plan ensures the improvement in survival rate. International Brain Tumour Segmentation (BraTS) challenge is organised every year since 2012. In 2018, Section for Biomedical Image Analysis (SBIA) of Perelman school of medicine under the university of Pennsylvania with Center for Biomedical Image Computing and Analytic (CBICA) conducted

the challenge. Automating the segmentation of the tumour and its related sub-regions make the treatment planning fast and after treatment monitoring process effortless.

1.8 Objectives of the Thesis

The main objectives of the current study are

1. Extraction of a new set of features from multiple modality of tumour affected brain MRI that provide a better classification of sub-regions of tumour.
2. Development of a new algorithm for the segmentation of tumour and related sub-regions in an affected brain MRI through classification.
3. Comparison of the developed technique with state of the art techniques.

1.9 Organization of Thesis

The Thesis is organized in seven chapters as given below.

- **Chapter 1** introduces brain and brain tumour. Different brain imaging techniques are discussed. An introduction to image segmentation is presented. The chapter ends with the motivation behind the thesis, objectives of the work and organization of various chapters.
- **Chapter 2** presents an exhaustive literature survey carried out on different image segmentation methods and various available brain tumour segmentation techniques, revealing the research potential in the field of brain tumour segmentation.
- **Chapter 3** describes all the tools used to carry out the study. Various feature extraction tools, feature selection tools and classification tools are discussed in detail in this chapter.

- **Chapter 4** focuses on the development of a new feature extraction technique called Multi-Spectral Pattern based Feature Extraction (MSPTF). The features are extracted from a fusion of multiple MRI modalities. The distance vector of a pixel is initially estimated considering different modalities. These distance vectors are then encoded and converted into features. Comparison of the developed features with conventional features is also included in this chapter.

- **Chapter 5** discusses the segmentation of brain tumour from MRI through a classification based method. A new algorithm for combined feature selection and multi-class classification based on Hierarchical Agglomerative Clustering (HAC) is described in detail. The results obtained using the developed algorithm is compared with the results obtained using state of the art methods.

- **Chapter 6** discusses a refinement technique applied to the developed HAC based segmentation method. It is based on the pattern of appearance of tumour and its sub-regions in an affected brain MRI. The basis of the refinement is wrong sequence identification. The probability of misclassification is estimated and corrections are incorporated if necessary. The advantage of refinement is also discussed in this chapter. Qualitative results obtained during the segmentation process are presented in this chapter. Comparison of the developed technique with state of the art methods are also carried out.

- **Chapter 7** depicts the summary and conclusion of the work. The major research contributions and scope for further work in this area are also presented.

A complete framework of the thesis is shown in Fig. 1.9.

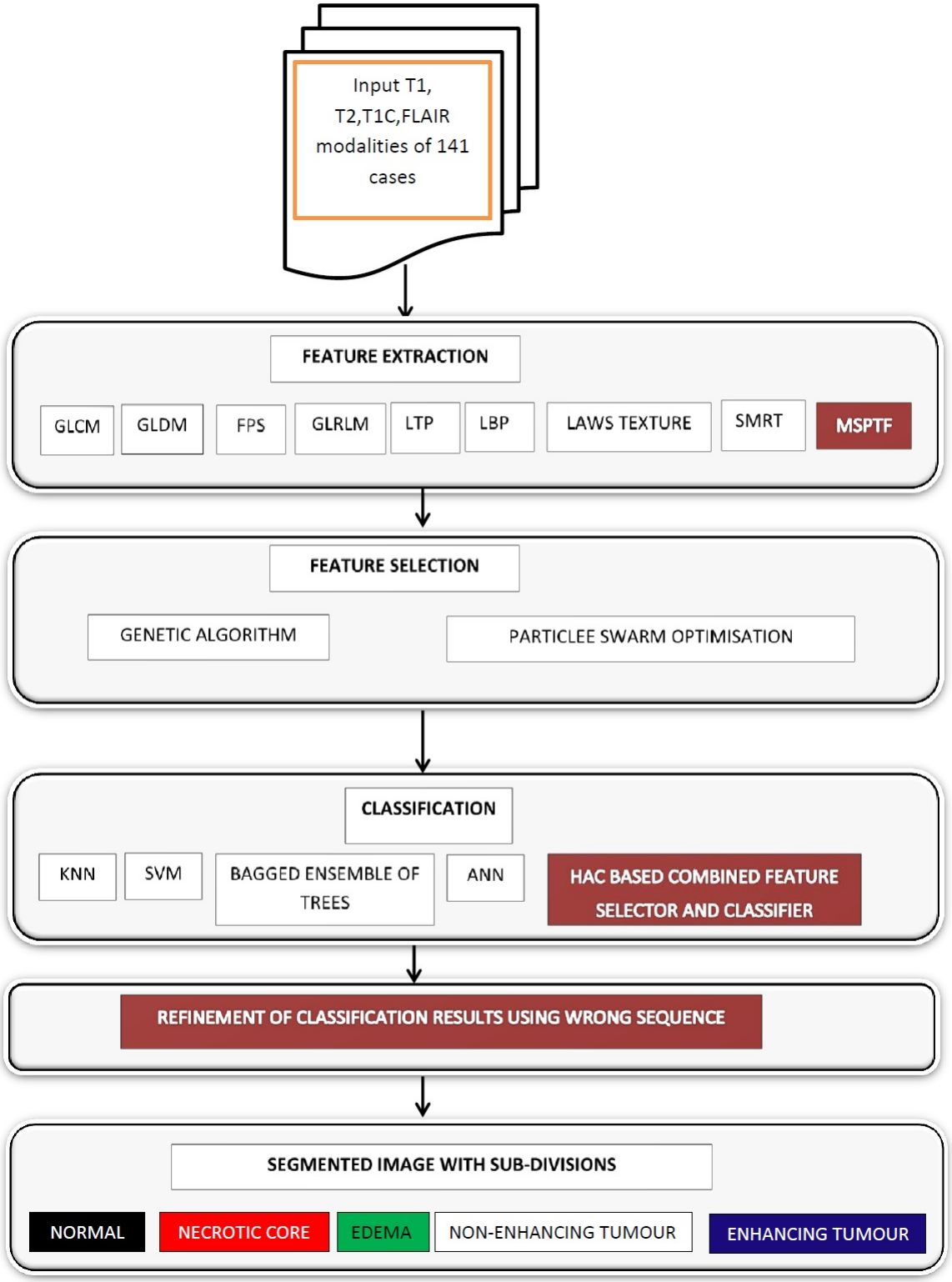

FIG. 1.9. Framework of the Thesis

Chapter 2

Literature Review

2.1 Brain Tumour Segmentation

Isolating different components or substructures present in a tumour affected MRI image is a tedious process, and currently, physicians depend on their experience as well as visual system to achieve the solution. The findings may vary from person to person, and there exist chances of disagreement too. Also, the data provided by MRI is huge so that it is not practical to process it manually. The recent advances in image processing techniques can be used to make the segmentation task semi-automatic or fully-automatic, which simplifies the job of the physicians and makes segmentation results faster and more accurate. Many image processing techniques were proposed to make segmentation automatic. Some methods use a single modality whereas a few use multiple modalities of MRI. The existing methods for tumour segmentation can be broadly categorised as edge/contour-based segmentation and classification based segmentation. Other common methods include atlas-based method, region growing segmentation technique, etc. Some segmentation techniques are hybrid which employ a group of different techniques to get the segmentation results [19].

2.1.1 Edge/Contour Based Segmentation

In this particular category of segmentation technique, various edge detection and contour finding algorithms are applied to differentiate various substructures of a tumour affected MRI.

The method proposed by Mbuyamba *et al.* [23] is a 2 stage segmentation process. In the first stage, the region of interest containing abnormality is localised using the proposed Hierarchical Centroid Shape Descriptor (HCSD). In the second stage, delineation of tumour area was done using a newly proposed Localised Active Contour Model with Background Intensity Compensation (LACM-BIC). The experiments were conducted in BraTS 2012 dataset, and only the tumour substructure was segmented with a dice score of 0.91. Edema and other components were not extracted in this method.

Based on the observation that certain contour-based methods are apt for segmenting a particular subset of MRI images, an automatic selection of a contour technique among five different contour techniques were implemented for tumour segmentation in Mbuyamba *et al.* [24]. The active contour methods involved were implicit active contours driven by Local Binary Fitting Energy (LBF) [25], active contours driven by Local Gaussian Distribution Fitting (LGDF) energy [26], contours based on Local Mean Separation Energy (LMS) [27], localized Chan-Vese (C-V) [27] and Localized Active Contour Model with Background Intensity Compensation (LACM-BIC) [24]. The results show that the automatic selection of active contour method achieved a Dice-Score of 0.93 for tumour region which is better than individual active contour techniques involved in the selection procedure.

Unlike the traditional active contour or snake, which uses a deterministic iterative method for optimisation, Mbuyamba *et al.* [28] used Cuckoo Search (CS) for optimisation. The proposed Multi-population Cuckoo Search Strategy (MCSS) uses a Pizza-slice Shaped Search Windows (PSSW). The experiment started with a noise removal with median filter and edge detection using canny filter as preprocessing steps. The proposed method was compared with multi-population Particle Swarm Optimization Search (MPSOS) with PSSW, MPSOS with Rectangular Shaped Search Windows (RSSW), MCSS with RSSW and traditional active contour method. Analysis of results shows that the proposed method achieved a Dice-Score

of 0.95 in segmenting tumour from MRI image which is better than other techniques used for comparison.

Rajinikanth *et al.* [29] proposed a new method integrating Teaching Learning Based Optimization (TLBO), entropy function based multi-level thresholding and active contour-based segmentation. Kapur's entropy function, Shannon's function and Tsallis entropy are the three entropy functions involved in this study. Finally, the segmentation is done using active contour method.

The experimental result shows that combination of Shannon's entropy based thresholding and level set segmentation offers better result for the considered dataset.

Hamamci *et al.* [30] in his proposed Tumour Cut algorithm used Cellular Automata (CA) for segmenting tumour region from enhanced T1 weighted brain MRI image. The method is semi-automatic which starts with user drawing longest diameter of a visible tumour. After determining tumour and normal seed points, CA is run twice. One for the tumour and other for the background to calculate tumour strength and background strength respectively. The two strengths are then combined to get tumour probability map. The surface having probability at least 0.5 is the tumour surface. The authors used three different datasets. Synthetic datasets of simulated tumours from the University of Utah, Harvard Brain Tumor Repository and brain tumor datasets obtained from clinical Radiation Oncology site. The analysis of results show that the method got a dice overlap percentage of 82.6 with a standard deviation of 17.3 in the synthetic dataset. In Harvard Brain Tumour Repository the technique performed better with a dice overlap percentage of 89.3 with a standard deviation of 6.9. In clinical radiation oncology dataset, the dice overlap percentage was 80.1 with 6.9 standard deviation. The analysis also shows that the result depends on the selection of the initial seed line.

Shanthakumar and Ganeshkumar [31] proposed a Fluid Vector Flow (FVF) active contour model for tumour segmentation. After pre-processing with anisotropic filtering, GLCM features and texture features using laws energy were extracted. ANFIS classifier is used to test the malignancy. If it is found to be malignant, the method tries to segment the tumour area using region growing method. The seed point selection is made automatic and depends on the appearance of the tumour. The proposed method achieved a similarity index of 0.8 approximately.

The segmentation process proposed by Kanas *et al.* [32] used two significant steps. In the first step, outliers were detected using clustering technique. K- means clustering with euclidean distance metric is used to cluster healthy tissues into Gray Matter (GM), White Matter (WM) and Cerebro Spinal Fluid (CSF). With the help of a threshold value, abnormalities were detected as samples that are distant to all three cluster centres. The false positives after the first stage were reduced in the second stage which uses a graph-based algorithm called random walker proposed by Grady [33]. Authors improved the work by expanding the analysis from 2D to 3D [34]. The proposed method goes through all the steps in the previous work. The 2D random walker is expanded to 3D random walker. The analysis of results shows that the method could segment the tumour with a Dice-Score of 0.81 whereas non-enhancing tumour region and edema region was segmented with a Dice-Score of 0.75. Enhancing tumour region got an average Dice-Score of 0.72.

A threshold-based scheme that uses level sets (TLS) for 3D tumour segmentation was used by Taheri *et al.* [35] in their work. To form speed function, a global threshold was used. The initial threshold was calculated using the level set initialization which then iteratively updated throughout the process of segmentation. Upon reaching the tumour boundary, the variation of the threshold declines because of the contrast between tumour and non-tumour intensities. This method highly depends on the intensity variation between tumorous and non-tumorous regions.

Nie *et al.* [36] proposed a new segmentation method called Spatial accuracy-weighted Hidden markov random field and Expectation maximisation (SHE) to segment tumorous region from multi-sequence MRI. SHE is executed in skull-stripped images.

Contour-based and region based segmentation techniques were combined in Khotanlou *et al.* [37]. The algorithm uses T1 weighted MRI sequence. Removal of non-brain data which may include fat, muscle, skull etc. is the first step in the segmentation process. A combination of histogram analysis, morphological operations and symmetry analysis was performed in the first step. The initial tumour segmentation was performed using a Fuzzy Possibilistic C-Means (FPCM) method or symmetry analysis and some morphological operations. Fuzzy classification assumes that the intensity in tumour region varies from that of the normal region. On the other hand, symmetry analysis assumes that a normal brain MRI has a plane of

symmetry. The refinement in the segmentation is done with the help of a parametric deformable model which is constrained by spatial relations. An average similarity index of 0.92 is obtained by this method.

2.1.2 Classification Based Segmentation

This category is characterised by the usage of one or more supervised or unsupervised classifiers which in turn labels different substructures of the brain MRI image.

Pereira *et al.* [38] proposed an automatic brain tumour segmentation method based on Convolutional Neural Network (CNN). They used relatively small kernel size of 3 x 3, leading to a deeper architecture. A pre-processing by intensity normalization is done in this method. Data augmentation with rotation and regularization is conducted to reduce the problem of overfitting. The work uses BraTS 2013 and 2015 database which consists of four MRI modalities, T1 weighted, T1 with Gad enhancement, T2 weighted and FLAIR. The evaluation measures used are Positive Predictive Value (PPV), Dice-Score and Sensitivity. In BraTS 2013 data set, they achieved a Dice-Score of 0.84 for the complete tumour (Edema+ET+NET+NC), 0.72 for Core (ET+NET+NC) and 0.62 for ET. In BraTS 2015 data set, this method achieved a Dice-Score of 0.78, 0.65 and 0.75 in Complete, Core and enhanced regions respectively. Comparing BraTS 2013 and 2015 data sets, only the enhancing region showed an improved result. Although this method ranked in the first position in 2013 BraTS challenge and second in 2015 challenge, there still exist gaps for improvement.

The multi fractal features proposed by Islam *et al.* [39] uses Support Vector Machine (SVM) and a modified AdaBoost algorithm. T1, T2 and FLAIR MRI modalities of 14 patients were considered for the study. The pre-processing stage includes realignment and unwrapping of slices within a volume and co-registering of other modalities with T1 modality. For pre-processing, SPM8 toolbox was used. Along with the proposed multi fractal texture features, piece-wise-triangular-prism-surface-area (PTPSA) fractal features were also used. The results show that with intensity features and proposed multi fractal features, they could achieve the highest Dice-Score of 0.83. But the False Positive Fraction was less when intensity features and proposed features used along with PTPSA features.

The method proposed by Reza and Iftekharuddin [40] starts with intensity normalization. Extracted features include intensities of all modalities, textural features using fractal PTPSA, texton features and mutifractional Brownian motion (mBm) features. The classifier used was Random Forest. Although this method achieved a Dice-Score of 0.908 for Tumour Core and 0.8 for Edema during training, the testing results were very poor for both Tumour Core (0.43) and Edema (0.42).

The method proposed by Cabria and Gondra [41] uses the fusion of 3 segmentation algorithms. The proposed Potential Field Segmentation (PFS), combination of region growing segmentation with electrostatic force clustering for seed initialization and Potential Field Clustering (PFC) are the three segmentation techniques used in this work. Also fusion of these methods were done using set intersection method and set union method. The proposed method is experimented with publicly available BraTS database. Analysis of results are done using the segmentation quality measure, Q, which is defined as the percentage of pixels in agreement with the ground truth segmentation. An average Q value of 0.612 is obtained using PFS alone. Also, the results obtained using union and intersection of the three segmentation methods were much less than PFS results.

T1 weighted MRI images were pre-processed with five variations of Principle Component Analysis (PCA) in Kaya *et al.* [42]. Box filtering is done as the pre-processing step. The PCA processed images were then clustered using K-means algorithm and Fuzzy C-Means clustering algorithm (FCM). Five most common PCA algorithms: namely the conventional PCA, Probabilistic Principal Component Analysis (PPCA), Expectation Maximization based Principal Component Analysis (EM-PCA), Generalizde Hebbian Algorithm (GHA), and Adaptive Principal Component Extraction (APEX) were applied to reduce dimensionality in advance of two clustering algorithms. The result analysis was done based on reconstruction error. The analysis phase shows that PPCA and EMPCA returned better results, and in most cases, FCM outperformed K-Means algorithm.

Comparison of the effectiveness of statistical features and wavelet features in brain tumour segmentation is carried out in Nabizadeh and Kubat [43]. Detecting the slice having tumour followed by statistical and wavelet feature extraction is done in the first phase. 475 statistical features and 81000 wavelet features were then reduced with the help of Principal Component Analysis (PCA). Various classifiers

were employed to compare the effectiveness of statistical and wavelet features extracted. Two different MRI modalities – T1 weighted and FLAIR – were separately processed in this study. The results show that for every classifier, statistical features outperformed wavelet features in classifying tumour and normal regions.

Li *et al.* [44] presents a probabilistic model of multi-modal MR brain tumour segmentation. This model combines sparse representation and the Markov Random Field (MRF) to solve the spatial and structural variability problem. With the help of sparse representation and MRF maximum, a priori is calculated which is then transformed into a minimum energy optimization. The graph cuts are used to approximately solve the minimum energy optimization via finding the minimum cuts in a graph model. The experiment used BraTS 2013 data set. The result analysis shows that complete tumour got a dice score of above 0.8 for both low grade and high grade. But the Dice-Score of tumour core and enhancing tumour is approximately 0.56, which is considered as a poor result.

Vishnuvarthanan *et al.* [45] proposed a clustering based segmentation scheme, which uses two major algorithms ie Self Organizing Map (SOM) and Fuzzy K-Means Clustering (FKM) proposed by Chang *et al.* [46]. Removal of skull region is done using Brain Extraction Tool (BET) as specified in Smith [47] in the pre-processing stage. For an initial clustering and dimensionality reduction, SOM is employed. The final clustering is done using FKM. The method got a dice overlap index of 0.47.

To make use of 3-D information in MRI scan, Abbasi and Tajeripour [48] proposed two new features such as Local Binary Pattern in Three Orthogonal Plane (LBP-TOP) and Histogram Orientation Gradients in Three Orthogonal Plane (HOG-TOP). Dataset used was BraTS 2013. In the first stage of pre-processing, bias field correction is done using N4ITK [49]. In the second stage of pre-processing, intensity scale of each sequence was normalized by a histogram matching algorithm implemented in ITK [50]. To extract Region of Interest (ROI), Otsu thresholding [51] is applied to FLAIR image. Gray level intensity, HOG-TOP and LBP-TOP features are extracted in 3-D MRI and the classification is done using random forest. Bagging is used as the ensemble method. The proposed method gave a Dice-Score of 0.83 for Complete Tumour, 0.75 for Tumour Core and 0.76 for enhancing tumour.

Havaei *et al.* [52] uses a Deep Neural Network (DNN) in BraTS 2013 dataset. Unlike the traditional Convolutional Neural Network (CNN), DNN exploits both local features as well as global contextual features simultaneously using two pathway architecture. DNN processes patches of size 4 x 33 x 33 to find the label of mid pixel in the patch. To speed up the process, DNN uses a convolutional implementation of a fully connected layer as final layer. Due to the misproportion of data (Normal pixel will be much higher than affected ones), training procedure is done in two phases. The proposed architecture was a cascaded architecture, which concatenates both global pathway and local pathway. Three concatenation methods were used. The first model, InputCascadeCNN, took 3 minutes on average, whereas the two other models, MFCascadeCNN model and LocalCascadeCNN model, took 1.5 minutes and 1.7 minutes respectively. Analysis of results shows that InputCascadeCNN worked better for Complete Tumour, Tumour Core and enhancing tumour with a Dice-Score of 0.88, 0.79 and 0.73 respectively.

Local Independent Projection-based Classification (LIPC) based segmentation proposed by Huang *et al.* [53] segments the whole MRI image using pixel by pixel classification strategy. LIPC algorithm has three major steps of dictionary construction, locally linear representation, and classification score computation. In the preprocessing step, image inhomogeneity correction and intensity normalization has been performed. The method does not extract second order statistical features, rather they considered a square patch surrounding a voxel which is rearranged as a feature vector. After passing through the LIPC algorithm, a final step of post-processing using connected component algorithm and mathematical morphology is used to refine the classified edema regions. BraTS 2012 and BraTS 2013 data sets are used for the study and the method achieved average Dice-Score of 0.84, 0.685, and 0.585 in segmenting Complete Tumour, Tumour Core, and enhancing tumour respectively on real patient data.

Ain *et al.* [54] proposed a combined brain tumour detection and segmentation framework. Datasets of different patients from Holy Family hospital and Abrar MRI and CT Scan Center, Rawalpindi was used for the study. The process starts with noise removal using Fast Discrete Curvelet Transform (FDCT) [55]. First-order histogram based features and second order texture features using Gray Level Co-occurrence Matrix (GLCM) are extracted from the noise removed image. Using

SVM as base classifier, an ensemble classifier is used to classify the image into normal or affected. If the image is found to be tumour affected, the segmentation of the tumour region is done using FCM clustering after skull stripping.

In Wang *et al.* [56], instead of using the traditional distance metrics, local and non-local informations were used to measure the distance in FCM clustering, which in effect will decide the membership value in each cluster. Although a single qualitative result is presented for tumour segmentation which does not provide an improvement from the standard FCM visually, the proposed method overweighed other variations of FCM in segmenting White Matter (WM), Gray Matter (GM) and Cerebro Spinal Fluid (CSF) with similarity indices of 0.92, 0.90 and 0.90 respectively.

Harati *et al.* [57] in their proposed method used an improved Fuzzy Connectedness (FC) algorithm to segment the brain tumour from Spoiled Gradient Recalled Acquisition (SPRG) and post gad T1 MRI image. Noise removal is done using anisotropic diffusion filter as head mask. In addition to intensity feature and homogeneity, a tumour detection matrix is defined for automatic seed selection. General fuzzy connectedness algorithm loses its path in the weak boundaries. The improved version of FC algorithm tries to improve the robustness over the boundaries by entering appropriate gradient information to the affinity function. The method achieved a similarity index of 0.92 in segmenting the tumour.

Cai *et al.* [58] used T1 weighted images, FLAIR, contrast enhanced T1 weighted MRI, Diffusion Weighted Images (DWI) and two scalar maps computed from the Diffusion Tensor Imaging (DTI). In preprocessing stage, skull stripping, co-registration with T1 images and gaussian smoothing are done. The intensity features of all the sequences are combined to form a feature vector. An intra-patient classifier and inter-patient classifier is built based on SVM.

The tumour segmentation method proposed by Clark *et al.* [59] uses T1 weighted, T2 weighted and proton density modalities of MRI. The system starts with clustering the slice using FCM. The clustered slice is then passed to the knowledge-based system. The knowledge about the intensities of different tissues in various sequence and expected shapes and placements of certain tissues within the MRI are included in knowledge base. From the initial clustering an intra cranial mask is created. Using adaptive histogram threshold, an initial segmentation of tumour is performed. Final

refinement on the segmentation is done using a density screening in feature space. Results show that although it could achieve a good percent match, it contained a large value of false positives.

Sheela and Suganthi [60] uses greedy snake model in their work. Pre-processing involves the identification of approximate ROI through morphological operations. In the second stage, mask formation is done using threshold. Using the initial contours given by mask, greedy snake model estimates new boundaries. The remaining inaccurate boundaries are estimated using FCM. Only T1 weighted modalities were used to conduct the experiments and sub-regions of the complete tumour are not segmented. The dice score for complete tumour is less than 0.78.

2.1.3 Segmentation Based on Other Methods

In literature some other methods are also employed to segment a tumour affected brain MRI. These methods include atlas based methods, graph cut method etc.

Prastawa *et al.* [61] isolated tumour and edema using an atlas based method. They used T1 weighted MRI and T2 weighted MRI sequences. The segmentation framework consists of three stages. In the initial stage, the abnormalities (tumour+edema) and its vague location in the given image are identified using a registered brain atlas of a healthy brain. In the second stage, edema region is filtered out from the entire abnormality using intensity features using thresholding. In the third stage, reclassification is done to improve the results with the assumption that each edema region is connected to a nearby tumour region. In this method, data set used was limited to three and validation is done using VALMET segmentation validation tool. A Jaccard Score of approximately .77 for tumour and .68 for edema is obtained.

The method proposed by Gooya *et al.* [62] uses a healthy brain atlas modified by a glioma growth model. The modified atlas is then registered into patients space for obtaining posterior probability of tissue labels. It also makes use of expectation maximization algorithm. T1, T1 contrast-enhanced image, T2 and FLAIR modalities were used for each case. In preprocessing step, inhomogeneity correction, skull stripping and cerebellum removal were done. The four sequences are co-registered

with an affine registration algorithm. The co-registered images are then registered with atlas space. Dice Score obtained for tumour and edema are 0.84 and 0.76 respectively.

The efficiency of four different sets of features in segmenting posterior fossa tumour was estimated by Ahmed *et al.* [63]. The feature extraction was done on intensity normalized and bias corrected MRI images. T1, T2 and FLAIR modalities were used. Intensity features, Texture features using Fractal Dimension (FD), level set based shape features and mBm texture features were used for the study. For feature selection Principle Feature Analysis (PFA), Kullback–Leibler Divergence (KLD) and newly proposed Boost Feature Subset Selection (BFSS) methods were employed. Graph cut and expectation maximization algorithms are the segmentation techniques used by this work.

The hybrid method proposed by Ramakrishnan and Sankaragomathi [64] involves a classifier as well as a region growing method. Classifier classifies the image into either tumour affected or non-tumourous. Region growing technique is applied in tumour images to segment the affected region. Computed Tomography (CT) images are employed for experimental purpose. Histogram equalization is done as the pre-processing step. GLCM features, maximum intensity feature and Local Gabor XOR Pattern (LGXP)features were extracted which is given as input to the classifier. SVM classifier is then employed for classification with a linear kernel and sequential minimum optimization. In segmentation stage, Modified Region Growing (MRG) with threshold optimization is employed. The whole image is divided into grids. Seed point and threshold are selected. In threshold selection procedure, Gray Wolf Optimization (GWO), Evolutionary Program (EP) and Harmony Search (HS) were conducted. Out of these three, GWO gave better results. An average sensitivity of 0.88 for tumour is achieved through this work.

To deal with unclear tumour boundaries, GLCM based Cellular Automata (GLCM-CA) is presented in Sompong and Wongthanavasu [65], which is a semi-automatic technique. The method has two stages. In the initial stage transformation of an original MRI to the featured image is done. The features of the tumour area which are similar to the background area are enhanced by this transformation. An Improved Tumour-Cut (ITC) algorithm Hamamci *et al.* [30] is used for segmentation. In ITC a novel patch weighted distance is proposed to deal with the problem of

robustness in seed growing. Publicly available BraTS 2013 data set was used for experiments. In testing phase, the method obtained a Dice-Score of 0.79 for Tumour Core and 0.84 for whole tumour.

Two popular clustering methods, K-Means and FCM are combined and a new method called K-means Integrated with Fuzzy C-means (KIFCM) is proposed in [66] to achieve the time efficiency of K- Means and accuracy efficiency of FCM. Authors used three different data sets for the experiment. The first set consists of .jpeg images where as the second and third includes multi modality MR images. Skull removal and denoising using the median filter is done as pre-processing operations. KIFCM clustering is done next. Thresholding, filtering and level set contouring is done sequentially in the final stage to get the segmentation results. The experiments were conducted in BraTS 2012 data set. T1 contrast enhanced modality is used for high-grade tumour. T2 weighted modality is used for low-grade and FLAIR modality for edema segmentations in both low grade and high grade. A non-parametric model distribution of intensity of normal region is estimated. Using this model, normal region is separated from the affected one. Edema is separated using another model created using FLAIR modality. An average Dice- Score of 0.875 and 0.83 is obtained as tumour and edema segmentation results respectively.

An enhanced Particle Swarm Optimization (PSO) is used by Vijay *et al.* [67] to segment tumour parts from MRI. Histogram-based gravitational optimization algorithm (HGOA) for brain lesion segmentation proposed by Nabizadeh *et al.* [68] uses DWI modality for stroke lesion segmentation and T1 weighted sequence for tumour lesion segmentation. HGOA is based on brain histogram analysis and an enhanced gravitational optimization algorithm. The method make use of intensity features only. HGOA has 2 main steps. The first step called histogram based brain segmentation algorithm, starts with intensity histogram calculation and smoothing the histogram using local weighted averaging technique. This algorithm segments the entire image into 'n' number of segments where 'n' is the number of local maxima of smoothed histogram. In the second step, N-dimensional Gravitational Optimization Algorithm (NGOA) is applied to the result of step1 to make the number of segments as desired. In the post-processing step Consistency Verification (CV) algorithm is executed in order to reduce false positives. The method could achieve an accuracy of 0.88 in segmenting tumour lesion.

Corso *et al.* [69] combines model-based classification technique and an extension of weighted aggregation technique for tumour segmentation. The original graph-based Segmentation by Weighted Aggregation (SWA) algorithm is extended to integrate model aware affinities. Results show that the method achieved a Jaccard Score of 0.69 in segmenting tumour and 0.62 in segmenting edema.

Rough FCM (RFCM) and shape based properties are used in Bal *et al.* [70]. Skull stripping is done as pre-processing step. The new centroid selection method for FCM reduces the execution time of RFCM. Fuzzy membership handles overlapping and uncertainty in data are handled by upper and lower bounds of rough set. The experiments were conducted on a limited number of data. The work concentrated on segmenting the Complete Tumour.

The method proposed by Ma *et al.* [71] is a hybrid technique in which initial segmentation is done through random forest classifier and the final refinement is done using multi-scale patch driven active contours. The work used multiple modalities and obtained a Dice-Score of 0.89, 0.80 and 0.76 for Complete Tumour, Tumour Core and enhancing tumour respectively.

Symmetry analysis and fast bounding box algorithm is employed to detect the tumour location in the method proposed by Kermi *et al.* [72]. The slice in which the largest bounding box was detected is selected as slice of interest. Region growing and geodesic level set methods are used for the final segmentation. The sub-regions were not segmented separately.

Tang *et al.* [73] used a multi-atlas method. Normal brain atlases are used to register label information. In the first step a normal brain image is recovered from tumorous MRI using a new low rank method. Registration of normal brain atlas to the recovered image is carried out in the next step. Both these steps were continued until convergence.

A summary of the reviewed literature is presented in Table 2.1.

TABLE 2.1: Literature Review Summary

AUTHOR	METHOD	MODALITIES	RESULT
Mbuyamba *et al.* [23]	HCSD + LACM-BIC	T1C, T2	Complete Tumour Dice-Score=0.91
Mbuyamba *et al.* [24]	Automatic Selection of Active Contour	NA	Complete Tumour Dice-Score=0.93
Mbuyamba *et al.* [28]	MCSS + PSSW + RSSW	T1	Complete Tumour Dice-Score=0.95
Rajinikanth *et al.* [29]	TLBO + Active Contour	FLAIR, T1C, T2	Complete Tumour Dice-Score=0.94
Hamamci *et al.* [30]	Tumour Cut using CA	T1C	Complete Tumour Dice-Score=0.84
Shanthakumar and Ganeshkumar [31]	FVF Active Contour	NA	Complete Tumour Similarity Index=0.81
Kanas *et al.* [34]	K-Means + 3-D Random Walker	T1, T2, T1C, FLAIR	DS (Complete Tumour =0.81, Edema=0.75,ET=0.72)
Taheri *et al.* [35]	TLS	T1, T1C	Jaccards Measure of Complete Tumour =0.87
Nie *et al.* [36]	SHE	T1, T1C, FLAIR, T2	Jaccards Measure of Complete Tumour =0.87
Khotanlou *et al.* [37]	FPCM + Parametric Deformable Model	T1	Similarity Index of Complete Tumour =0.92
Pereira *et al.* [38]	CNN	T1, T1C, T2,FLAIR	DS (Complete Tumour =0.84,Tumour Core = 0.72, ET=0.62)
Cabria and Gondra [41]	PFS	T1,T2	Q value of Complete Tumour=0.612

TABLE 2.1: Literature Review Summary

AUTHOR	METHOD	MODALITIES	RESULT
Kaya *et al.* [42]	5 types of PCA + K-Means	T1	Reconstruction Error Rate=1.14
Nabizadeh and Kubat [43]	wavelet features + PCA + SVM	T1,FLAIR	Accuracy of Complete Tumour=0.9
Li *et al.* [44]	Sparse Representation + MRF	T1, T2, T1C, FLAIR	DS (Complete Tumour=0.84, Tumour Core=0.54, ET=0.57)
Vishnuvarthanan *et al.* [45]	SOM+FKM	T1, T2, T1C, FLAIR	Dice Overlap Index of Complete Tumour=47%
Abbasi and Tajeripour [48]	LBP-TOP + HOG-TOP + Bagged ensemble of Trees	T1, T2, T1C, FLAIR	DS (Complete Tumour=0.83, Tumour Core=0.75, ET=0.76)
Havaei *et al.* [52]	DNN	T1, T2, T1C, FLAIR	DS (Complete Tumour=0.88, Tumour Core=0.79, ET=0.73)
Huang *et al.* [53]	LIPC	T1, T2, T1C, FLAIR	DS (Complete Tumour=0.84, Tumour Core=0.685, ET=0.585)
Ain *et al.* [54]	SVM ensemble +FCM	NA	NA
Harati *et al.* [57]	Improved Fuzzy Connectedness	T1C	Similarity Index of Complete Tumour=0.92
Cai *et al.* [58]	Quadratic Discriminant Analysis+SVM	T1C,T1, Diffusion weighted, FLAIR, DTI	Accuracy (Edema=0.98, ET=0.96, NET=0.96)
Clark *et al.* [59]	FCM+ Knowledge based System	T1,T2, Proton Density	Average Percentage match > 90

TABLE 2.1: Literature Review Summary

AUTHOR	METHOD	MODALITIES	RESULT
Sheela and Suganthi [60]	FCM+ Greedy Snake	T1	DS of Complete Tumour=0.78
Prastawa *et al.* [61]	Atlas Based Method	T1,T2	Jaccard Score (Complete Tumour=0.77, edema=0.68)
Gooya *et al.* [62]	Glioma growth model + healthy brain atlas	T1,T2, FLAIR, T1C	Jaccard Score (Complete Tumour=0.84, edema=0.76)
Ahmed *et al.* [63]	BFSS+Graph Cut+ Expectation Maximization	T1,T2, FLAIR	Jaccard Score of Complete Tumour=0.6
Ramakrishnan and Sankaragomathi [64]	SVM + MRG +GWO	CT images	Sensitivity of Complete Tumour=0.88
Sompong and Wongthanavasu [65]	GLCM – CA + ITC	T1,T2, FLAIR, T1C	DS (Complete Tumour=0.84, Tumour Core=0.79)
Abdel-Maksoud *et al.* [66]	KFCM + Contouring	T1,T2, FLAIR	DS (Complete Tumour=0.875, Edema=0.83)
Nabizadeh *et al.* [68]	HGOA + NGOA + CV	T1	Accuracy of Complete Tumour=0.88
Corso *et al.* [69]	Model based SWA	T1, T1C, T2, FLAIR	Jaccard Score (Complete Tumour=0.69, Edema=0.62
Ma *et al.* [71]	Random Forest + Active Contour	T1, T1C, T2, FLAIR	DS (Complete Tumour=0.89, Tumour Core=0.80, ET=0.76)
Kermi *et al.* [72]	Symmetry Analysis + Region Growing + Geodesic Levelset	T2, FLAIR	Sensitivity of Complete Tumour=(0.81 for T2 and 0.89 for FLAIR)

The literature review disclose the fact that classification/clustering based segmentation perform better for the segmentation of MRI images. From the exhaustive literature review performed, the following observations were drawn.

- Majority of classification/clustering based segmentation studies have considered only single modality MRI images from among the available modalities such as T1,T2,T1C,FLAIR.
- The studies which considered multiple modalities considered the intensity features corresponding to the modalities separately. No effort is made to combine the features from various modalities. Combination of features may suggest better results.
- None of the segmentation algorithms reviewed addressed the performance of normal region. Normal region identification is equally important to draw a demarcation between normal region and tumorous region.
- Most of the studies used segmentation algorithms to segment the tumour as a whole. Further classification of the tumour such as edema, necrotic core, enhancing tumour and non-enhancing tumour is not considered.
- The studies which classified the tumour into multiple regions used the same set of features to identify various classes. Developing separate features for various classes may improve the segmentation results.

2.2 Conclusion

Along with the unpredictable size, shape and location within the brain, whimsical boundaries among different sub-regions of a tumour in MRI make edge/contour based techniques to fail in segmenting the tumour sub-regions. Atlas or model based techniques also gave poor results. Literature review also shows that better results were achieved, when segmentation is treated as a classification problem rather than contour finding problem. Some works used clustering or unsupervised classifiers. Supervised classifier is superior to both these methods. Most of the works in literature does not consider tumour sub-regions while segmenting. They try to segment

the complete tumour only. The analysis of the sub-regions have wide applications such as prediction of survival rate, finding out nature of tumour, after treatment monitoring, etc.

Each modality of MRI is capable of identifying a certain type of tissue. Many of the existing techniques use single modality. Working in multiple modalities may yield better segmentation.

To get a better segmentation of various sub-regions of tumour, classification based segmentation using fusion of multiple MRI modalities is experimented in this work.

Chapter 3

Tools Used

3.1 Introduction

The framework of image segmentation through classification consists of three major steps. In the first stage various features are extracted from MRI and a feature set is formed. In the second stage unwanted features, that may reduce the efficiency of the segmentation system are identified and removed from the feature set. In the last

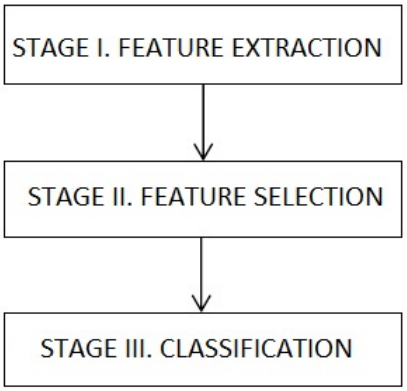

FIG. 3.1. Stages of Segmentation

stage classification is carried out using the selected features to get a labelled image. The pixels that have the same label, together constitute a segment. Fig. 3.1 shows the different stages involved in the segmentation process.

The various tools used in this study are explained in subsequent sections.

3.2 Feature Extraction

Feature is a synonym of attribute. Feature extraction can be considered as a pre-processing stage [74]. Extracting features from raw data has two advantages over using the raw data as itself.

- Reduces the number of data so that complexity of further processing becomes easy.
- Identifies features that can characterize the given data.

Reduction of the number of data makes processing easier at the cause of losing some information. The root of success of any classification technique is the availability of features with high discrimination capability among different classes under consideration. The result of classification stage highly depends on the class discriminating potential of the extracted features.

Prodigious number of techniques exist for extracting features from an image. Statistical feature extraction and transform based feature extraction are the two major categories of feature extraction techniques. In the case of medical image processing, accuracy of the output is more important than time complexity of the system. Along with pixel intensities, second order statistical features and transform based features are used. These specified features are extracted from all the four modalities of MRI ie FLAIR, T1 weighted, T1 weighted with contrast enhancement (T1C) and T2 weighted. As the segmentation problem is re-framed as a classification problem and the segmentation result is equated to the pixel by pixel classification result, all the features are extracted for each pixel.

3.2.1 One Dimensional Feature Extraction

For the current study, the only one dimensional feature extracted is the intensity feature. For a specific pixel, its intensities in FLAIR , T1 weighted , T1C and in T2 weighted modalities are taken to form a feature vector of size 4. Fig. 1.6 shows the 4 MRI modalities used in this study. The intensity of the pixel (x_i, y_i) from all the modalities form a feature vector of size 4 for that pixel

To examine the reliability of intensity features in tumour segmentation, the intensity ranges of edema, normal and tumour core (NC+ET+NET) are analysed with the help of available ground truth. The analysis was done in all four MRI modalities.

Fig. 3.2 shows the intensity distribution of normal, edema and tumour core in T1C modality. Fig. 3.3, Fig. 3.4 and Fig. 3.5 shows the intensity distributions of normal, edema and tumour core in T1 Weighted MRI, T2 Weighted MRI and FLAIR MRI respectively.

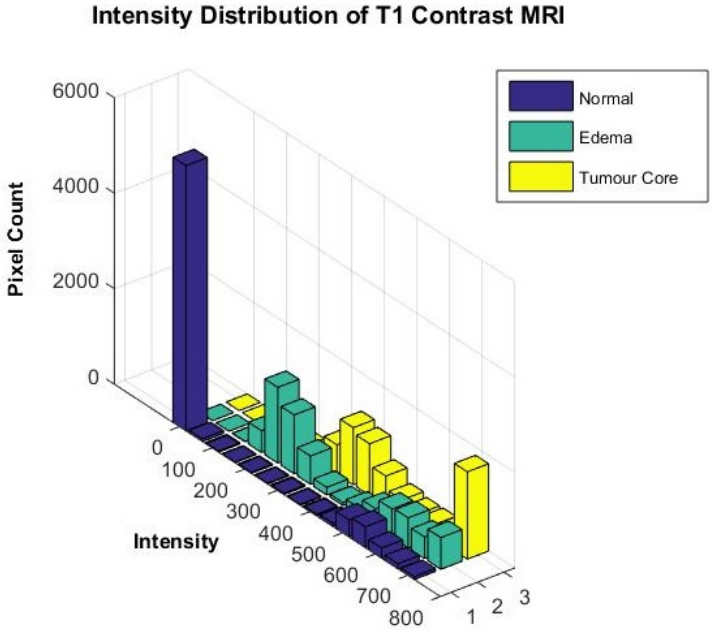

FIG. 3.2. Intensity distributions of Various Sub-regions in T1 Contrast MRI

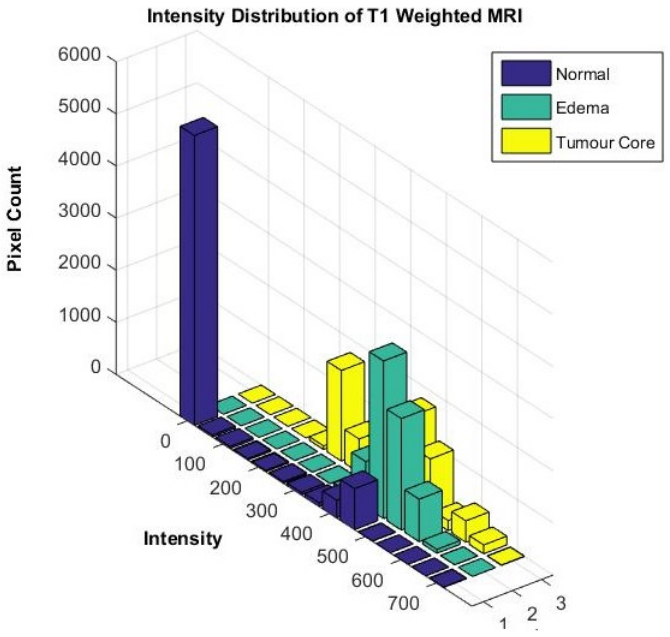

FIG. 3.3. Intensity distributions of Various Sub-regions in T1 weighted MRI

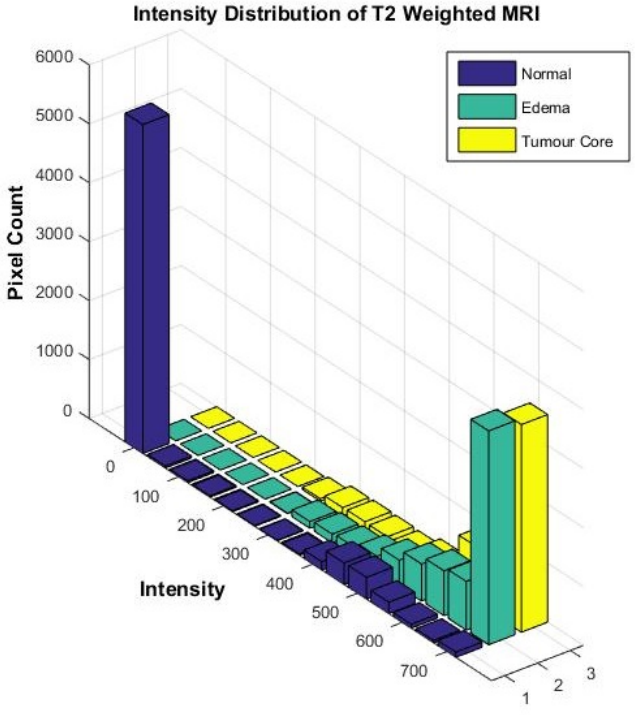

FIG. 3.4. Intensity distributions of Various Sub-regions in T2 weighted MRI

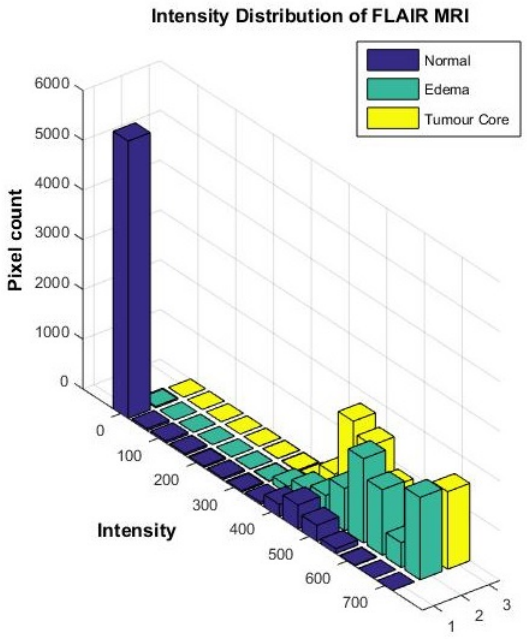

FIG. 3.5. Intensity distributions of Various Sub-regions in FLAIR MRI

The analysis reveals the fact that the intensities of edema, normal and tumour core are overlapped in such a way that segmentation of tumour and other substructures from any of the MRI modality is not achievable by the direct use of intensity feature alone. This gives rise to the requirement of additional more powerful features that can describe each sub-regions accurately. Hence second order statistical features and transform based features are considered.

3.2.2 Second Order Statistical Features

Second order statistical feature considered in this study are

1. Gray Level Co-occurrence Matrix (GLCM)
2. Gray Level Run Length Matrix (GLRLM)
3. Gray-Level Difference Matrix (GLDM)
4. Laws Texture Energy
5. Local Binary Pattern (LBP)

6. Local Ternary Pattern (LTP)

For each pixel in the image, 5 × 5 neighbourhoods are chosen as shown in Table 3.1 to form a sub-image from which all features except LBP and LTP are derived. For LBP and LTP, 8 neighbourhoods surrounding the pixel of interest are chosen.

TABLE 3.1: Sub-image Corresponding to pixel $Z_{i,j}$

Z(i-2,j-2)	..	..	..	Z(i-2,j+2)
..	Z(i-1,j-1)	..	Z(i-1,j+1)	..
..	..	**Z(i,j)**	..	..
..	Z(i+1,j-1)	..	Z(i+1,j+1)	..
Z(i+2,j-2)	..	..	..	Z(i+2,j+2)

3.2.2.1 Gray Level Co-occurrence Matrix

GLCM as proposed by Haralick *et al.* [75] is a matrix that defines the distribution of co-occurring grey-level values within an image or a sub-image. The matrix is formed by tabulating how many times different combinations of gray levels occurred together in the image or sub-image under consideration. A parameter that can be varied for the computation of GLCM is the offset, which represents the angle between the pixel of interest and its neighbour. Offset is a 2 valued vector. Depending on the offset, GLCM in different orientations can be computed. The various offsets and corresponding orientation angles are shown in Table 3.2 and in Fig. 3.6. The size of GLCM depends on the number of gray levels chosen. The gray values in the image are scaled so that it is converted to a value between 0 and G-1, where G is the number of gray levels. Another parameter is the distance d between two elements in the scaled image. In the current study distance is chosen as 1 and glcm matrices are formed for all four offsets. Number of gray level is set to 8.

Features mentioned in Albregtsen *et al.* [76] and Haralick *et al.* [75] are extracted. The texture features and their corresponding equations are shown in Table 3.3. The equations use the following notations:

TABLE 3.2: GLCM Orientation and Corresponding Offset

Angle	**Offset**
0	[0 1]
45	[-1 1]
90	[-1 0]
135	[-1 -1]

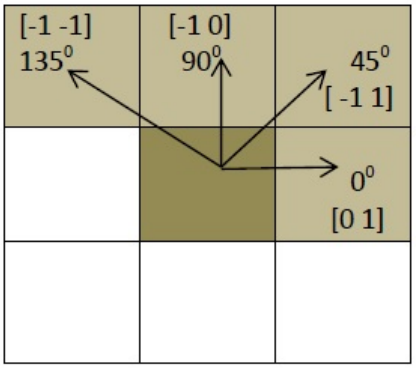

FIG. 3.6. GLCM Orientation and Corresponding Offset

G Number of gray levels.

P GLCM matrix.

μ The mean value of P

μ_x The row wise mean of GLCM

μ_y The column wise mean of GLCM

σ_x The row wise standard deviation of GLCM

σ_y The column wise standard deviation of GLCM

HX The entropy of P_x

HY The entropy of P_y

$P_{x+y}(k) = \sum_{i=0}^{G-1} \sum_{j=0}^{G-1} P(i,j)$

where i+j=k and k=0,1,...2G

$P_{x-y}(k) = \sum_{i=0}^{G-1} \sum_{j=0}^{G-1} P(i,j)$

where i-j=k and k=0,1,...G-1

$HXY1 = -\sum_{i=0}^{G-1} \sum_{j=0}^{G-1} P(i,j) log[P_x(i)P_y(j)]$

$HXY2 = -\sum_{i=0}^{G-1} \sum_{j=0}^{G-1} P_x(i)P_y(j) log[P_x(i)P_y(j)]$

TABLE 3.3: Features Extracted from GLCM

Feature	Equation
Contrast	$\sum_{i=0}^{G-1}\sum_{j=0}^{G-1}(i-j)^2 * P(i,j)$
Homogeneity	$\sum_{i=0}^{G-1}\sum_{j=0}^{G-1}P(i,j)^2$
Inverse Difference Moment (IDM)	$\sum_{i=0}^{G-1}\sum_{j=0}^{G-1}\frac{P(i,j)}{1+\lvert i-j\rvert^2}$
Entropy	$-\sum_{i=0}^{G-1}\sum_{j=0}^{G-1}P(i,j) * log[P(i,j)]$
Correlation	$\sum_{i=0}^{G-1}\sum_{j=0}^{G-1}\frac{(i-\mu_x)(j-\mu_y)P(i,j)}{\sigma_x\sigma_y}$
Sum of Squares	$\sum_{i=0}^{G-1}\sum_{j=0}^{G-1}(1-\mu)^2P(i,j)$
Sum Average	$\sum_{i=0}^{2G-2}iP_{x+y}(i)$
Sum Entropy	$-\sum_{i=0}^{2G-2}P_{x+y}(i)log[P_{x+y}(i)]$
Difference Entropy	$-\sum_{i=0}^{G-1}P_{x-y}(i)log[P_{x-y}(i)]$
Inertia	$\sum_{i=0}^{G-1}\sum_{j=0}^{G-1}(i-j)^2P(i,j)$
Cluster Shade	$\sum_{i=0}^{G-1}\sum_{j=0}^{G-1}(i+j-\mu_x-\mu_y)^3P(i,j)$
Cluster Prominence	$\sum_{i=0}^{G-1}\sum_{j=0}^{G-1}(i+j-\mu_x-\mu_y)^4P(i,j)$
Maximal Correlation Coefficient	$\sum[\frac{P(i,k)P(j,k)}{p_x(i)P_y(k)}]^{\frac{1}{2}}$
Information Measure of Correlation I	$\frac{HXY-HXY1}{max(HX,HY)}$
Information Measure of Correlation II	$1-exp[-2.0(HXY2-HXY)]^{\frac{1}{2}}$

3.2.2.2 Gray Level Run Length Matrix

GLRLM introduced by Galloway [77] is a texture analysis method based on run-lengths of image gray levels. In a coarse texture, relatively long gray-level runs would occur more often whereas a fine texture contains primarily short runs [78].Gray Level Run Length Matrix represented by GR is a matrix with dimension m x n, where m is the number of different gray-levels in the input matrix and n represents the run length. Features that are extracted from GLRLM for the current study are shown in Table 3.4. For all the equations in Table 3.4, n_r represents the number of runs and n_p is the number of pixels. A total of 44 features in all four directions ($0^0, 45^0, 90^0$ and 135^0) are extracted for the study. All the features are extracted based on an instinct that these will capture informations about run length distribution of gray-levels [78].

3.2.2.3 Texture Feature Extraction using Gray-Level Difference Matrix

For a given distance $d = (d_x, d_y)$ and matrix M, Gray Level Difference Matrix M_d is formed using the Equation 3.1 [79]

$$M_d(x, y) = |M(x, y) - M(x + d_x, y + d_y)| \tag{3.1}$$

The probability density P_d of $M_d(x, y)$ is an n dimensional vector where n is the number of gray-levels. The i^{th} component of P_d is the probability that $M_d(x, y)$ has the value i.

GLDM matrix formation for a pixel of interest is done on a sub-image formed by considering it's 5×5 neighbourhood.

Features that are extracted from the probability density of GLDM are the following.

$$Homogeneity = \sum_{i=1}^{n} \frac{P_d(i)}{(i^2 + 1)} \tag{3.2}$$

$$Contrast = \sum_{i=1}^{n} P_d(i).(i^2) \tag{3.3}$$

TABLE 3.4: Features Extracted from GLRLM

Feature	Equation
Short Run Emphasis	$SRE = \frac{1}{n_r}\sum_{i=1}^{m}\sum_{j=1}^{n}\frac{GR(i,j)}{j^2}$
Long Run Emphasis	$LRE = \frac{1}{n_r}\sum_{i=1}^{m}\sum_{j=1}^{n}GR(i,j).j^2$
Gray Level Non-uniformity	$GLN = \frac{1}{n_r}\sum_{i=1}^{m}[\sum_{j=1}^{n}GR(i,j)]^2$
Run Length Non-uniformity	$RLN = \frac{1}{n_r}\sum_{j=1}^{n}[\sum_{i=1}^{m}GR(i,j)]^2$
Run Percentage	$RP = \frac{n_r}{n_p}$
Low Gray-Level Run Emphasis	$LGRE = \frac{1}{n_r}\sum_{i=1}^{m}\sum_{j=1}^{n}\frac{GR(i,j)}{i^2}$
High Gray-Level Run Emphasis	$HGRE = \frac{1}{n_r}\sum_{i=1}^{m}\sum_{j=1}^{n}GR(i,j).i^2$
Short Run Low Gray-Level Emphasis	$SRLGE = \frac{1}{n_r}\sum_{i=1}^{m}\sum_{j=1}^{n}\frac{GR(i,j)}{i^2.j^2}$
Short Run High Gray-Level Emphasis	$SRHGE = \frac{1}{n_r}\sum_{i=1}^{m}\sum_{j=1}^{n}\frac{GR(i,j).i^2}{j^2}$
Long Run Low Gray-Level Emphasis	$LRLGE = \frac{1}{n_r}\sum_{i=1}^{m}\sum_{j=1}^{n}\frac{GR(i,j).j^2}{i^2}$
Long Run High Gray-Level Emphasis	$LRHGE = \frac{1}{n_r}\sum_{i=1}^{m}\sum_{j=1}^{n}GR(i,j).i^2.j^2$

$$AngularSecondMoment = \sum_{i=1}^{n}[P_d(i)]^2 \tag{3.4}$$

$$Entropy = -\sum_{i=1}^{n}P_d(i).log[P_d(i)] \tag{3.5}$$

$$Mean = \frac{1}{m}\sum_{i=1}^{n}P_d(i).i \tag{3.6}$$

3.2.2.4 Texture Feature Extraction using Laws Texture Energy Method

Law's texture energy measures are derived from three simple vectors of length 3. The first vector L=(1,2,1) is for the one-dimensional operations of center-weighted local averaging. The second vector E=(-1,0,1) represents the symmetric first differencing for edge detection, and the third vector S=(-1,2,-1) represents the second differencing for spot detection. The three vectors,L,E and S are convolved with the transpose of itself and with the transpose of others to form nine different 3 × 3 matrices. Of these nine matrices, six matrices (LL, EE, SS, LE, ES, LS) are chosen as kernels. To get the texture features, the above 3 × 3 kernels are convolved with the chosen sub-image and energy of each resultant matrix is used to describe the texture [80]. Energy of any m × n matrix LP is computed using the Equation 3.7.

$$Energy(LP) = \sum_{i=1}^{m}\sum_{j=1}^{n} LP(i,j)^2 \tag{3.7}$$

3.2.2.5 Local Binary Pattern

LBP is a texture analysis method that makes use of the differences of intensities surrounding a point [81]. As the name indicates, the LBP contains only two symbols ie. 0 and 1. LBP is generated by comparing 8 neighbourhood pixels of the pixel of interest. Zero is assigned to the neighbourhood if its intensity value is less than the central pixel. Otherwise a value of 1 is assigned to it. Fig. 3.7 portrays the LBP for the central pixel Z_0. The difference between a neighbourhood pixel, Z_i and the central pixel Z_0 is computed and binary pattern of length eight is generated according to Equation 3.8.

$$LBP(Z_0) = \sum_{i=1}^{8} S(Z_i - Z_0).2^{(8-i)}, where S(x) = \begin{cases} 1, & \text{if } x \geq 0 \\ 0, & \text{if } x < 0 \end{cases} \tag{3.8}$$

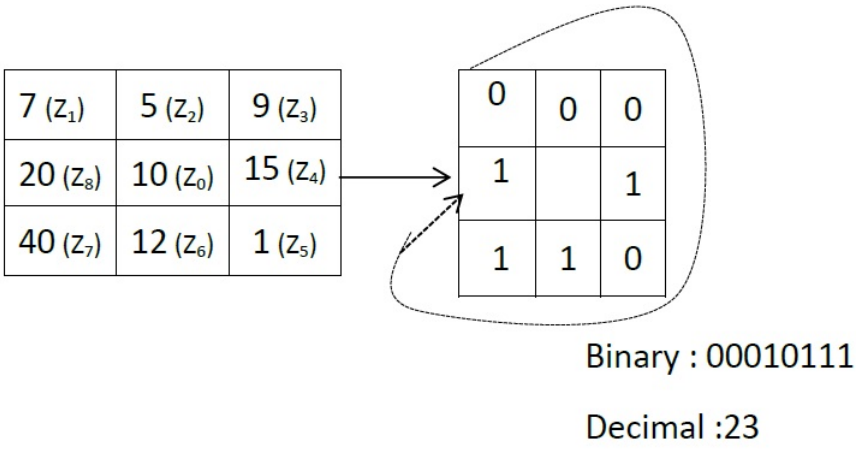

FIG. 3.7. LBP Code for the Central Pixel

3.2.2.6 Local Ternary Pattern

One of the popular variation of LBP is LTP. Like LBP, LTP also considers 8 neighbourhood intensity values of a pixel of interest. But it uses a threshold so that minor variations (values below a selected threshold) are suppressed and only prominent variations account for the pattern values. Fig. 3.8 shows the LTP code generation. The variations below the selected threshold are not taken into account and coded as zero. The positive difference between Z_i (i^{th}neighbouring pixel) and Z_0 (central pixel), which is beyond the threshold is coded as $+1$ and negative difference as -1. The coded pattern is decomposed into two binary patterns considering either $+1$ or -1 at a time and making others zero as shown in Fig. 3.8. The code generation is done according to Equation 3.9 and Equation 3.10 [82].

$$LTP(1, Z_0) = \sum_{i=1}^{8} S_1(Z_i - Z_0).2^{(8-i)}, where S_1(x) = \begin{cases} 1, & \text{if } x \geq t \\ 0, & \text{if } 0 < x < t \end{cases} \tag{3.9}$$

$$LTP(2, Z_0) = \sum_{i=1}^{8} S_2(Z_i - Z_0).2^{(8-i)}, where S_2(x) = \begin{cases} 1, & \text{if } -x \geq t \\ 0, & \text{if } -x < t \end{cases} \tag{3.10}$$

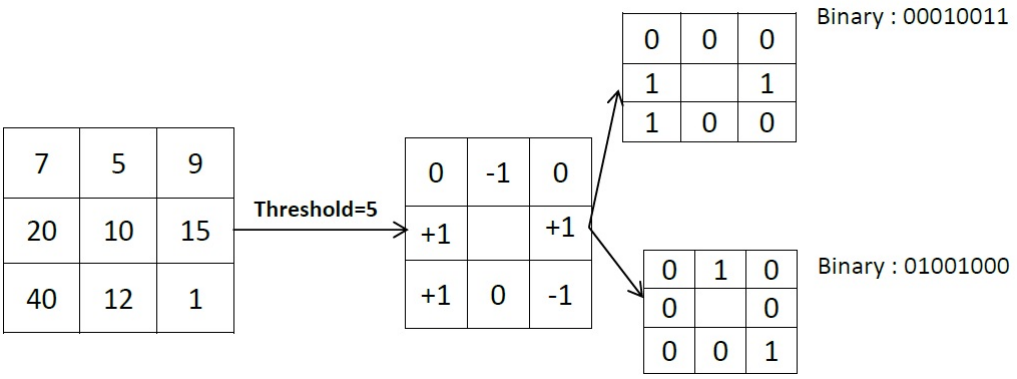

FIG. 3.8. LTP for the Central Pixel

3.2.3 Transform Based Features

Image transformations aim to exploit features from an image that are not easily detected in spatial domain. Two transform based features are used in the current study. Features extracted using FPS as well as SMRT are considered in this study.

3.2.3.1 Feature Extraction using FPS

Power spectrum gives the amount of signal at a particular frequency. To calculate the FPS of an image I, calculate sample power spectrum using the Equation 3.11. High values of the power spectrum near origin indicate coarseness while the spread out values represent that the texture is fine.

$$\psi(u,v) = F(u,v).F^*(u,v) = |F(u,v)^2| \tag{3.11}$$

where F stands for Fourier transform and * for complex conjugate. For the current study, the features extracted from FPS are radial sum and angular sum [83]. The equations for radial sum and angular sum are shown in Equation 3.12 and Equation 3.13 respectively.

$$\phi_{r_1,r_2} = \sum_{r_1^2 \leq u^2+v^2 < r_2^2} |F(u,v)|^2 \tag{3.12}$$

$$\phi_{\theta_1,\theta_2} = \sum_{\theta_1 \leq tan^{-1}(v/u) \leq \theta_2} |F(u,v)|^2 \tag{3.13}$$

3.2.3.2 Sequency Mapped Real Transform Based Features (SMRT)

SMRT as proposed in Jaya *et al.* [84] uses MRT coefficients $Y^{(p)}_{k1,k2}$ extracted for an image block $X_{n1,n2}, 0 < n1, n2 < N-1$, using Equation 3.14

$$Y^{(p)}_{k1,k2} = \sum_{\forall(n1,n2)|z=p} X_{n1,n2} - \sum_{\forall(n1,n2)|z=p+M} X_{n1,n2} \tag{3.14}$$

for $0 < k1, k2 < N-1$ and $0 < p < M-1$ where $M = N/2$ and $z = ((n_1k_1)+(n_2k_2))_N$

$k1, k2$ are the frequency indices and p is the phase index.

Selected MRT coefficients are reordered to form Sequency based MRT. Table 3.5 shows the placement of SMRT coefficients.

TABLE 3.5: Index Pattern of SMRT coefficients for N=8

0,0,0	0,1,0	0,1,1	0,1,2	0,1,3	0,2,0	0,2,2	0,4,0
1,0,0	1,1,0	3,1,0	5,1,0	7,1,0	1,2,0	3,2,0	1,4,0
1,0,1	1,1,1	3,1,1	5,1,1	7,1,1	1,2,1	3,2,1	1,4,1
1,0,2	1,1,2	3,1,2	5,1,2	7,1,2	1,2,2	3,2,2	1,4,2
1,0,3	1,1,3	3,1,3	5,1,3	7,1,3	1,2,3	3,2,3	1,4,3
2,0,0	2,1,0	2,1,1	2,1,2	2,1,3	2,2,0	6,2,0	2,4,0
2,0,2	6,1,0	6,1,1	6,1,2	6,1,3	2,2,2	6,2,2	2,4,2
4,0,0	4,1,0	4,1,1	4,1,2	4,1,3	4,2,0	4,2,2	4,4,0

For the current study, the image is divided into 8 × 8 sub-images. MRT coefficients are calculated using Equation 3.14. SMRT features are extracted by calculating the absolute sum of phase terms using Equation 3.15. [84] [85].

$$f_{k1,k2} = \frac{\sum_{i=1}^{N_b} \sum_p |Y^p_{k1,k2}|}{NXN} \tag{3.15}$$

where N_b is the number of blocks and $N \times N$ is the size of the image.

3.3 Feature Selection Tools

Feature selection is the process of selecting features that can strongly represent the image. Though both feature selection and dimensionality reduction tries to reduce the total number of features in the feature set, feature selection selects relevant features and excludes that are not relevant, whereas dimensionality reduction reduces feature set by creating new combinations of attributes. Feature selection carried out eliminates the features which are of no use in improving the performance of the segmentation system. From the total set of features explained in section 3.2, an optimized set of features are identified. Thus feature selection process minimizes the complexity of the system.

Feature selection can be carried out using various techniques. Major categories are explained in Table 3.6

TABLE 3.6: Categories of Feature Selection Techniques

No.	Method	Description	Example
1	Filter	Apply a statistical measure to assign a scoring to each feature. The features are ranked by the score and either selected to be kept or removed from the dataset.	Chi squared test
2	Wrapper	Consider the selection of a set of features as a search problem, where different combinations are prepared, evaluated and compared to other combinations. A predictive model is used to evaluate a combination of features and assign a score based on model accuracy.	Random Hill-Climbing algorithm, Genetic Algorithm
3	Embedded	Learn which features best contribute to the accuracy of the model while the model is being created	Regularization Methods

Unlike the filter methods, wrapper methods consider the relationships between variables and tend to be more efficient. The working of wrapper method is presented in Fig. 3.9. In each iteration a learning algorithm is executed to find out the classification efficiency by using the particular combination of features. In this study

we used two wrapper methods, Genetic Algorithm (GA) and Particle Swarm Optimization (PSO), for feature selection. Back Propagation Network (BPN) is used as learning algorithm in both methods. The methods are explained in Section 3.3.1 and in Section 3.3.2.

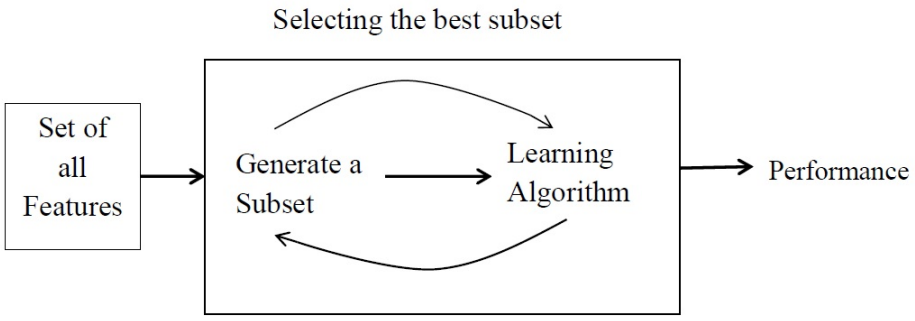

FIG. 3.9. Wrapper Technique for Feature Selection

3.3.1 Genetic Algorithm

GA is an adaptive heuristic search algorithms for optimization that mimic the process of natural evolution. GA implement the optimization strategies by simulating evolution of species through natural selection. Robustness is the main advantage of GA. They do not break down easily even in the presence of reasonable noise or when inputs are changed slightly. GA maintains a balance between efficiency and efficacy. GA is a randomized algorithm which contains several iterations of sequential execution of three operations, selection, cross over and mutation. Instead of a single solution, GA always works on a population of solutions. GA starts with a randomly selected population (set of solutions). The fitness of each solution in the population is then evaluated using a fitness function. Based on the fitness value a selection of good solutions are done. Selection is followed by a crossover operation with probability P_c on a pair of selected solutions at randomly chosen sites to produce better offsprings or solutions. The crossover is followed by mutation operation which is done with a probability P_m. Mutation helps in recovering lost genetic materials and randomly distributes genetic information. The three operations are done repeatedly until the stopping condition is reached [86]. In each iteration, BPN evaluates the accuracy of the system. Maximum number of iterations are chosen as the stopping

condition for GA in this work. Roulette-Wheel technique is used to carry out selection operation and single point cross over is done to create new offspring. The values of various parameters and methods used in GA implementation is summed up in Table 3.7.

TABLE 3.7: Values of the Parameters and Methods Used by GA for the Current Study.

Cross Over Probability (P_c)	Mutation Probability (P_m)	Selection Pressure (β)	Mutation Rate	Population Size	Maximum Iteration	Cross Over Method	Selection Technique
0.7	0.3	8	0.1	10	10	Single Point Crossover	Roulette Wheel

3.3.2 Particle Swarm Optimisation

PSO is an optimisation method which tries to improve a candidate solution with regard to a given measure of quality iteratively. The population of candidate solutions, which are termed as particles, are moved around in search space according to simple mathematical formulae over the particle's position and velocity. Each particle's movement is influenced by two factors. They are

1. Particle's local best known position
2. The best known position in the entire search space

The best known position is updated as better positions are found. This moves the swarm towards the best solution [86].

In this work, we used the basic version of PSO algorithm. It uses global topology as the swarm communication structure. Global topology allows all particles to communicate with all the other particles. Thus the whole swarm share the same best position from a single particle.

Since PSO is a population based stochastic optimization technique, it shares many similarities with evolutionary computation techniques. PSO is initialized with a population of random solutions and searches for optima by updating generations. The potential solutions or particles fly through the problem space by following the current optimum particles. In each step, each particle is accelerated towards its pbest (particle's coordinates in the problem space which are associated with the best solution so far) and lbest (the best value, obtained so far by any particle in the neighbours) locations. The parameters used by the PSO algorithm are enlisted in Table 3.8

TABLE 3.8: Parameter Values Used by PSO for the Current Study.

Maximum Velocity	Minimum Velocity	Inertia weight	Personal Learning Coefficient	Global Learning Coefficient	Population Size	Maximum Iteration
0.1	-1	0.66	1.36	1.36	20	20

3.4 Classification Tools

A classifier is a tool used to categorize the given data into a fixed number of classes. Classifiers can be categorised based on the number of classes into which the entire data are to be distributed and based on the learning technique. Based on the number of classes, a classifier can be a binary classifier (number of classes equals 2) or a multi-class classifier (number of classes greater than 2). Based on the learning method, a classifier is either a supervised classifier or unsupervised classifier. For the current work we need a multi-class classifier.

3.4.1 Unsupervised Classifier

Training phase will be absent in unsupervised classification process due to the lack of availability of training data. The entire data gets clustered according to their feature values. The underlying principle of clustering tries to reduce the inter cluster similarity and increase the intra cluster similarity. The cluster of the newly arrived data is decided in such a way that it obeys the above mentioned principle. Fig. 3.10 shows the schematic diagram of an unsupervised learning.

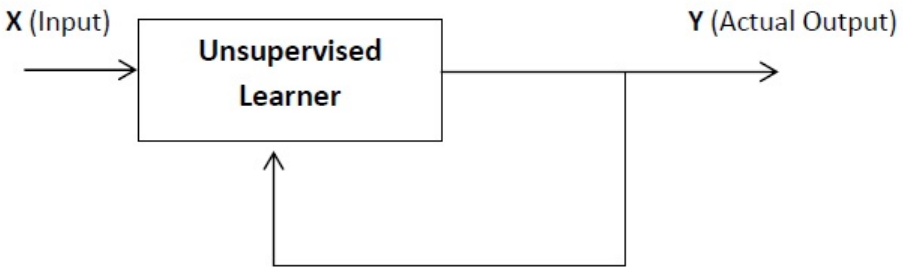

FIG. 3.10. Unsupervised Learning Technique

3.4.2 Supervised Classifier

Supervised classification makes use of supervised learning technique and it is applicable only when training data (data with input / output pair) are available. In supervised learning, we have input variables (X) and output variables (Y) and we use an algorithm to learn the mapping function from the input to the output $Y = f(X)$. Fig. 3.11 shows the supervised learning method. The goal is to approximate the mapping function so well that when a new input data (x_{new})arrives, mapping function should be able to predict the output variable (Y) for that data.

Supervised classification is carried out in two phases. The parameters are fixed or models are created with the help of input/output pair during training phase. When a new data arrives, it is classified with the help of the learned model or parameters in the testing phase [87].

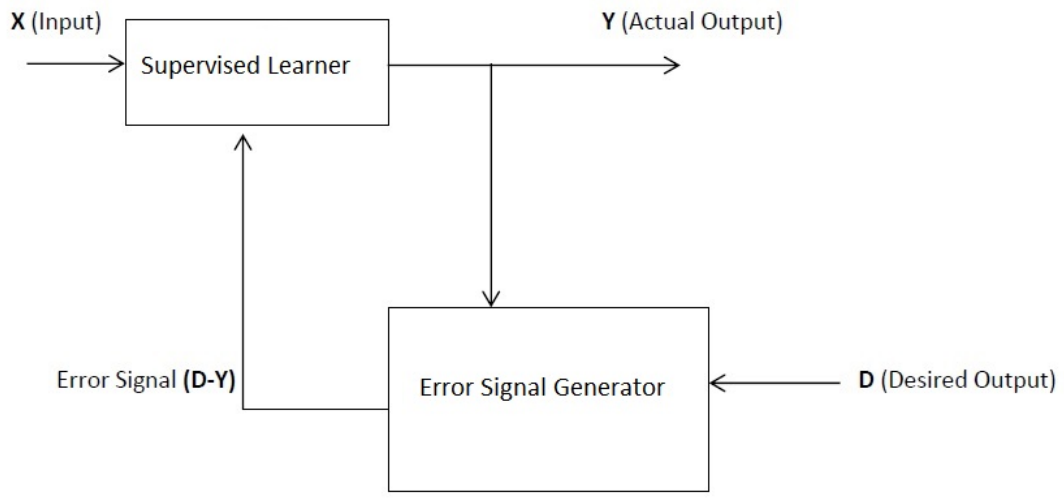

FIG. 3.11. Supervised Learning Technique

Since the training data are available and supervised classifier performs much better than unsupervised classifier, only supervised classifiers are engaged in this work to segment the tumour affected brain MRI. The supervised methods for classification incorporated in this work are listed below.

1. K-Nearest Neighbour (KNN)
2. Support Vector Machine (SVM)
3. Artificial Neural Network (ANN)
4. Bagged Ensemble of Trees

3.4.2.1 K-Nearest Neighbour Classifier

K number of neighbours are chosen for a given input based on selected distance measure. The class of a given object is decided based on the class of its K- nearest neighbours. During the training phase, a KNN-Model is created using the input/output pairs of data [88]. The parameters and their values for creating KNN model for the current study are listed below.

1. Number of Neighbours = 10

2. Distance Metric = Euclidean

3. Distance Weight = Squared Inverse

4. Priority = Uniform

In the second phase of classification the model created in the previous stage is used to classify the newly arrived data with unknown class.

3.4.2.2 Support Vector Machine

In its original form, SVM is a binary supervised classifier. The classification is done according to a chosen hyperplane. The choice of hyperplane is done in such a way that the distance to the nearest point on each side of the hyperplane is maximized [89].

There exist a number of ways to extend SVM as a multi-class classifier. The methods available and the underlying technique are shown in Table 3.9.

Like any other supervised classifiers, SVM also go through learning phase and testing phase. During training, an SVM model is created. The parameters and corresponding values used in SVM model creation are listed below. The SVM model is used in the next phase for classifying a given data with unknown class.

1. Kernel Function = Gaussian

2. Kernel Scale = 0.5

3. Box Constraint Level = 1

4. Multi Class Method = One Vs. One

TABLE 3.9: Techniques for extending binary SVM to Multi-class SVM

Method	Description	Number of Learners (for N class)
One vs.One (OVO)	Binary classifiers are learned considering only 2 classes at a time while others are ignored.	$\frac{N\times(N-1)}{2}$
One vs.All (OVA)	Binary classifiers are learned by grouping single class in the first group and rest in next group.	N
BinaryComplete (BC)	All binary combinations of classes are considered.	$2^{(N-1)}-1$
TernaryComplete (TC)	All ternary combinations(-1,0,+1) of classes are considered.	$\frac{3^{(N-1)}-2^{(N+1)}+1}{2}$
Ordinal	K^{th} classifier is learned by setting first K classes as positive and rest as negative.	$N-1$
Sparse Random	Random.	Approximately $15log_2N$

3.4.2.3 Artificial Neural Network

ANNs are computing systems inspired by the biological neural networks. An ANN is based on a collection of connected nodes called artificial neurons. Each connection (analogous to a synapse in biological neural network) between artificial neurons can transmit a signal. The artificial neuron that receives the signal, processes it and triggers the subsequent neurons if the signal strength exceeds a threshold. The interconnections among neurons have a weight that adjusts as learning proceeds. Typically, artificial neurons are organized in layers. Different layers may perform different kinds of transformations on their inputs. Signals travel from the first (input), to the last (output) layer, possibly after traversing the layers multiple times [87].

In this work we used the BPN, which is a three layered neural network consisting of input layer, hidden layer and output layer as shown in Fig. 3.12. During the learning phase, errors are calculated at the output layer (difference between the actual output and expected output) after processing a batch of data. The calculated errors are propagated backward to the hidden layer and then to the input layer. During the backward propagation of errors, the interconnection weights are updated using gradient descent technique. In this work a single hidden layer with 10 neurons is used.

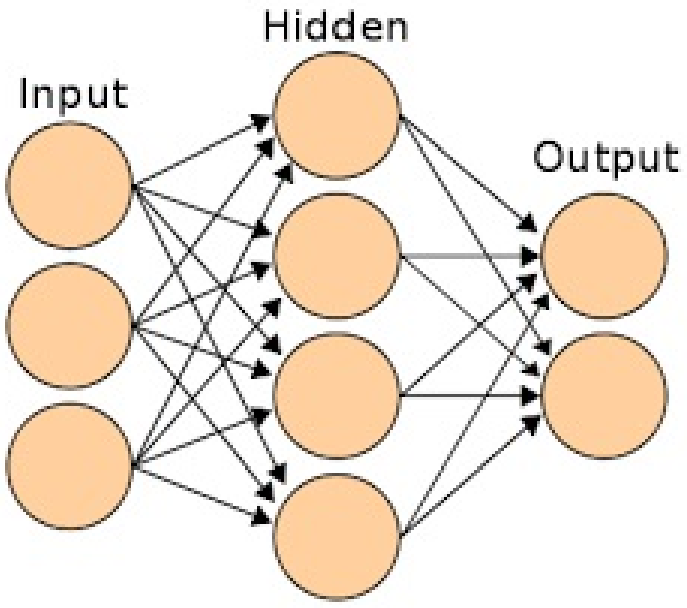

FIG. 3.12. Layers of Artificial Neural Network

After the training session, the weights are fixed and a learned or trained neural network is obtained. During the second phase, data with unknown class is given as input to the trained network and the output of the network gives the class of the given data.

3.4.2.4 Bagged Ensemble of Trees

A classification tree predicts the class of the given data. As shown in Fig. 3.13, a classification tree is a binary tree (each node has a maximum of two children) which contains a root node, intermediate nodes and leaf nodes. Each leaf node represents

a single class in the given classification problem. Root node and each intermediate node represents a decision criteria. The classification process starts from the root of the tree. In all nodes except the leaf nodes, a check is carried out and based on the results, the tree is traversed from root to leaf thus reaching a conclusion regarding the class of the given data.

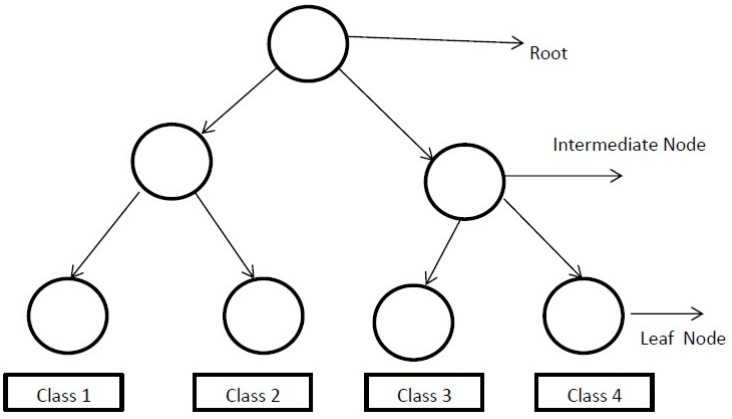

FIG. 3.13. A Classification Tree

Instead of a single tree, an ensemble of classification trees would yield better results. There exists several ways for creating an ensemble of trees. In this study bootstrap aggregation or bagging is used as ensemble technique. The parameters and values assigned are listed below.

1. Ensemble Method = Bagging

2. Number of Learners = 200

3. Learning Rate = 0.1

4. Subspace Dimension = 1

3.5 Data

Brain Tumour Segmentation (BraTS) challenge, which is organized every year, focuses on the segmentation of intrinsically heterogeneous brain tumours. BraTS challenge utilizes multi-institutional pre-operative MRI scans. The data base of BraTs challenge contains both real and simulated data.

Real data from BraTS 2015 and BraTS 2016 databases are used for this work [90]. The database contains images of fully anonymous cases from ETH Zurich, University of Bern, University of Debrecen, and University of Utah. All four modalities (T1,T2,T1C and FLAIR) were available along with corresponding ground truth. All were skull stripped and linearly co-registered with T1 image. Around 350 cases were available of which 120 were chosen randomly. For each case 176 slices were available of which 5 slices were selected, based on their visual quality, to carry out the segmentation. The images were taken in axial plane. MRI images corresponding to 21 cases were also collected from Hindlab MRI Scan Centre, Government Medical College, Thrissur and Lakeshore Hospital, Cochin. All the considered images are gray scale images. 75 % of the data was used for training and 25 % for testing.

All the experiments were conducted on a 64 bit Intel Core i3 machine with 1.8GHz speed and 4GB internal RAM. Matlab (2015) software was used for programming.

3.6 Conclusion

Feature extraction tools, feature selection tools and classification tools used for the study along with their parameters are discussed. The data used for this study, the system and software through which programs were implemented are also explained. All the features explained in this chapter pertain to an image of particular modality. To improve the performance of the segmentation algorithm, features are derived considering multiple modalities together. Such a feature extraction method ie Multi-Spectral Pattern based Texture Features (MSPTF) is proposed in the next chapter.

Chapter 4

Multi-Spectral Pattern Based Texture Feature

4.1 Introduction

The classification based segmentation starts with feature extraction. All the feature extraction tools described in the previous chapter is capable of extracting features from a single image. But in the case of MRI images, multiple modalities are available and certain types of tissues are exposed in each modality. Features extracted from a single modality can delineate particular types of tissues only. For example in T1 weighted modality, both CSF and inflammation is shown as bright and fat as dark. But in FLAIR image, CSF is dark and inflammation and fat is bright or light. A new feature extraction technique, Multi Spectral Pattern based Texture feature (MSPTF), that can make use of informations from multiple modality is proposed in this chapter. The comparison of the proposed features and conventional features in segmenting tumour and related sub-regions is carried out with the help of KNN classifier, SVM classifier and Bagged Tree classifier.

4.2 Multi Spectral Pattern Based Texture Feature Extraction

MSPTF is a newly proposed technique which uses multiple MRI modalities simultaneously to extract features that best describe each regions in a tumour affected MRI. Each MRI modality highlights certain pathology of brain. Their combined use will yield features that have high discriminating power among different components of a tumour affected MRI. The proposed algorithm has three distinct phases which are listed below.

1. Distance Vector (DV) calculation
2. Encoding Distance Vector
3. Transformation of coded vectors into binary format and feature extraction

The phases of MSPTF are described in Section 4.2.1, Section 4.2.2 and Section 4.2.3.

4.2.1 Distance Vector Calculation

In this initial phase, patient's MRI images in n different modalities are supplied to the algorithm as input. This phase transforms the images in different modalities into distance vectors. For each pixel, a DV is calculated. The elements in the DV are either positive integers or negative integers or zero depending on the intensity of the pixel in various modalities.

DV is generated for each pixel in the image by comparing its intensities in different MRI modalities. The size of DV depends on the number of MRI modalities (n) considered. Compute differences of the corresponding pixel intensities considering two MRI modalities at a time. The distance vector DV is calculated, as shown in Fig. 4.1. The size of DV is a function of n and it is given by the equation $Size(DV) = \frac{n(n-1)}{2}$. DV is encoded in the second phase of the MSPTF extraction algorithm.

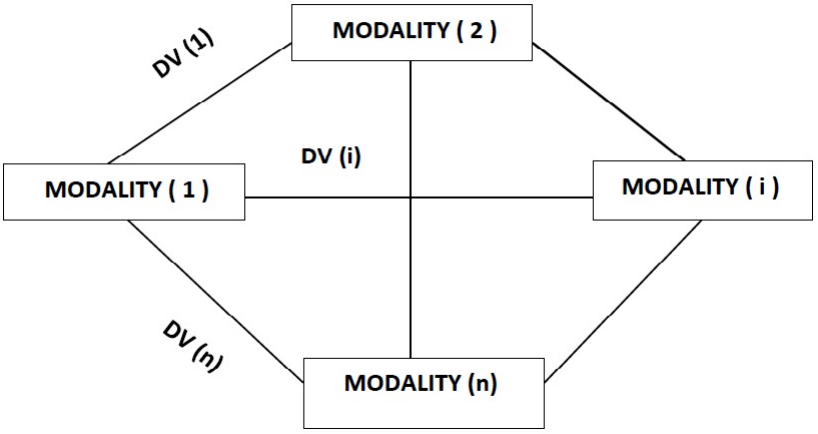

FIG. 4.1. Pairwise Distance Among all Modalities to Form DV of Size $n(n-1)/2$

4.2.2 Encoding Distance Vector

Input to this phase is a DV corresponding to a pixel and output is the Encoded Distance Vector (EDV). The size of EDV is same as the size of DV.

The values in DV are encoded into 7 different values (0,+1,-1,+2,-2,+3,-3). Three threshold values τ_1 (lower threshold), τ_2 (middle threshold) and τ_3 (upper threshold) are used for encoding purpose. Encoding is done according to the Equation 4.1.

$$EDV(i) = \begin{cases} 0, & \text{if } abs[DV(i)] < \tau_1 \\ +1, & \text{if } \tau_1 \leq DV(i) < \tau_2 \\ -1, & \text{if } \tau_1 \leq -(DV(i)) < \tau_2 \\ +2, & \text{if } \tau_2 \leq DV(i) < \tau_3 \\ -2, & \text{if } \tau_2 \leq -(DV(i)) < \tau_3 \\ +3, & \text{if } DV(i) \geq \tau_3 \\ -3, & \text{if } -(DV(i)) \geq \tau_3 \end{cases} \tag{4.1}$$

4.2.3 Feature Extraction from Encoded Distance Vector

The final stage of MSPTF is the extraction of features from EDV. A seven-valued EDV is given as input to this phase and six binary vectors (containing only 0's and 1's) are generated as output. All binary vectors have the same size as EDV.

For conversion, a single value out of the seven values in the EDV is considered at a time. All other values are made zero at this point. Thus six binary vectors are generated for EDV(i) corresponding to +1, -1, +2, -2, +3 and -3 respectively.

The six binary vectors are then converted to decimal values to serve as features for the pixel under consideration.

The output of MSPTF algorithm is stored in the matrix $\Re$. The entire algorithm is presented in Algorithm 1. A numerical illustration of Algorithm 1 can be seen in Appendix A.

Algorithm 1: Multi Spectral Pattern based Feature Extraction

Input: Images in n different MRI modalities, τ_1, τ_2, τ_3
Output: Multi spectral pattern based feature set $\Re$

1: $d1, d2 = size(image)$
2: Initialize $\Re$ to a 3D matrix of zeros of size d1 $\times$ d2 $\times$ [n $\times$ (n-1)/2]
3: Set the All modality 3D matrix M of size d1 $\times$ d2 $\times$ n with different modalities of images given as input
4: **for** i=1 to d1 **do**
5: **for** j=1 to d2 **do**
6: Initialize count to 0. Initialize DV and EDV as zero vectors of size n $\times$ (n-1) /2 .
7: Calculate DV of the pixel $P_{i,j}$ through step 9 to step 14
8: **for** l=1 to (n-1) **do**
9: **for** m=l+1 to n **do**
10: $DV(count) = M(i, j, l) - M(i, j, m)$
11: $count = count + 1$
12: **end for**
13: **end for**
14: Encode DV of the pixel $P_{i,j}$ using Equation 4.1 and store it in EDV.
15: Convert the 7 symbol EDV into 6 binary patterns b_1, b_2, b_3, b_4, b_5 and b_6 considering one symbol at a time and making others zero
16: Convert all binary pattern into corresponding decimal $dc_1, dc_2, dc_3, dc_4, dc_5$ and dc_6
17: $\Re_{i,j} = \{dc_1, dc_2, dc_3, dc_4, dc_5, dc_6\}$.
18: **end for**
19: **end for**

4.3 Performance Measures

To evaluate the proposed feature and compare it with other conventional features, classification is performed.

The result of a classifier is measured using four parameters, True Positives (TP), True Negatives (TN), False Positives (FP) and False negatives (FN). Table 4.1 can be used to elucidate the parameters.

TABLE 4.1: Parameters for Measuring Classification Result

Actual Condition	A	Not A
Classifier says "A"	TP	FP
Classifier says "Not A"	FN	TN

Precision, Sensitivity and Dice-Score are used for analysing the classification results. These metrics make use of more than one above mentioned parameters. Equation 4.2 through Equation 4.4 shows the definition of these metrics.

$$Precision = \frac{TP}{TP + FP} \tag{4.2}$$

$$Sensitivity = \frac{TP}{TP + FN} \tag{4.3}$$

$$Dice - Score = \frac{2}{\frac{1}{Precision} + \frac{1}{Sensitivity}} \tag{4.4}$$

Sensitivity is a function of TP and FN. A high sensitivity indicates that a class has high TP and low FN. But this metric does not deal with FP. Unlike classification in other images, both FN and FP are equally harmful in the case of medical images. Thus a classifier which yields a significant sensitivity value for a particular class may have a high FP , which is not desirable. On the other hand precision is a function of TP and FP. It does not consider FN. Thus a third metric ie Dice-Score, which is derived from sensitivity and precision is also used for the analysis of results.

4.4 Analysis of Results

SVM, KNN and Bagged Tree classifiers are used to evaluate the performance of the newly developed feature. Models for KNN classifier, SVM classifier and Bagged Tree classifier are created using training data and parameter values mentioned in Section 3.4.2.1, Section 3.4.2.2 and Section 3.4.2.4 respectively. All the conventional methods are executed in the four different modalities (FLAIR, T1, T1C, T2) independently. For the developed method, all modalities are used together. The threshold values used in MSPTF algorithm are computed by analysing the intensity values of tumour sub-regions in various modalities. To calculate the thresholds, the range of intensity differences are divided into three as shown in Equation 4.5.

$$A = \frac{\Delta - \delta}{3} \tag{4.5}$$

In Equation 4.5 Δ represents the maximum of absolute value of intensity difference and δ is the minimum of absolute value of intensity difference, of corresponding pixels among all considered modalities.

Thresholds are calculated using Equation 4.6.

$$\tau_k = \delta + A * (k - 1) \tag{4.6}$$

Where k varies from 1 to 3.

For this study, the threshold values used are $\tau_1 = 50$, $\tau_2 = 125$ and $\tau_3 = 200$.

From the BraTs database of 350 cases, 120 cases are randomly chosen. For each case, five slices were selected based on their visual quality. For all these images the ground truths were available. From these images, m $\times$ n matrices were considered which contains pixels corresponding to tumour and its sub-regions. A total of 592 features were derived from these matrices. These features are given as input to SVM, KNN and Bagged Tree classifiers independently. A five fold cross validation is carried out and confusion matrices are obtained. The performance measures mentioned in Section 4.3 are retrieved from the confusion matrices. The framework of the system is shown in Fig. 4.2.

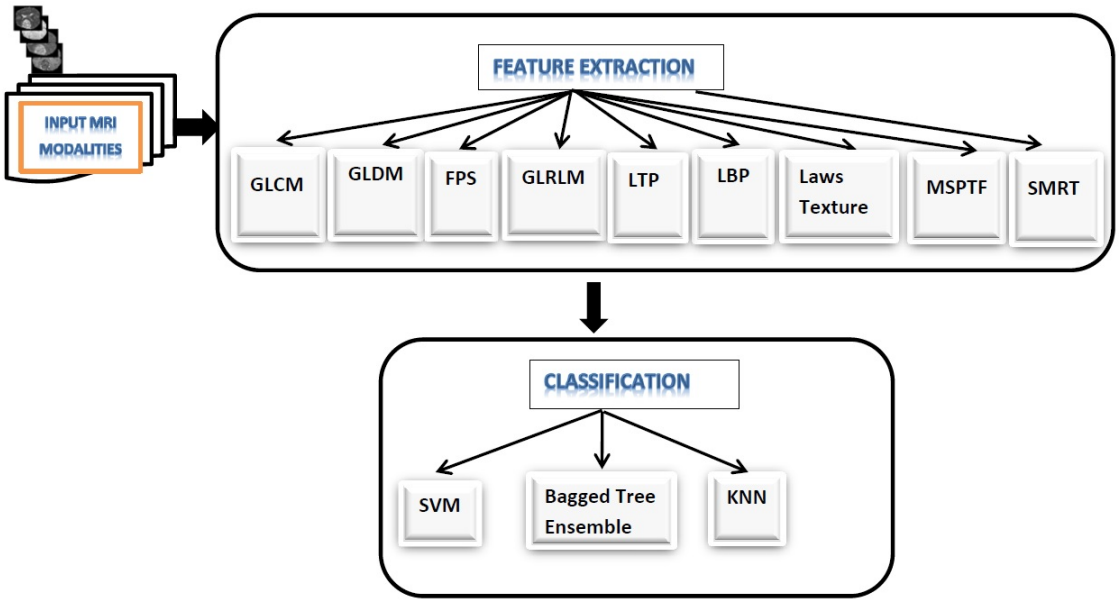

FIG. 4.2. System Framework

4.4.1 Analysis of Results of KNN Classifier

Table 4.2 shows the sensitivity measures of various classes when KNN classifier and different feature sets are used.

TABLE 4.2: Sensitivity of KNN classifier with Different Features

CLASS	FPS	GLCM	GLDM	GLRLM	LAWS	LBP	LTP	SMRT	MSPTF
N	0.68	0.61	0.61	0.38	0.57	0.58	0.62	0.69	**0.78**
NC	0.58	0.41	0.55	0.40	0.44	0.52	0.55	0.36	**0.67**
E	0.69	0.55	0.65	0.44	0.67	0.52	0.52	0.51	**0.73**
NET	0.39	0.37	0.29	0.36	0.37	0.39	0.46	0.32	**0.48**
ET	0.62	0.39	0.62	0.52	0.58	0.52	0.54	0.28	**0.67**

Results show that MSPTF features yielded a sensitivity of 0.78 for normal region, which is higher than the sensitivity given by other features. From the equation of sensitivity, we can infer that 22 % of the total normal tissues were wrongly classified into other classes. In the case of edema, 73 % got correctly classified using the developed feature extraction method. Although only less than half percent of the

non-enhancing tumour cells are placed in correct class by MSPTF, it still worked better than other existing features. Around 67 % of enhancing tumour got correctly placed by MSPTF feature set.

All sub-regions got a better sensitivity when MSPTF features were employed. But the sensitivity of normal tissue is a matter of concern since 22 % of the total normal tissues were misclassified as affected. The graphical view of the sensitivity measure is shown in Fig. 4.3

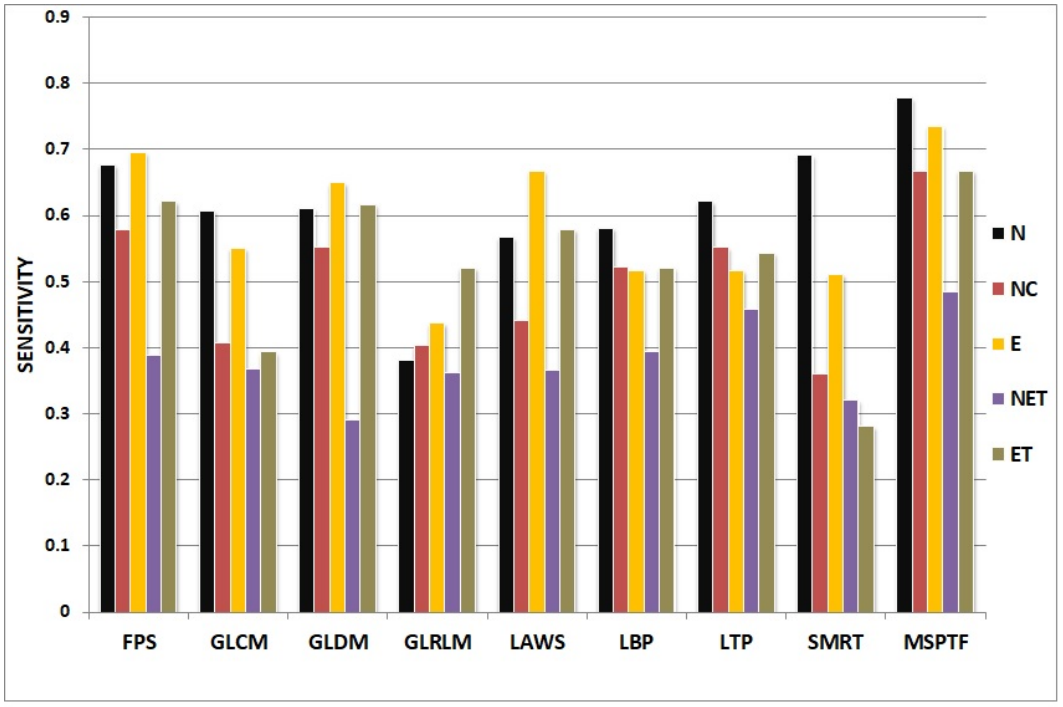

FIG. 4.3. Sensitivity of KNN classifier with Different Features

Precision measure of a class depends on TP and FP. A greater value of precision for a class implies more number of objects of that class got exactly classified and/or the number of other class objects that were inappropriately classified into this particular class is less. Precision of the five classes, when feature sets extracted using the considered conventional methods and the developed method is presented in Table 4.3.

From the results, it is clear that for all classes, the MSPTF gave a precision value much better than other existing methods. Except NET, the precision for all other classes were above 0.67 when the developed features were used. In the case of normal tissues, the precision using KNN classifier is 0.76. This implies that a

TABLE 4.3: Precision of KNN classifier With Different Features

CLASS	FPS	GLCM	GLDM	GLRLM	LAWS	LBP	LTP	SMRT	MSPTF
N	0.70	0.64	0.65	0.49	0.52	0.59	0.62	0.59	**0.76**
NC	0.63	0.46	0.54	0.51	0.56	0.57	0.58	0.49	**0.69**
E	0.57	0.45	0.61	0.47	0.57	0.52	0.54	0.39	**0.67**
NET	0.45	0.39	0.37	0.38	0.40	0.40	0.44	0.35	**0.53**
ET	0.65	0.45	0.55	0.34	0.61	0.47	0.51	0.36	**0.70**

number of objects that actually belong to the affected classes were misclassified into normal class by the KNN classifier. The graphical representation of the precision measures are shown in Fig. 4.4 .

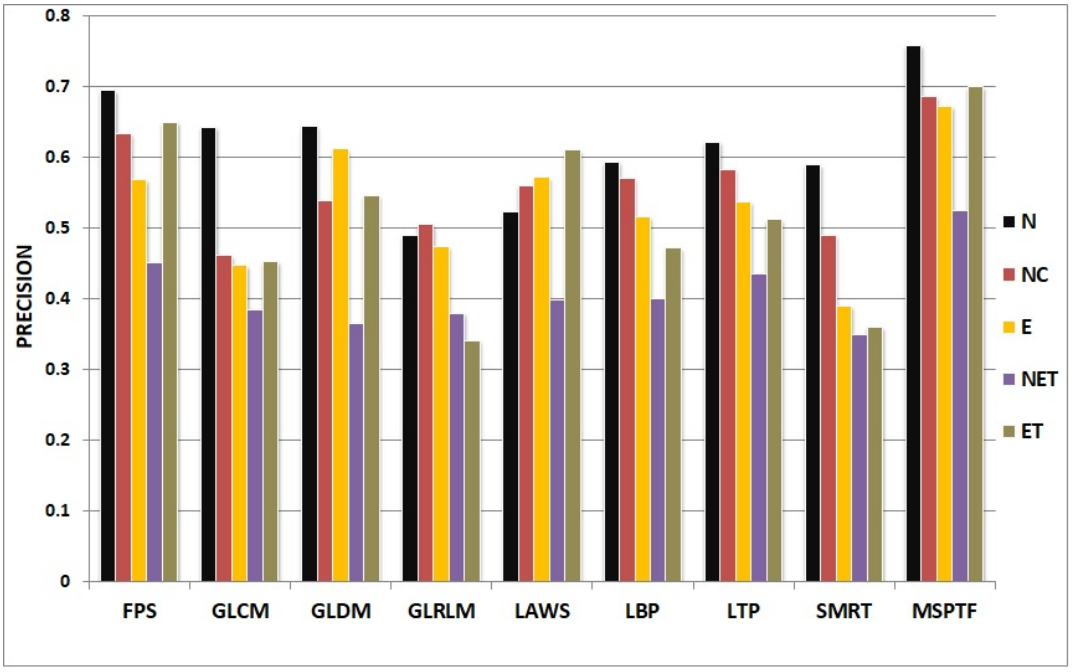

FIG. 4.4. Precision of KNN classifier with Different Features

Dice-Score for different classes, when a KNN classifier is employed, are shown in Table 4.4. The results are presented in Fig. 4.5 in chart form.

Results reveal that the Dice-Scores using MSPTF feature set are much greater than Dice-Scores using other features when KNN classifier is applied. For normal region, KNN classifier gave a Dice-Score of 0.77 using MSPTF features. For all the

TABLE 4.4: Dice-Score of KNN classifier in Segmenting Tumourous MRI

CLASS	FPS	GLCM	GLDM	GLRLM	LAWS	LBP	LTP	SMRT	MSPTF
N	0.69	0.63	0.63	0.43	0.54	0.59	0.62	0.63	**0.77**
NC	0.60	0.43	0.55	0.45	0.49	0.54	0.57	0.41	**0.68**
E	0.63	0.49	0.63	0.45	0.62	0.52	0.53	0.44	**0.70**
NET	0.42	0.38	0.32	0.37	0.38	0.40	0.45	0.33	**0.50**
ET	0.64	0.42	0.58	0.41	0.59	0.50	0.53	0.31	**0.68**

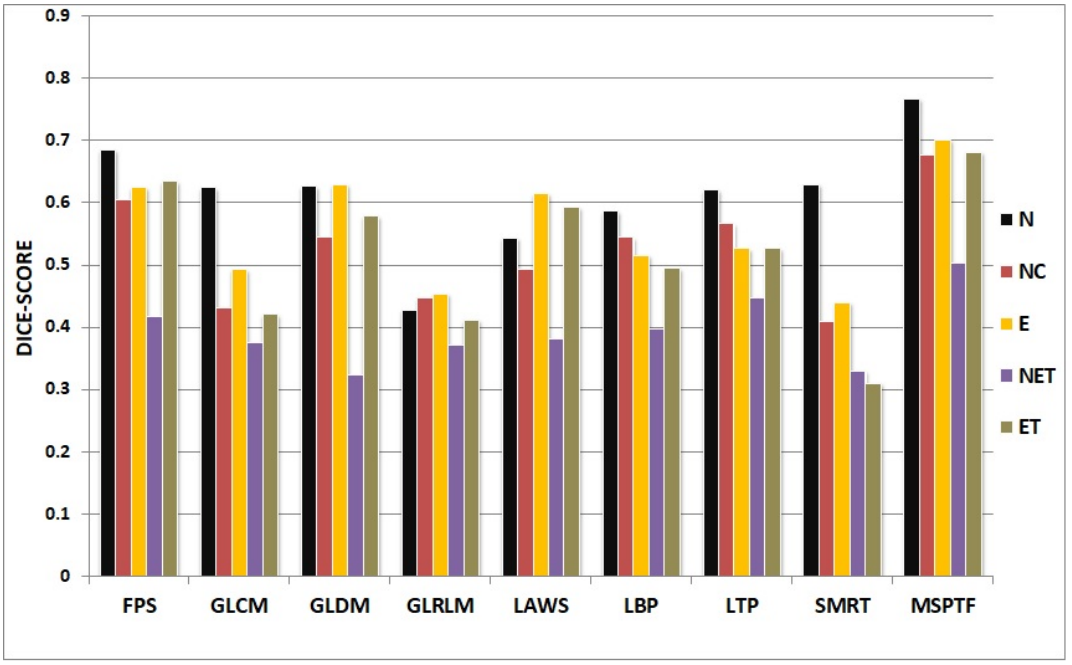

FIG. 4.5. Dice-Score of KNN classifier with Different Features

classes except NET, MSPTF yielded a Dice-Score greater than or equal to 0.68. For NET the Dice-Score given by KNN classifier is 0.50.

4.4.2 Result Analysis of SVM classifier

Feature sets obtained using 9 different feature extraction methods including the developed one are given to the SVM classifier and the results are analysed based on 3 measures.

The analysis of sensitivity of SVM classifier using different feature sets is shown in Table 4.5 and in Fig. 4.6.

TABLE 4.5: Sensitivity of SVM classifier with Different Features

CLASS	FPS	GLCM	GLDM	GLRLM	LAWS	LBP	LTP	SMRT	MSPTF
N	0.76	0.95	0.74	0.82	0.72	0.55	0.57	0.71	**0.80**
NC	0.21	0.00	0.45	0.00	0.08	0.45	0.47	0.44	**0.61**
E	**0.80**	0.22	0.59	0.40	0.47	0.58	0.60	0.56	**0.80**
NET	0.12	0.01	0.27	0.00	0.11	0.37	0.37	0.23	**0.59**
ET	0.43	0.00	0.59	0.00	**0.69**	0.44	0.46	0.28	0.67

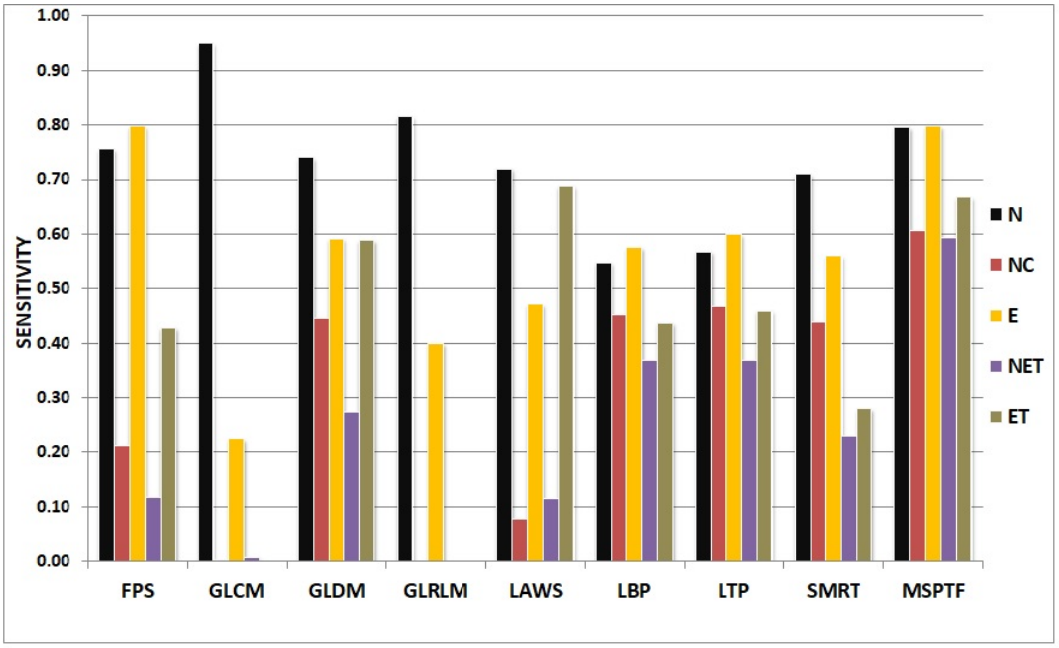

FIG. 4.6. Sensitivity of SVM classifier with Different Features

From the analysis it is clear that FPS, GLCM, GLRLM and LAWS feature sets did not perform consistently. Sensitivity given by GLCM, FPS, GLRLM and LAWS texture feature sets for NC and NET classes fall below 25 % . GLCM and GLRLM sensitivity for all classes except normal and edema classes are almost zero. This implies that most of the pixels got classified into normal class and some of the remaining into edema class when GLCM or GLRLM feature sets were used. The proposed feature set gave a sensitivity of 0.80 for both normal and edema regions. For necrotic core and non-enhancing tumour classes, MSPTF feature set yielded a

sensitivity of 0.61 and 0.59 respectively. But compared to other feature sets, MSPTF gave better results for all the classes except ET. Laws Texture energy delivered a sensitivity of 0.69 for ET which is higher than the sensitivity given by MSPTF. But the sensitivity of all other classes using Laws Texture energy are much less.

Table 4.6 and Fig. 4.7 show the precision measures of the 5 different classes when SVM classifier is applied to various feature sets.

TABLE 4.6: Precision of SVM classifier with Different Features

CLASS	FPS	GLCM	GLDM	GLRLM	LAWS	LBP	LTP	SMRT	MSPTF
N	0.59	0.32	0.53	0.30	0.42	0.52	0.53	0.64	**0.67**
NC	0.85	**1.00**	0.61	0	0.76	0.52	0.53	0.40	0.87
E	0.39	0.33	0.65	0.27	**0.71**	0.50	0.53	0.42	0.68
NET	0.65	0.76	0.46	0.00	0.65	0.43	0.44	0.32	**0.68**
ET	0.62	0.00	0.52	0.00	0.37	0.45	0.46	0.41	**0.74**

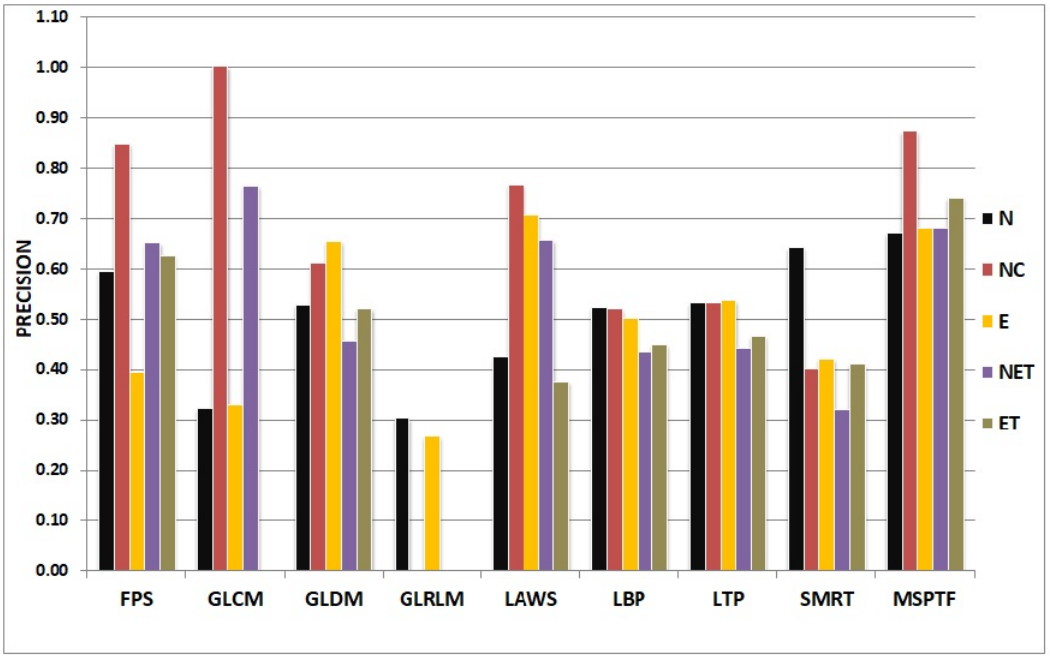

FIG. 4.7. Precision of SVM classifier with Different Features

Results show that for normal class, the proposed feature set gave a precision of 0.67, which is much higher than the precision produced by other feature sets. In the case of NC and NET, even though GLCM features returned a precision of 1 and 0.76

respectively, for other classes the precisions were very less compared to other feature sets. For edema class, LAWS features produced the best precision. But for other classes, results were much less compared to the best precision values in each class. Although the developed feature set could produce the best precision for normal and enhancing tumour class only , it performed consistently for all other classes.

KNN classifier gave a better precision for normal class than SVM classifier when MSPTF was used. This clearly indicates that normal class was not easily separable using the decision plane selected for SVM. Also KNN generated a highly convoluted decision boundary driven by the training data for normal class.

Table 4.7 and Fig. 4.8 shows the SVM classifier's Dice-Scores when the existing and developed feature sets are used.

TABLE 4.7: Dice-Score of SVM classifier with Different Features

CLASS	FPS	GLCM	GLDM	GLRLM	LAWS	LBP	LTP	SMRT	MSPTF
N	0.66	0.48	0.62	0.44	0.53	0.53	0.55	0.67	**0.73**
NC	0.34	0.00	0.52	0.00	0.14	0.48	0.50	0.41	**0.71**
E	0.53	0.27	0.62	0.32	0.57	0.54	0.57	0.48	**0.73**
NET	0.20	0.01	0.34	0.00	0.19	0.40	0.40	0.27	**0.64**
ET	0.51	0.00	0.55	0.00	0.48	0.44	0.46	0.34	**0.70**

For all classes except non-enhancing tumour class, MSPTF features returned a Dice-Score that lies between 0.70 and 0.73. For non-enhancing tumour class the Dice-Score of MSPTF feature set is 0.64. But the second highest value of DS given by SVM classifier is by using 0.40, which was given by both LBP feature and LTP features

For all classes MSPTF gave maximum DS. DS value using other features were much less than that using MSPTF for all ROI.

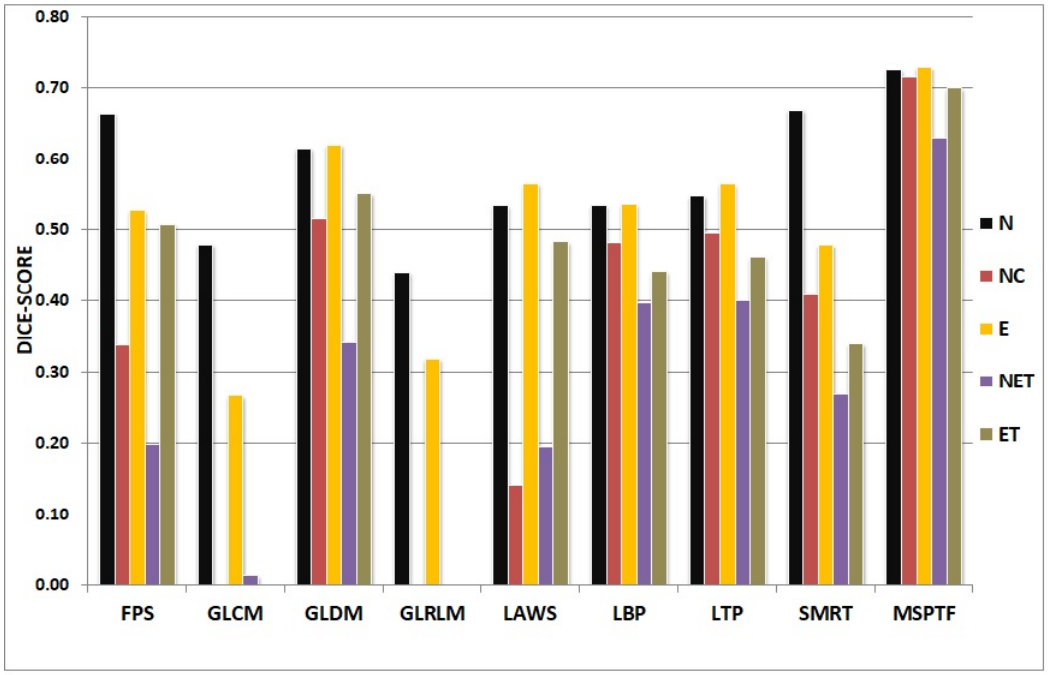

FIG. 4.8. Dice-Score of SVM classifier with Different Features

4.4.3 Result Analysis of Bagged Tree classifier

Comparison of the sensitivity values is shown in Table 4.8 and Fig. 4.9. For all the classes except NC and ET, MSPTF features gave the maximum sensitivity using Bagged Tree classifier.

TABLE 4.8: Sensitivity of Bagged Tree classifier with Different Features

CLASS	FPS	GLCM	GLDM	GLRLM	LAWS	LBP	LTP	SMRT	MSPTF
N	0.83	0.76	0.68	0.55	0.70	0.70	0.72	0.83	**0.85**
NC	**0.63**	0.42	0.48	0.42	0.40	0.49	0.33	0.54	0.60
E	**0.75**	0.59	0.65	0.54	0.67	0.67	0.69	0.66	**0.75**
NET	0.48	0.38	0.35	0.30	0.28	0.42	0.32	0.45	**0.58**
ET	0.73	0.43	0.66	0.37	0.67	**0.79**	0.65	0.33	0.68

The Precision values are shown in Table 4.9 and Fig. 4.10.

Comparison of precision reveals that LBP features gave the maximum result for NC (1.00) and NET (0.93) regions. These values are much higher than the second highest values. But for the remaining classes, the results were poor. The high values

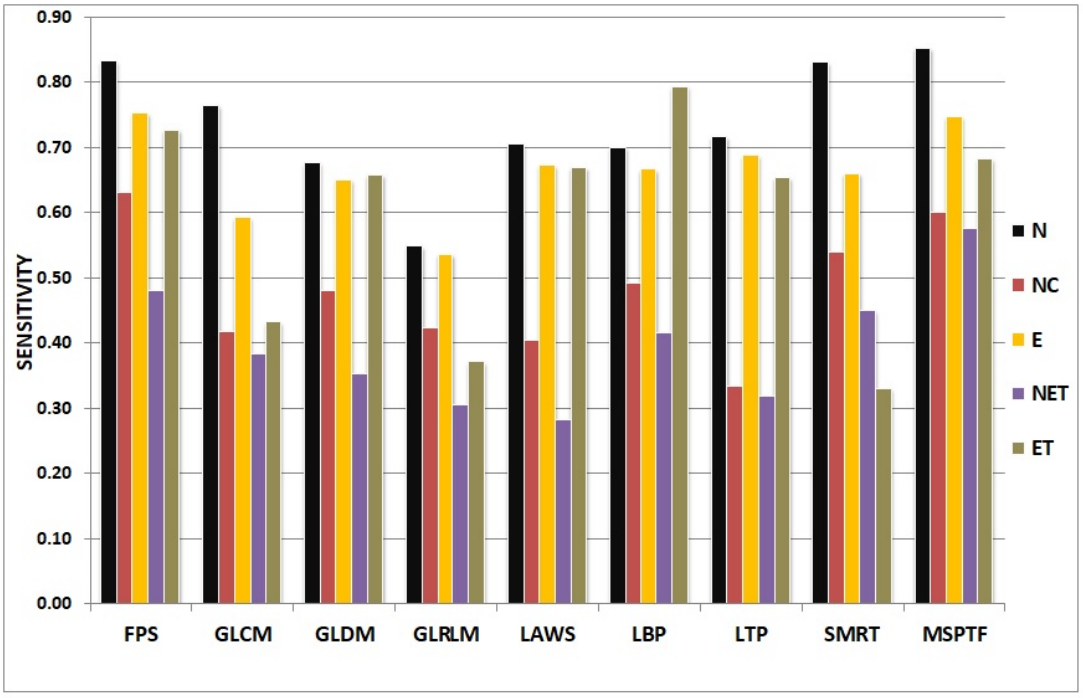

FIG. 4.9. Sensitivity of Bagged Tree classifier with Different Features

TABLE 4.9: Precision of Bagged Tree classifier with Different Features

CLASS	FPS	GLCM	GLDM	GLRLM	LAWS	LBP	LTP	SMRT	MSPTF
N	0.76	0.67	0.62	0.48	0.60	0.59	0.58	0.70	**0.77**
NC	0.70	0.59	0.61	0.49	0.59	**1.00**	0.59	0.62	0.67
E	0.70	0.49	0.63	0.46	0.58	0.62	0.63	0.54	**0.71**
NET	0.60	0.47	0.46	0.39	0.50	**0.93**	0.47	0.47	0.62
ET	0.70	0.53	0.55	0.40	0.57	0.54	0.55	0.49	**0.72**

for NC and NET and comparatively low precision for other classes indicates that many of the pixels that truly belonged to NC and NET got misclassified into other classes by the classifier when LBP features were used. MSPTF got the second highest precision for NET (0.62) and it performed consistently for all classes. It gave the best precision values for N, E and ET.

The comparison of Dice-Score can be viewed in Table 4.10 as well as in Fig. 4.11.

Comparison of Dice-Score, which is considered to be a more reliable measure

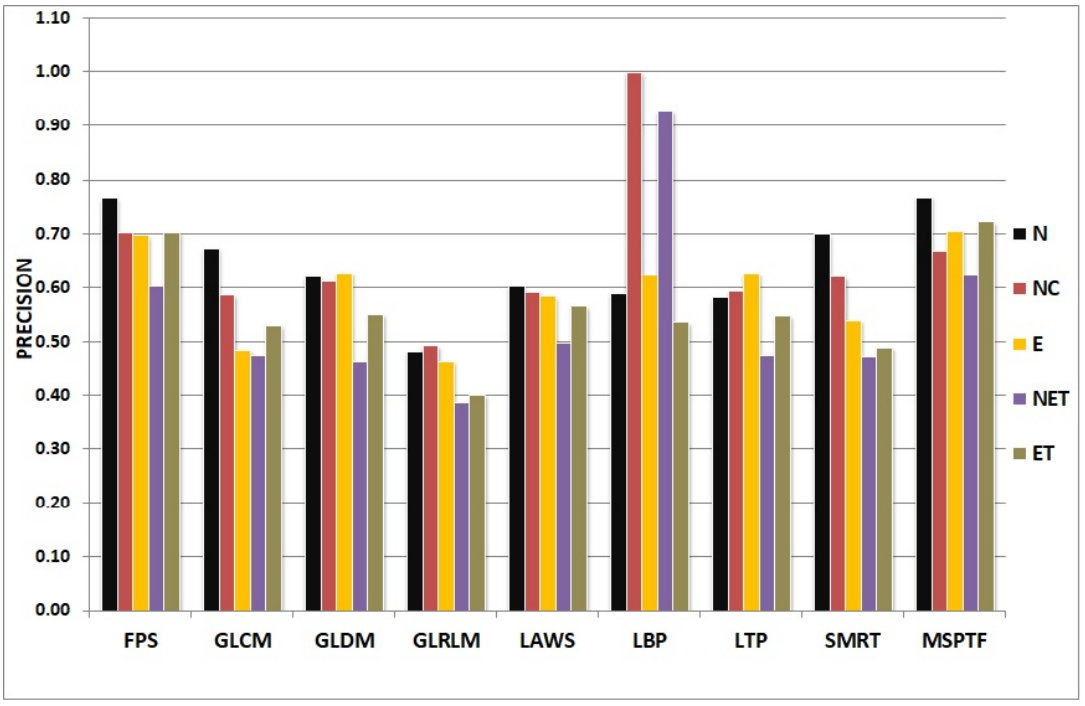

FIG. 4.10. Precision of Bagged Tree classifier with Different Features

TABLE 4.10: Dice-Score of Bagged Tree classifier with Different Features

CLASS	FPS	GLCM	GLDM	GLRLM	LAWS	LBP	LTP	SMRT	MSPTF
N	**0.80**	0.72	0.65	0.51	0.65	0.64	0.64	0.76	**0.80**
NC	**0.66**	0.49	0.54	0.46	0.48	**0.66**	0.43	0.58	0.63
E	0.72	0.53	0.64	0.50	0.62	0.64	0.66	0.59	**0.73**
NET	0.53	0.42	0.40	0.34	0.36	0.57	0.38	0.46	**0.60**
ET	**0.71**	0.48	0.60	0.39	0.61	0.64	0.60	0.40	0.70

than the other two measures, reveals that the proposed MSPTF features outweighed all other features in classifying Normal, Edema and NET regions. For other classes too, the developed feature gave the second best Dice-Scores. The highest DS value for necrotic core was given by both FPS features and LBP features when bagged tree classifier was employed.

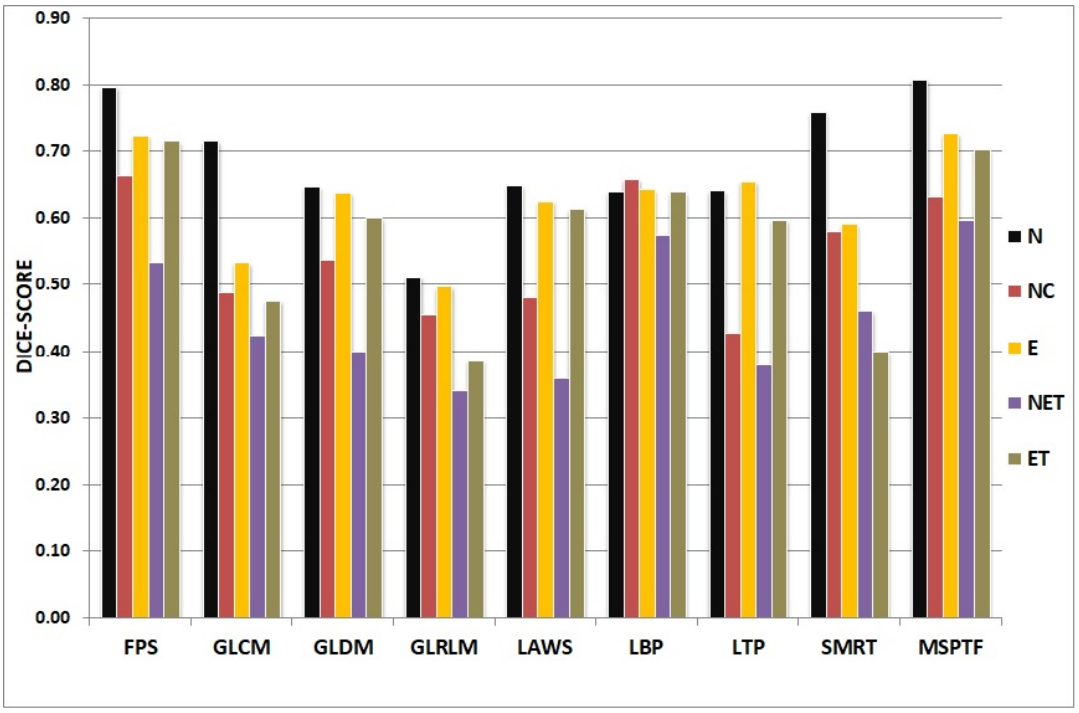

FIG. 4.11. Dice-Score of Bagged Tree classifier with Different Features

4.5 Conclusion

A new feature extraction technique considering a fusion of multiple MRI modalities is described in this chapter. Performance measures used to evaluate various results in the thesis are mentioned. The effectiveness of the proposed MSPTF features in classifying tumour sub-structures are evaluated with three classifiers. It is seen that MSPTF outperformed other features in classifying the tumour and its sub-regions. The objective of the work is to segment the tumour and its sub-regions. The next chapter describes in detail the developed HAC based segmentation technique.

Chapter 5

Hierarchical Agglomerative Clustering Based Combined Feature Selection and Classification

5.1 Introduction

A new classification based segmentation method is proposed in this chapter. A total of 592 features has been derived as discussed in Chapter 4. After the extraction of features, the next step usually performed is feature selection. During the feature selection stage, features that support the classification are filtered out from other features. The job of a good feature selection technique is two fold.

1. Remove the redundant features.

2. Remove the features that decelerate classification results.

In the newly proposed method, feature selection and classification are simultaneously performed to segment the tumour region.

Based on the number of classes, classification methods can be categorized as binary classification and multi-class classification. If the number of classes are only 2, binary classification techniques can be applied. But if the number of classes exceeds two, we should go for a multi-class classification technique. The scenario is presented in Fig. 5.1. Selection of features for multi-class classification is more complex than selecting features for binary classification. For example consider the scenario of selecting features for classifying n classes. There is a possibility that inclusion of the features that are good enough in distinguishing two classes, say class 1 and class 2, may worsen the system's capability in differentiating another pair of classes. Thus in multi-class classification, we may sometimes have to compromise on prominent features that are excellent in classifying a pair of class due to their adverse effect on another pair. The complication in multi-class classification can be reduced by making it a multi-layer binary classification. Fig. 5.2 shows the reconstruction of multi-class classification problem into a multi-layer binary classification problem. The reconstruction has given an opportunity to select best suitable feature set for each pair of class separately.

The proposed technique, which employs Hierarchical Agglomerative Clustering (HAC), decomposes multi-class classification problem into multi-layer binary classification. It also combines feature selection and classification. Thus a fusion of feature selection and classification is incorporated in the HAC based classifier. The proposed technique is evaluated by comparing the results with state of the art methods.

5.2 Hierarchical Agglomerative Clustering

HAC is a bottom up clustering technique in which initial number of clusters equals the total number of objects to be classified and merging of clusters are done in each step using a selected distance metric and linkage criteria. The algorithm proceeds until all the objects are clustered under a single cluster. Step by step merging of objects based on the distance metric, linkage criteria and the corresponding distance can be plotted using a dendrogram [91]. Fig. 5.3 shows a hierarchical agglomerative clustering of 30 objects. Initially each object is placed in to an individual cluster

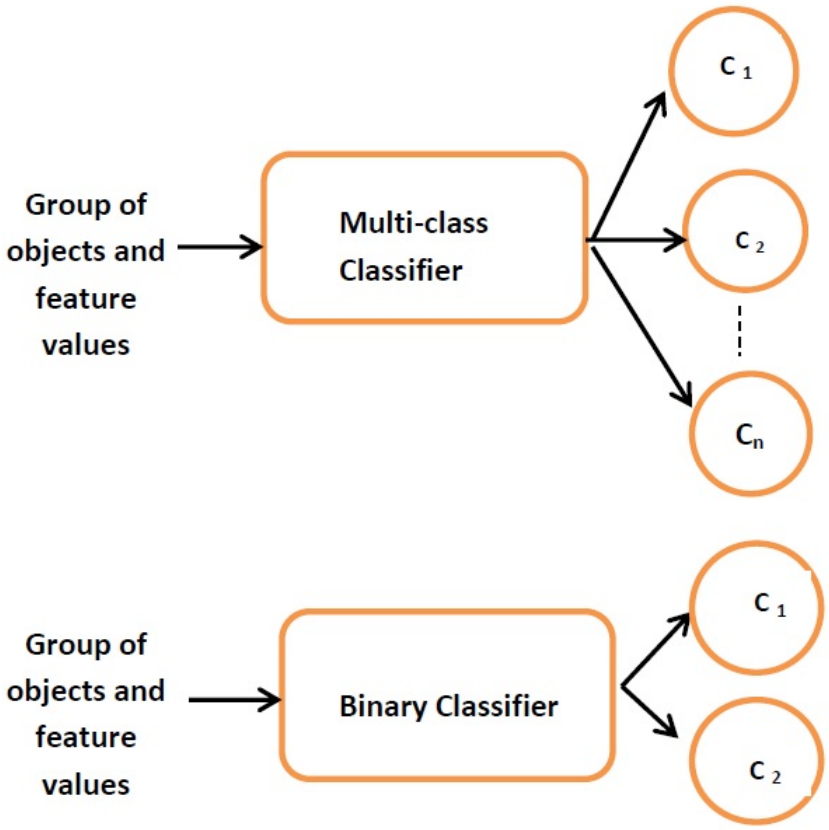

FIG. 5.1. Multi-class classifier and Binary Classifier

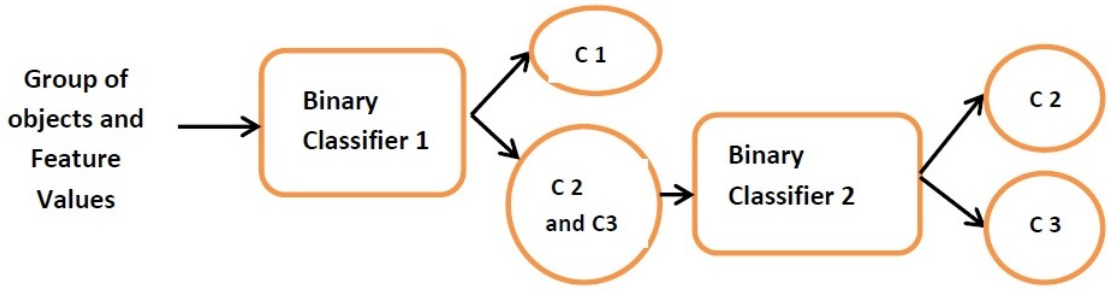

FIG. 5.2. Reconstruction of Multi-Class classification into Multi-Layer Binary Classification

so that the number of clusters equals the number of objects. In each step, objects with more similarity are combined to form a single cluster, thus reducing cluster numbers. The process is continued until all the objects come under a single cluster. Dendrogram gives a clear idea about the number of major clusters and inter-cluster distances.

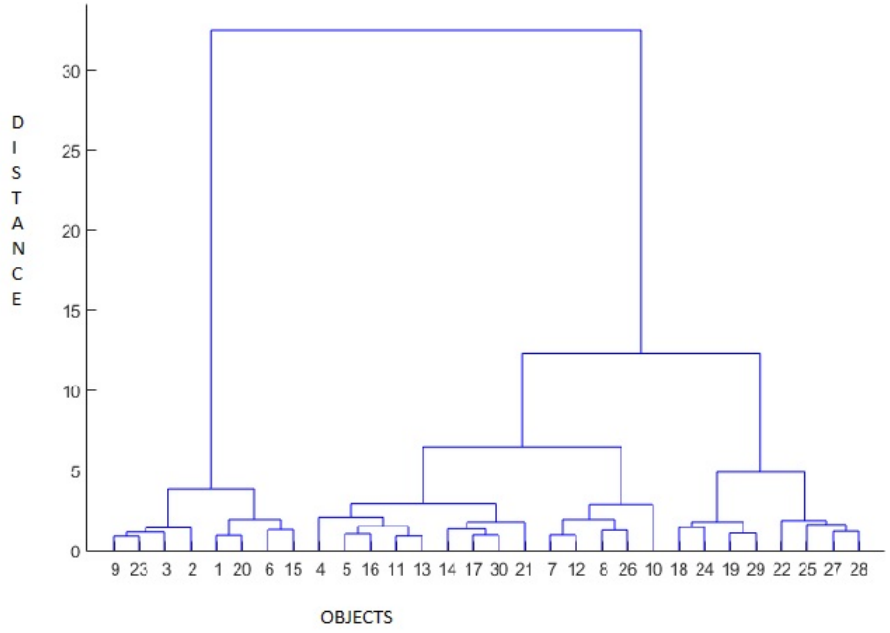

FIG. 5.3. Hierarchical Agglomerative Clustering of 30 objects

5.3 HAC based Feature Selection and Classification

A new method based on HAC, which is able to do feature selection and classification together, is developed. The developed method is a supervised classifier. Like any other supervised classifier, this method also has a learning phase. During this phase, classification models are created with the help of data with known class. The models are used in the next phase to reveal the class of a new data with unknown class. Feature selection and classification model creation are done according to the algorithm presented in Algorithm 2.

5.3.1 Learning Phase of the Developed Method

Learning of the proposed supervised classifier is carried out according to Algorithm 2.

Algorithm 2: HAC based Feature Selection and Creation of Classification Models

Input: 1. F - A matrix of order m × n (set of n features of m observation.)
Input: 2. L - Label vector of order m × 1.
Input: 3. k - number of distinct classes.
Input: 4. (k-1) number of separately trained SVMs.
Output: 1. S - A set of (k-1) pair of classes
Output: 2. $F^{'}$ - A set of (k-1) feature sets.

1: Organize the observations, corresponding features and labels according to the class in which they belong to form k groups $G(0)$ through $G(k-1)$
2: **for** i=0 to k-1 **do**
3: **for** j=1 to n **do**
4: AVGF(i,j)=mean(values of j^{th} feature in i^{th} class/group)
5: **end for**
6: **end for**
7: Cluster the data in the matrix 'AVGF' of order k × n using HAC technique . $S = HAC(AVGF)$
8: Step 7 gives a matrix S of dimension (k-1) × 2. Each row in S represents a pair of class. The distance between the member classes in each pair are also given as output by HAC.
9: **for** g=1 to k-1 **do**
10: For the pair of classes [S(g,1) ,S(g,2)],select a set of best features $F^{'}(g)$ that discriminate S(g,1) from S(g,2) through Step 11.
11: $F^{'}(g) = F_{ga}(g) \cap F_{pso}(g)$, where $F_{ga}(g)$, is the set of features selected by GA and $F_{pso}(g)$ is the set of features selected by PSO for the pair of classes [S(g,1),S(g,2)].
12: Create an SVM model, $SVM(g)$, for classifying S(g,1) and S(g,2) using the selected features from step 11.
13: **end for**

Algorithm 2 modifies multi-class classification scheme into multi-layer binary classification scheme. The algorithm has two distinct phases as given below.

1. HAC based Clustering

2. Feature Selection and Creation of SVM models

5.3.1.1 HAC based Clustering

The inputs to this phase are n features of m observations, the number of classes 'k' and true class label of each observation. The output will be a set S of pair of classes along with the distance between the member classes in each pair.

After getting the inputs, Algorithm 2 rearranges the input feature matrix according to the class of each data. The reorganization groups the features of data in the same class together. The mean value of each feature in each class is calculated. This results in a k $\times$ n matrix. HAC is performed to the resultant matrix. The output of HAC is a table S of (k-1) number of class pairs which are sorted according to the distance between member classes. S serves as a look up table during testing phase.

The next phase make use of the outputs of HAC to generate classification models.

5.3.1.2 Feature Selection and Creation of SVM Models

The class pairs provided by HAC will be ordered according to the distance between the member classes in the pair. For a pair of class in the table S, feature selection is carried out using both PSO and GA. A fusion of features selected by both the methods are used for discriminating member classes of that particular pair. Using the selected feature set, an SVM model is created. The outputs of this phase are listed below.

1. A set of (k-1) pair of classes sorted according to distance

2. A set of (k-1) number of feature sets, $F^{'}$

3. (k-1) number of SVMs corresponding to each pair of classes

.

5.3.2 Testing Phase of the Developed Method

Testing is carried out using the set of feature sets $F^{'}$ and the SVMs obtained during training. A set of observations and their features are given as input to the trained classifier. The classifier finds out the label of each observation. The procedure for testing is mentioned below.

1. Take SVM(k-1) to classify the set of observation.

2. Do the binary classification using the feature set $F^{'}(k-1)$.

3. Label the output of binary classification according to the look up table S.

4. Remove the labelled observations from the observation set.

5. Set k=k-1 and repeat the steps from 1 to 4 until k becomes 0

5.3.3 Application of the Developed Algorithm in the Study

During the learning phase, all features of the data extracted using conventional methods discussed in Chapter 3 and developed method described in Chapter 4 are presented to Algorithm 2. For every pixel, all the features are extracted since this method involves a pixel by pixel classification. Along with the extracted features of observations, their corresponding class labels as well as total number of classes k, which in the current study is 5, are also provided as inputs.

The algorithm starts by grouping the entire set of observations according to the class they belong (from class 0 through class 4). 5 different groups G^0 through G^4 are formed. Mean values of each feature in each group is computed to form a

5 × n matrix $AVGF$, where n is the number of features. The average value of a feature j in a particular group G^i is determined by the Equation 5.1.

$$AVGF_{i,j} = \frac{\sum_{z=1}^{l} G^i_{j,z}}{l} \tag{5.1}$$

where l is the number of observations in the i^{th} group and $G^i_{j,z}$ is the value of j^{th} feature of z^{th} observation in Group G^i.

The resultant matrix $AVGF$ is clustered using HAC technique. The chosen distance metric is euclidean. HAC outputs 4 pairs of class indices. The output of HAC is a dendrogram showing how the classes got paired during clustering and the distance between the member classes in a pair. The dendrogram obtained for the current study is shown in the Fig. 5.3. The pair of classes generated by HAC algorithm sorted according to the distance among them are shown in Table 5.1. Each class inside the class pair can be a class in its original form or a class formed by combining two or more classes. From Table 5.1, it is evident that distance between [3 4] is less than distance between [2 3,4] and so on. Single linkage algorithm is used for computing distance between clusters. In Fig. 5.4, the classes are numbered from 1 to 5 and they correspond to Normal, NC, E, NET and ET respectively. From Fig. 5.4 it clear that normal class has maximum distance from other classes. So it is comparatively easy to classify affected area from normal area. The classes with least distance is edema and non-enhancing tumour. Table 5.1 shows that normal class and the class formed by the combination of all other classes has the longest distance which is equal to 0.0293, and hence can be classified easily. The next longest distance is 0.0168 between class 5 and the class formed by combining classes 2,3 and 4

The algorithm selects 4 set of features corresponding to each pair of classes. The feature set $F^{'}(g)$ for classifying the member classes of g^{th} pair is chosen using the Equation 5.2.

$$F^{'}(g) = F_{ga}[S(g,1), S(g,2)] \cap F_{pso}[S(g,1), S(g,2)] \tag{5.2}$$

where $F_{ga}[S(g,1), S(g,2)]$ and $F_{pso}[S(g,1), S(g,2)]$ are the sets of features selected by GA and PSO respectively for classifying the classes S(g,1) and S(g,2).

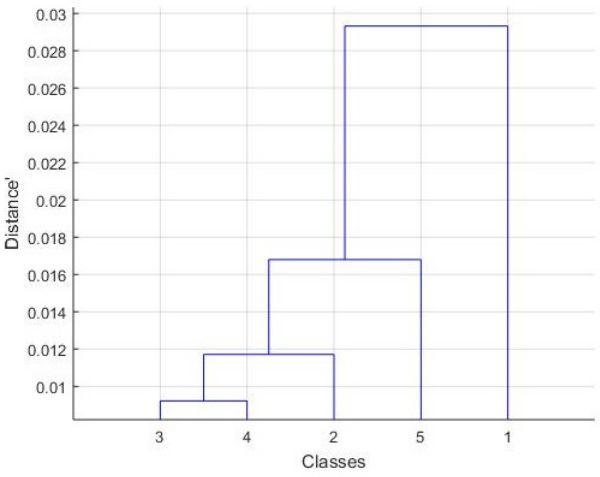

FIG. 5.4. Dendrogram Generated by HAC

TABLE 5.1: Pair of Classes Given by HAC Algorithm and Their Distances.

Pair of Classes	[3 4]	[2 { 3,4}]	[5 {2,3,4}]	[1 {5,2,3,4}]
Distance	0.0092	0.0117	0.0168	0.0293

Finally, using the four sets of feature sets, four SVM models are constructed. Thus each class pair generated using HAC has its own feature set and SVM model for classification. The following are the outcomes of learning phase.

1. Four pairs of classes and their distances

2. Four feature sets

3. Four binary SVM models

During the testing phase, all the outputs obtained during training are used to label the observation with unknown class. Using the feature set $F'(4)$ and SVM(4),

the initial observation set is classified. Based on the result, observations are categorized either as normal or belonging to other classes. SVM(3) and F(3) are used to perform the next binary classification. Enhancing tumour is separated by this classifier. The next binary classification by SVM(2) and F(2), differentiates NC. The final binary classification by SVM(1) is used for categorizing edema and non-enhancing tumour. An illustration of the testing phase is given in Fig. 5.5. The learning curves of GA and PSO are shown in Appendix B.

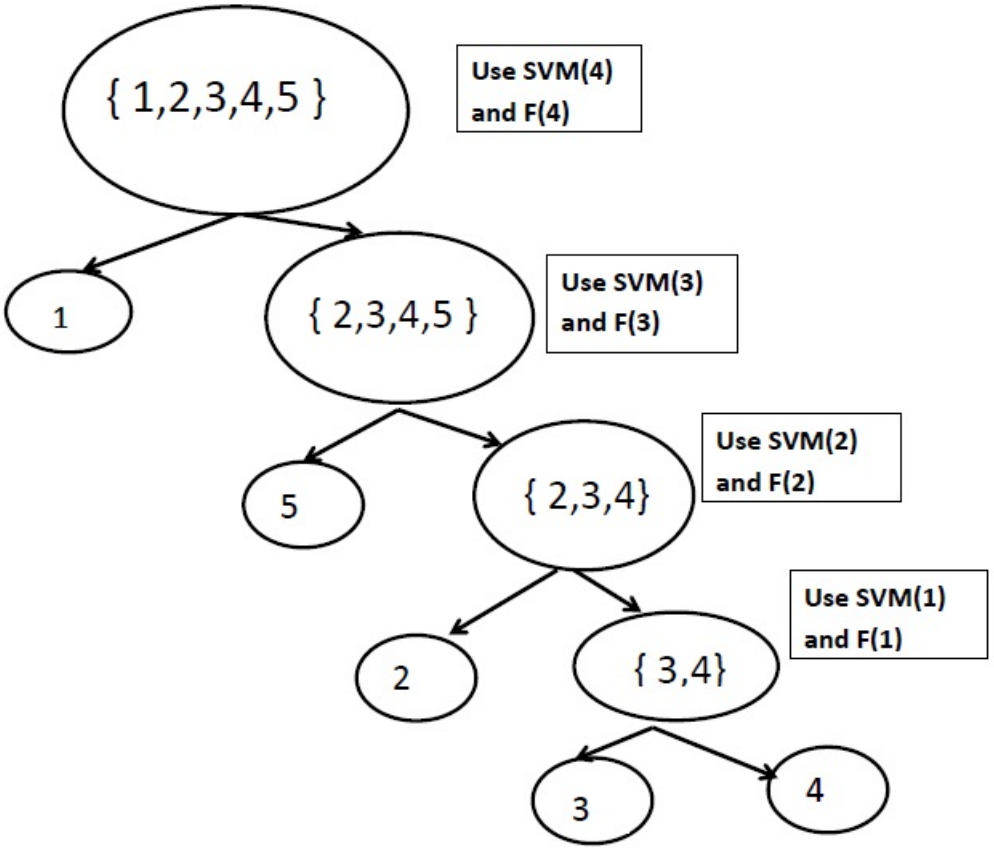

FIG. 5.5. Testing Procedure of the Developed Classifier

5.4 Results and Analysis

This section presents the results of the developed classifier. The comparison of the results obtained through the developed method with the results of conventional techniques are also presented. The selected conventional techniques use either GA or PSO for feature selection. The parameters as mentioned in Section 3.3.1 is used for

GA and in Section 3.3.2 is used for PSO. The classification is carried out using KNN, SVM Bagged tree and ANN classifiers. The parameters for the model construction of these classifiers are mentioned in Section 3.4.2.1, Section 3.4.2.2, Section 3.4.2.4 and Section 3.4.2.3 respectively. The metrics used for evaluation are Sensitivity, Precision and Dice-Score. The tables from Table 5.2 to 5.4 shows the results.

TABLE 5.2: Comparison of Sensitivity of Different Feature Selection - Classification Algorithm Combinations with the Developed Method.

CLASS	**GA+ SVM**	**PSO+ SVM**	**GA+ KNN**	**PSO+ KNN**	**GA+ BAGTREE**	**PSO+ BAGTREE**	**GA+ ANN**	**PSO+ ANN**	***NEW CLASSIFIER***
N	0.800	0.810	0.790	0.800	0.892	0.892	0.786	0.780	**0.910**
NC	0.689	0.701	0.685	0.690	0.669	0.677	0.676	0.685	**0.816**
E	0.805	0.813	0.744	0.754	0.810	0.816	0.740	0.750	**0.856**
NET	0.594	0.637	0.508	0.540	0.606	0.619	0.571	0.587	**0.794**
ET	0.798	0.798	0.798	0.811	0.793	0.793	0.789	**0.822**	**0.822**

By analysing Table.5.2, it is clear that all the other classes except NET have a sensitivity value greater than 0.8 when the developed classifier is used . The developed method gave a sensitivity value of 0.794 for NET, while PSO+SVM method gave 0.637 which is the maximum sensitivity for NET among conventional methods. But the sensitivity of ET using the developed method is same as the sensitivity value using PSO+ANN method. All other classes got an elevated sensitivity using the developed method. Fig. 5.6 shows the sensitivity results in 2-D chart.

Comparison of precision values of the developed method with other methods used in the study are shown in Table 5.3. Only Normal class and necrotic core has a precision which is greater than 0.8 when conventional methods are applied. All other classes fall below 0.8, among which NET has the worst result. Using PSO + SVM, the precision for NC class is found to be the maximum (0.903). But all other classes including the normal class has very less precision when PSO + SVM is used. The developed method gives a precision of 0.819 for NC which is less than the precision given by PSO + SVM and GA + SVM. This indicates that the feature set given by the intersection of GA selected features and PSO selected features resulted in a hyperplane which was not good as the hyperplane produced by GA features

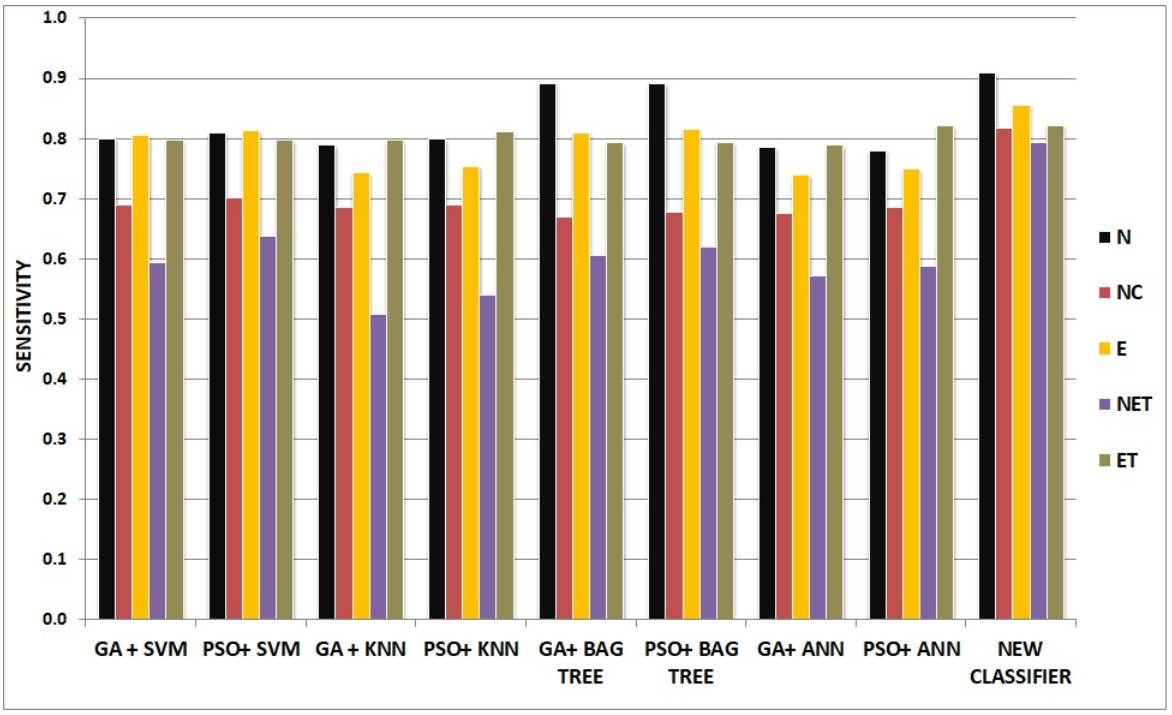

FIG. 5.6. Sensitivity Comparison of the Developed Method with Other Popular Methods

alone and PSO features alone for NC classification. But the remaining classes got an increased precision value using the developed method which means that either true positives increased or false positives decreased for all the classes except NC. The graphical view of the precision measures are shown in Fig. 5.7.

TABLE 5.3: Comparison of Precision of Different Feature Selection - Classification Algorithm Combinations with the Developed Method.

CLASS	**GA+ SVM**	**PSO+ SVM**	**GA+ KNN**	**PSO+ KNN**	**GA+ BAGTREE**	**PSO+ BAGTREE**	**GA+ ANN**	**PSO+ ANN**	***NEW CLASSIFIER***
N	0.723	0.738	0.806	0.811	0.837	0.842	0.794	0.807	**0.872**
NC	**0.902**	**0.903**	0.719	0.732	0.749	0.752	0.721	0.717	0.819
E	0.718	0.731	0.707	0.728	0.767	0.780	0.727	0.747	**0.870**
NET	0.719	0.739	0.561	0.588	0.705	0.699	0.594	0.615	**0.789**
ET	0.765	0.774	0.748	0.754	0.760	0.764	0.741	0.749	**0.851**

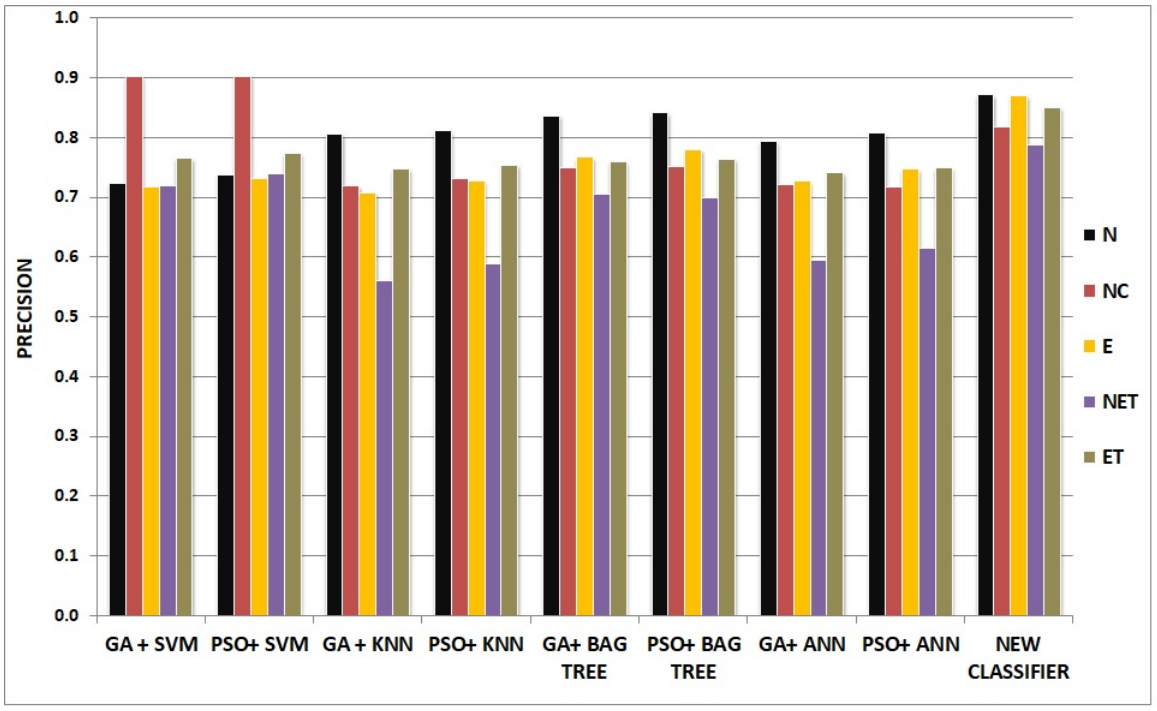

FIG. 5.7. Comparison of Precision of the developed method with other popular methods

Dice-Score is a more reliable measure which considers true positives, false positives and false negatives together. The Dice-Score results are shown in Table 5.4 and graphically in Fig. 5.8.

TABLE 5.4: Comparison of Dice-Score of Different Feature Selection - Classification Algorithm Combinations with the Developed Method.

CLASS	GA+ SVM	PSO+ SVM	GA+ KNN	PSO+ KNN	GA+ BAGTREE	PSO+ BAGTREE	GA+ ANN	PSO+ ANN	*NEW CLASSIFIER*
N	0.760	0.772	0.798	0.806	0.864	0.866	0.790	0.793	**0.890**
NC	0.781	0.789	0.701	0.711	0.707	0.713	0.697	0.700	**0.818**
E	0.759	0.770	0.725	0.741	0.788	0.798	0.733	0.749	**0.863**
NET	0.650	0.684	0.533	0.563	0.652	0.657	0.583	0.601	**0.791**
ET	0.781	0.786	0.772	0.782	0.776	0.779	0.764	0.784	**0.836**

The Dice-Score results show that all classes got the advantage by the developed classifier. NET region got the maximum increase in the Dice-Score value using the developed classifier. The developed method is able to lift the classification results

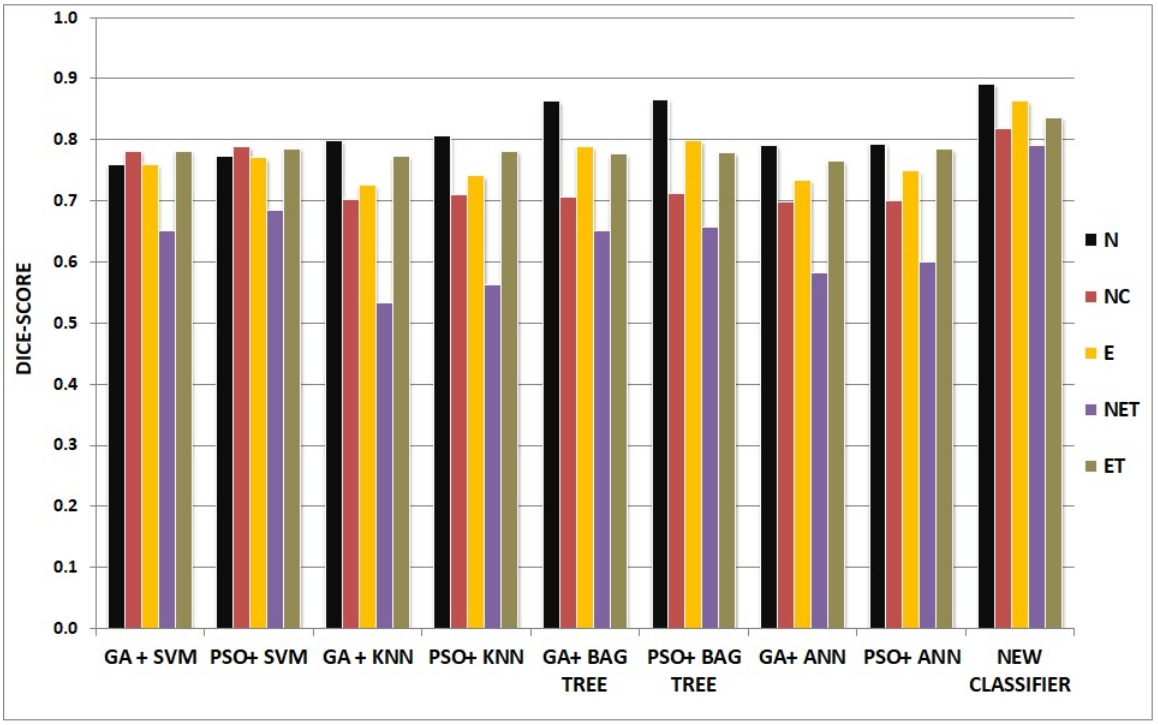

FIG. 5.8. Dice-Score comparison of the developed method with other popular methods

in various measures by dividing the multi-class classification into several binary classification stages. All the classes got the advantage of selecting separate feature set for every pair of classes.

5.5 Conclusion

A new supervised classifier that incorporates a fusion of feature selection and classification is developed in this chapter. Both learning phase and testing phase are described in detail. The application of the developed technique to segment the tumour and its related sub-regions from MRI is also presented. The results of comparison of developed method with various combinations of conventional methods are shown in tabular form and graphically. The Sensitivity, Precision and Dice-Score values highlights the performance of the developed method.

The Dice Score of normal region was 0.89 using the developed classifier. All other regions' Dice-Score lies in the range of 0.79 and 0.86. Though the developed

feature set and classifier elevated the segmentation results, medical application demands better result. A refinement technique is proposed in the next chapter as an attempt to improve segmentation results further.

Chapter 6

Classification Refinement using Wrong Sequence Search Algorithm

6.1 Introduction

This work proposes a classification based segmentation technique. Though the developed classification method described in Chapter 5 gave better classification results than other conventional methods for all regions, medical images demand better values to improve diagnosis and thus treatment planning. A method for refining the classification results and thus the segmentation process is proposed in this chapter. The proposed method is not a classifier on its own. It is suitable for correcting the misclassified pixels in an image whose sub-regions to be segmented follows a known pattern.

The presence of edema surrounding the brain tumour is common. Also tumour grow by dividing cells forming a closed shape. The presence of edema and growth of tumour core is shown in Fig. 6.1. Thus by analysing the pattern of pixels in all possible directions, the classification results can be improved. The proposed Wrong Sequence Search (WSS) technique passes through two phases which are listed below.

1. Finding out the probability of misclassification of a pixel

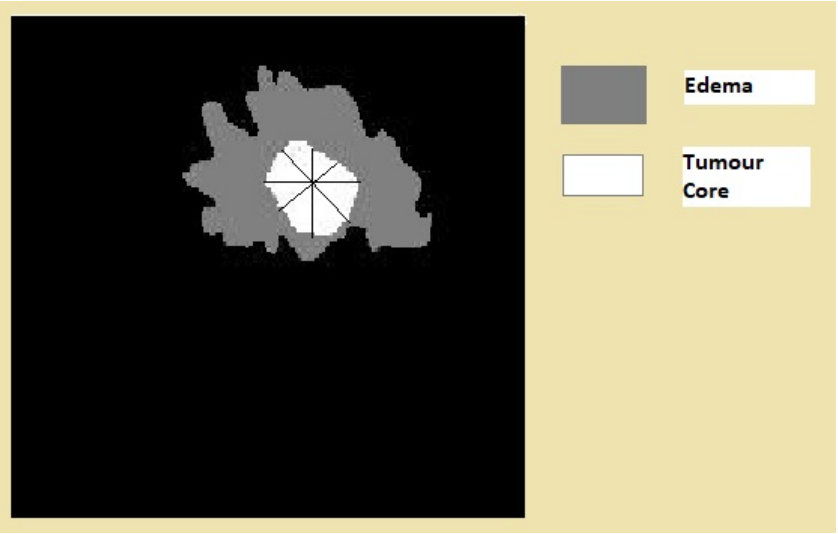

FIG. 6.1. Pattern of Presence of Edema and Tumour Core

2. Finding out the new class label for the pixel with a high misclassification probability

This method analyses patterns in all possible directions which necessitates keeping track of the location of the pixel as well as class label of neighbouring pixels given by the classifier. The method is detailed in the following section. Comparison of results before and after the application of the refinement technique is presented in Section 6.3. The qualitative results are shown in Section 6.6. The newly developed segmentation system is compared with state of the art methods in Section 6.6.

6.2 Wrong Sequence Search Algorithm

The classifier labels the pixels in various sub-regions of a tumour affected MRI. The labels given by the classifier for different regions are listed below

- Normal - 0
- NC - 1

- E - 2
- NET - 3
- ET - 4

The WSS algorithm in this work depends on the following domain specific knowledge.

1. A Tumour Core (NC+NET+ET) will be a closed region.
2. The presence of peri-tumoural edema is common in most of the cases.

The pattern of occurrences of normal, edema and tumour core are known. But the pattern of NC,NET and ET in the tumour core is unknown. The labels given by the classifier is modified as shown below before the application of WSS algorithm.

1. Normal - 0
2. Edema - 1
3. Tumour core - 2

WSS algorithm requires a tree data structure whose generation is explained in Algorithm 3 in Section 6.2.1. Wrong Sequences are defined in Section 6.2.2. Calculation of probability of misclassification of a pixel and the new label identification if required is described in Section 6.2.3

6.2.1 Octonary Tree

A tree is a hierarchical open data structure which has nodes and links. One of the node is termed as root, from which the tree originates. A node can have multiple children . In an octonary tree, the root node has exactly 8 child nodes and each child grows in a single direction. The eight different paths from the root node to leaf nodes in the octonary tree represents the 8 different directions from the central pixel. The central pixel corresponds to the root node, from where the pattern in eight possible directions are analysed. The central pixel and 8 possible directions (East, West, South, North, NorthEast, NorthWest, SouthEast and SouthWest) are shown in Fig. 6.2.

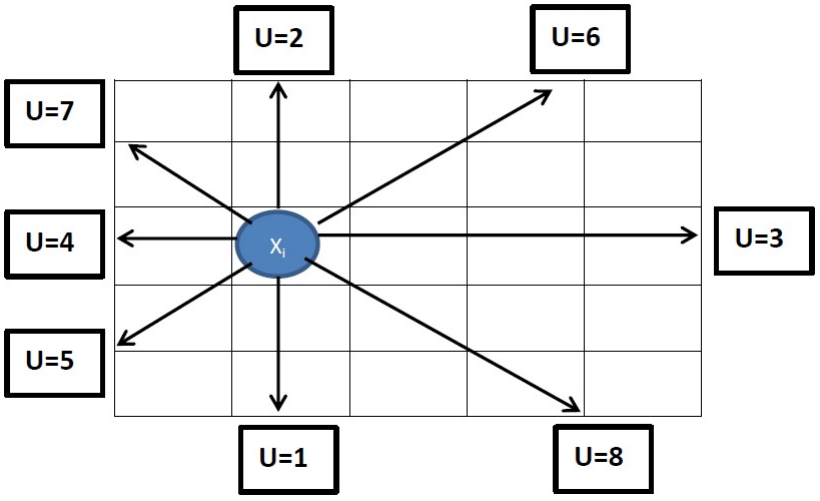

FIG. 6.2. Each Direction Corresponds to a Branch in the Octonary Tree

Octonary Tree Generation

Let D be the set $\{+1, -1, +d2, -d2, +(d2+1), -(d2+1), +(d2-1), -(d2-1)\}$, where each element in D represents a direction. $D(1) = +1$ represents south direction $D(2) = -1$ represents north direction etc. Generating a tree of depth ρ, for a pixel $X_{i,j}$ in an image of dimension d1 $\times$ d2 is bounded by the following conditions

$$1 \leq mod[kD(u), d1] \leq d1, \qquad \text{for } u = 1, 2 \tag{6.1}$$

$$1 \leq mod[kD(u), d2] \leq d2, \qquad \text{for } u = 3, 4 \tag{6.2}$$

$$\begin{aligned} 1 \leq mod[kD(u), d1] \leq d1 \quad and \\ 1 \leq mod[kD(u), d2] \leq d2, \text{for } u = 5, 6, 7, 8. \end{aligned} \tag{6.3}$$

k represents any positive integer that lies between 1 and the tree depth ρ. In Fig. 6.2 d1=5 and d2=5. The branches corresponding to u=4,5,7 cannot grow longer than 1, even though ρ is set 10, since it reached its boundary. Also the branch corresponding to direction u=1,2,6 and 8 cannot expand beyond a length of 2. Thus all the leaves of the tree corresponding to the boundary pixels will not be in the same level. Tree generation is presented in Algorithm 3. The tree generation has two phases as listed below.

1. A tree, T1,of depth 1 is generated with root node and 8 child nodes.

2. Eight unary trees (each node having only single child) of depth $\rho - 1$ are generated and attached to each leaf nodes of T1 making the depth of the tree ρ.

Algorithm 3: Tree Generation Algorithm

Input: The labelled image I returned by the classifier, The pixel position $X_{i,j}$ whose octonary tree is to be generated, The depth of the tree ρ

Output: A labelled octonary tree T1 of depth ρ corresponding to the input pixel $X_{i,j}$

1: Vectorize I to get the vector V. Let $X_{i,j}$ be placed in position p in V.
2: Root(T1)= Label[$V(p)$]
3: Attach Label($V[p + D(j)]$) to the root of T1 from left to right for j=1:8 . T1 (j) = Label($V[p + D(j)]$)
4: **for** j=1 to 8 **do**
5: **for** k=2 to ρ **do**
6: Append Label($V[p + kD(j)]$ to T1(j)
7: **end for**
8: **end for**

The generation of octonary tree using Algorithm 3 is depicted in Fig. 6.3.

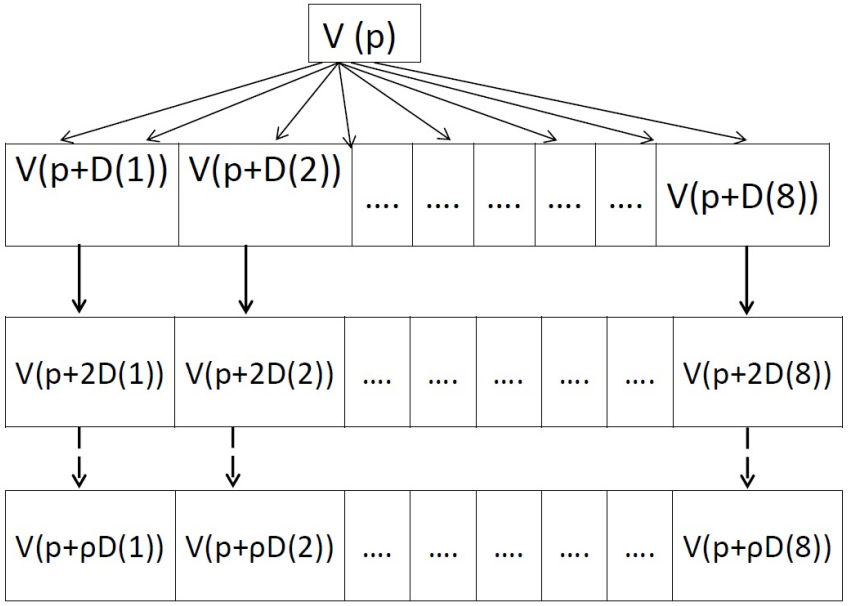

FIG. 6.3. Creating Octonary Tree for the node $X_{i,j}$

6.2.2 Defining Wrong Sequence

Defining possible sequences and wrong sequences are purely problem specific. In the current study we try to segment different regions of a tumour affected brain MRI. We are aware that the tumour grows by dividing cells. Thus irrespective of the size and shape, tumour core will be a closed region. Also the presence of peri-tumoural edema is expected in most cases. The edema separates normal cells from the affected cells. The presence of edema is not necessary in all cases. Considering all these facts, the wrong sequence and correct sequence can be inferred from all possible sequences. The list of entire possible sequences and wrong sequences of length 3 for this problem are given in Appendix C. A sample Octonary Tree and the wrong sequences in it are also depicted in Appendix C.

6.2.3 Classification Refinement

Classification refinement for a pixel $X_{i,j}$ is carried out in two steps. In the first step, the probability of misclassification (P_{rm}) is calculated. In the second step new class label for $X_{i,j}$ is found out if P_{rm} exceeds a fixed threshold. The algorithm for refinement is presented in Algorithm 4.

Algorithm 4: Wrong Sequence Search Based Classification Refinement Algorithm

Input: Octonary Tree for $X_{i,j}$, A fixed threshold θ, The current class (CC) of $X_{i,j}$ according to the classifier, Precision of CC returned by the classifier, Possible Sequence set PS, Wrong Sequence set WS

Output: Refined Classification Result for $X_{i,j}$

1: Count Wrong Sequences in the tree (N_{ws}) using the Octonary Tree and the set WS.
2: Compute the probability (P_{rm}) of misclassification of $X_{i,j}$ using the equation 6.4
3: **if** $P_{rm} > \theta$ **then**
4: Find out the new class for $X_{i,j}$ using Step 4 and Step 5
5: Compute the likelyhood of $X_{i,j}$ belonging to class C_i using the Equation 6.5.
6: The class with maximum likelyhood value is chosen as the new class for $X_{i,j}$.
7: **end if**

The wrong sequence based refinement algorithm is detailed in the following subsections.

6.2.3.1 Computing Probability of Misclassification

Once the octonary tree of depth ρ is generated and each node of it is initialized with the label provided by the classifier, Algorithm 4 is executed for each pixel $X_{i,j}$ to find out the probability of misclassification P_{rm}. P_{rm} depends on the number of wrong sequences (N_{ws}) in the tree and precision of the Current Class (CC) in which $X_{i,j}$ belongs. The precision measure is chosen since it is a function of FP. The Equation 6.4 is used to find P_{rm}. In the equation, k represents a constant, whose value equals 0.10875. The probability exceeding a certain threshold θ indicates that the classification of $X_{i,j}$ is wrong and the new class of $X_{i,j}$ needs to be found out. Trial and error method is used to find the value of θ.

$$P_{rm} = \frac{k * N_{ws}}{Precision(CC)} \tag{6.4}$$

6.2.3.2 Finding out New Class Label

The Algorithm 4 also finds out new class for $X_{i,j}$. The decision is based on the class labels of neighbouring nodes. The closer neighbours get more weight in decision

making. The probability of $X_{i,j}$ belonging in a class C_i is decided by the the total number of neighbourhood nodes which are in C_i in each radial distance. Equation 6.5 gives a value representing the likelihood of $X_{i,j}$ to belong to a class C_i and the class with maximum likelihood is chosen as the new class of $X_{i,j}$.

$$Likelihood(C_i) = \sum_{j=1}^{3} \frac{1}{j} NN(i,j) \tag{6.5}$$

$NN(i,j)$ is the number of nodes with class i in j^{th} radial distance.

6.3 Results and Analysis

This section presents the differences in performance measures before and after the application of refinement technique. Unlike in previous chapters, here we consider only 3 classes. Normal, Edema and Tumour core (Necrotic core + Enhancing tumour + Non-enhancing tumour). For changing the 3-class (Normal, Edema, Tumour) result into 5-class (Normal, Edema, Necrotic core, Enhancing Tumour ,Non-enhancing tumour) result, a KNN classifier is used. The KNN classifier works after the refinement, and it is used to classify the pixels which moved from other classes to Tumour core after the refinement process. For testing the effectiveness of the refinement technique, 10 MRI images were randomly chosen and classified using the classifier developed in Chapter 5, (PSO + SVM) classifier, (PSO+BAGTREE) classifier and (GA+ KNN) classifier. The results obtained from each classifier is fed to the refinement algorithm. A comparison between the results obtained before and after the application of the refinement technique is also carried out. Precision, Sensitivity and Dice-Score of the three classes before and after the application of refinement technique are shown from Table 6.1 to 6.3. The comparison is also given as 2-dimensional chart in Fig. 6.4 to 6.6.

The comparison results in Table 6.1 show that after the application of refinement technique, the developed classifier's sensitivity values improved for all the three classes. Increased value of sensitivity indicates that either true positives increased or false negatives decreased. The sensitivity of normal class increased from 0.91 to

TABLE 6.1: Sensitivity Comparison of Various Classifiers Before and After the Application of Refinement Technique

CLASS	**GA+KNN**		**PSO+SVM**		**PSO+ BAGTREE**		**Developed Classifier**	
	Before	**After**	**Before**	**After**	**Before**	**After**	**Before**	**After**
Normal	0.79	0.81	0.81	0.83	0.89	0.91	**0.91**	**0.93**
Edema	0.74	0.77	0.81	0.85	0.82	0.86	**0.86**	**0.92**
Tumour	0.84	0.84	0.85	0.85	0.87	0.88	**0.91**	**0.94**

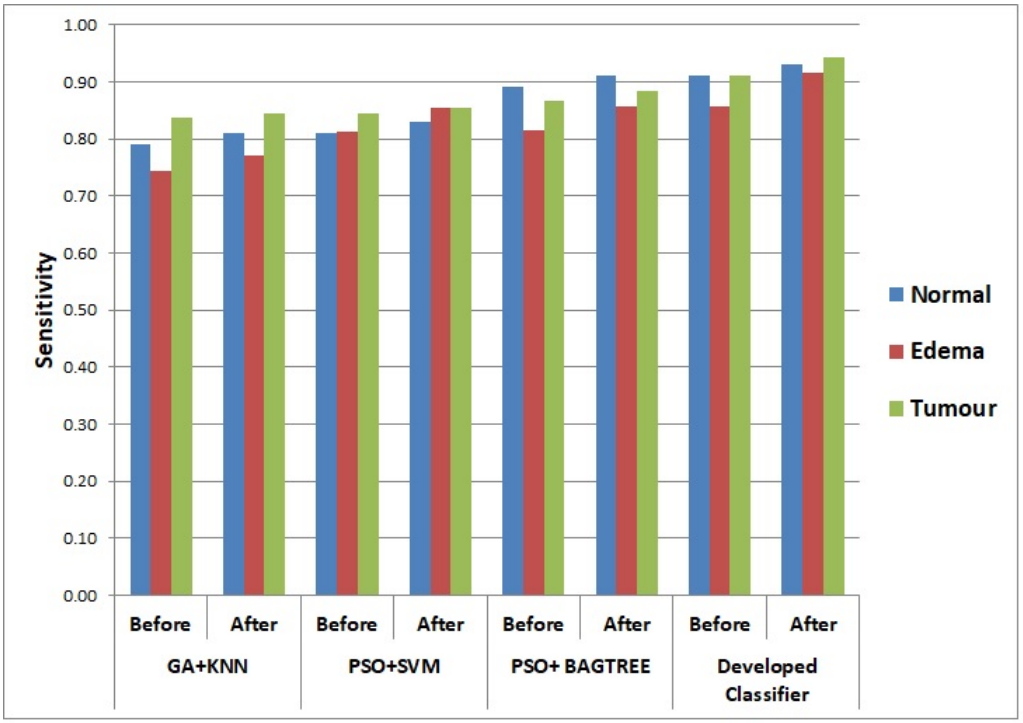

FIG. 6.4. Sensitivity Comparison of Various Classifiers Before and After the Application of Refinement Technique

0.93. The net improvement in sensitivity is 2 %. For the class Edema, the developed classifier's sensitivity improved remarkably from 0.86 to 0.92. All the other classifiers' sensitivity for normal and edema classes improved in the same manner. PSO+BAGTREE classifier gave an improved sensitivity for tumour region too.

The effect of refinement technique on the classification results using precision values is shown in Table 6.2. For all classes the largest variation before and after

TABLE 6.2: Comparison of Precision of Various Classifiers Before and After the Application of Refinement Technique

CLASS	GA+KNN		PSO+SVM		PSO+ BAGTREE		Developed Classifier	
	Before	After	Before	After	Before	After	Before	After
Normal	0.81	0.81	0.74	0.76	0.84	0.86	**0.87**	**0.91**
Edema	0.71	0.73	0.73	0.76	0.78	0.81	**0.87**	**0.91**
Tumour	0.85	0.87	0.93	0.95	0.91	0.94	**0.92**	**0.95**

refinement is given by the developed classifier. The same is shown as a 2-D chart in Fig. 6.5.

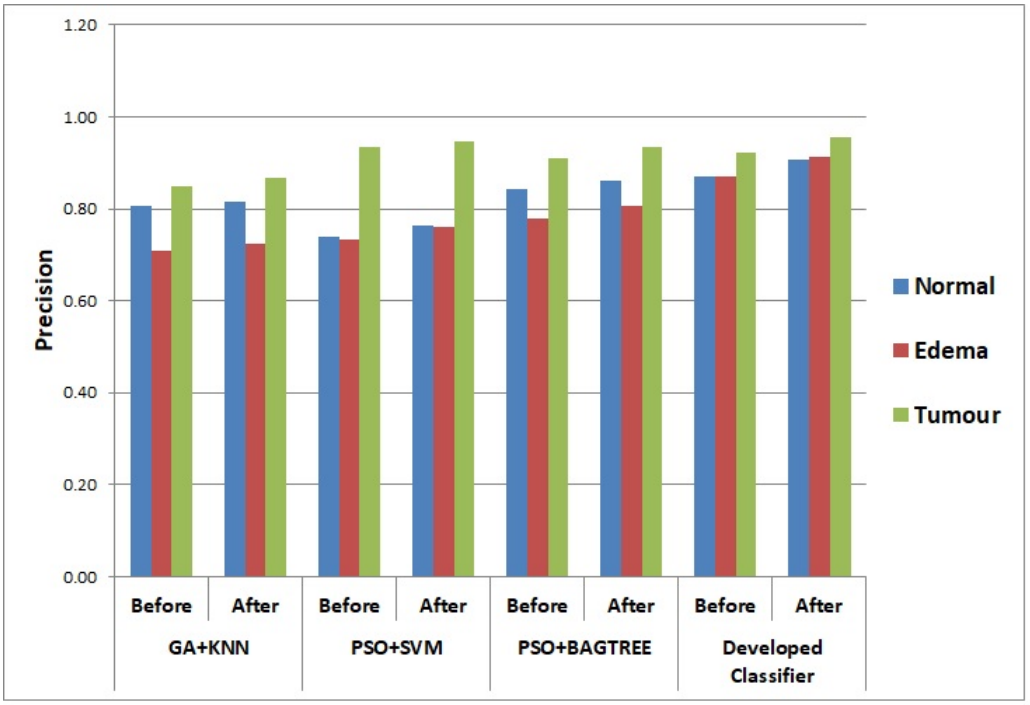

FIG. 6.5. Precision Comparison of Various Classifiers Before and After the Application of Refinement Technique

The Dice-Score variation after refinement is shown in Table 6.3. It is evident that refinement technique produced positive results. The same can be viewed as graph in Fig. 6.6.

However this refinement technique does not address the problem of misclassification inside the Tumour Core (among NC, ET and NET).

TABLE 6.3: Comparison of Dice-Score of Various Classifiers Before and After the Application of Refinement Technique

CLASS	GA+KNN		PSO+SVM		PSO+ BAGTREE		Developed Classifier	
	Before	After	Before	After	Before	After	Before	After
Normal	0.80	0.81	0.77	0.80	0.87	0.89	**0.89**	**0.92**
Edema	0.73	0.75	0.77	0.80	0.80	0.83	**0.86**	**0.92**
Tumour	0.84	0.86	0.89	0.90	0.89	0.91	**0.92**	**0.95**

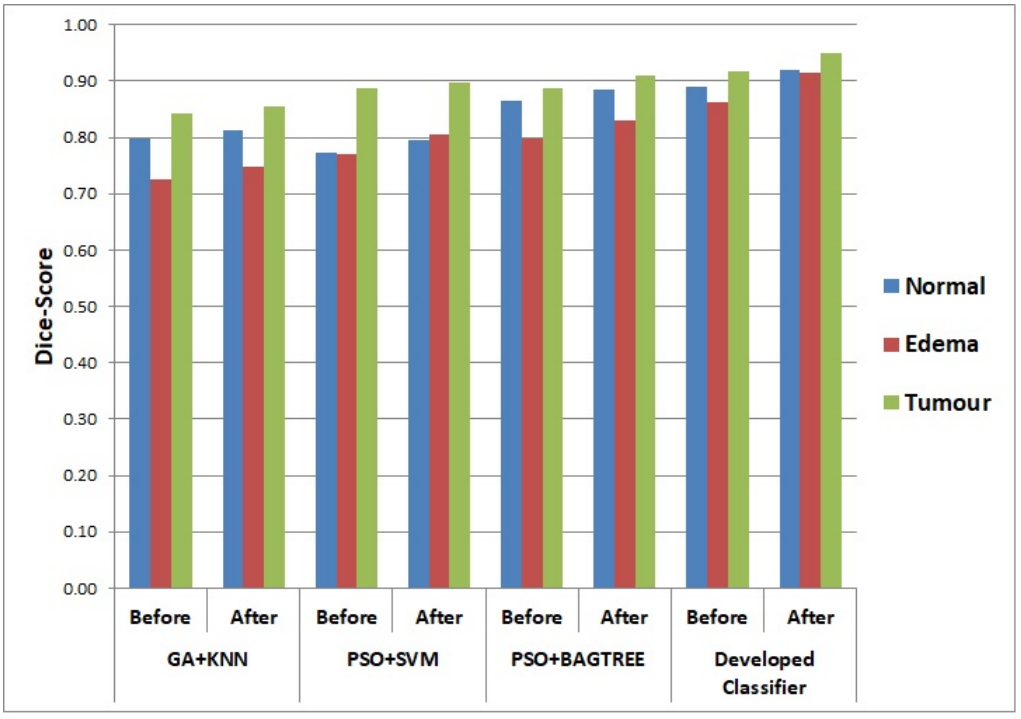

FIG. 6.6. Dice-Score Comparison of Various Classifiers Before and After the Application of Refinement Technique

6.4 Conversion of Refinement Result into a 5-Class Result

Although the refinement technique improved the classification results of the three classes, Normal, Edema and Tumour core (Necrotic Core+ Enhancing Tumour+ Non-Enhancing Tumour), we are still not sure about the impact of refinement on the classes NC, ET and NET if considered separately. To further classify Tumour

Core into NC, ET and NET, a KNN classifier is applied to the refined results to produce a result in 5-class mode. The final results after the KNN classification are shown from Table 6.4 to 6.6. The bar charts of the results are shown from Fig. 6.7 to 6.9.

TABLE 6.4: Sensitivity Comparison of the Classification Results Before and After Refinement

CLASS	**GA+KNN**		**PSO+SVM**		**PSO+ BAGTREE**		**Developed Classifier**	
	Before	**After**	**Before**	**After**	**Before**	**After**	**Before**	**After**
N	0.79	0.81	0.81	0.83	0.89	0.91	**0.91**	**0.93**
NC	0.68	0.68	0.70	0.70	0.68	0.68	**0.82**	**0.82**
E	0.74	0.77	0.81	0.85	0.82	0.86	**0.86**	**0.92**
NET	0.51	0.53	0.64	0.67	0.62	0.68	**0.79**	**0.84**
ET	0.80	0.81	0.80	0.80	0.79	0.79	**0.82**	**0.87**

TABLE 6.5: Comparison of Precision of the Classification Done Using Different Techniques Before and After the Refinement

CLASS	**GA+KNN**		**PSO+SVM**		**PSO+ BAGTREE**		**Developed Classifier**	
	Before	**After**	**Before**	**After**	**Before**	**After**	**Before**	**After**
N	0.81	0.81	0.74	0.76	0.84	0.86	**0.87**	**0.91**
NC	0.72	0.73	0.90	0.90	0.75	0.76	**0.82**	**0.84**
E	0.71	0.73	0.73	0.76	0.78	0.81	**0.87**	**0.91**
NET	0.56	0.58	0.74	0.75	0.70	0.75	**0.79**	**0.83**
ET	0.75	0.76	0.77	0.79	0.76	0.79	**0.85**	**0.89**

Although the refinement technique does not consider the subdivision of the tumour into sub-regions (NC,ET and NET), the Table 6.4 through 6.6 shows that this technique has enhanced the overall results. Hence it can be concluded from Fig. 6.7 to 6.9 that the developed classifier's Sensitivity, Precision and Dice-Score values of all regions have increased after refinement. For other classifiers, the results either increased or remained same.

TABLE 6.6: Dice-Score Comparison of the Classification Results Before and After the Apllication of Refinement Technique

CLASS	**GA+KNN**		**PSO+SVM**		**PSO+ BAGTREE**		**Developed Classifier**	
	Before	**After**	**Before**	**After**	**Before**	**After**	**Before**	**After**
N	0.80	0.81	0.77	0.79	0.87	0.89	**0.89**	**0.92**
NC	0.70	0.71	0.79	0.79	0.71	0.71	**0.82**	**0.83**
E	0.73	0.75	0.77	0.80	0.80	0.83	**0.86**	**0.92**
NET	0.53	0.55	0.68	0.71	0.66	0.71	**0.79**	**0.83**
ET	0.77	0.78	0.79	0.80	0.78	0.79	**0.84**	**0.88**

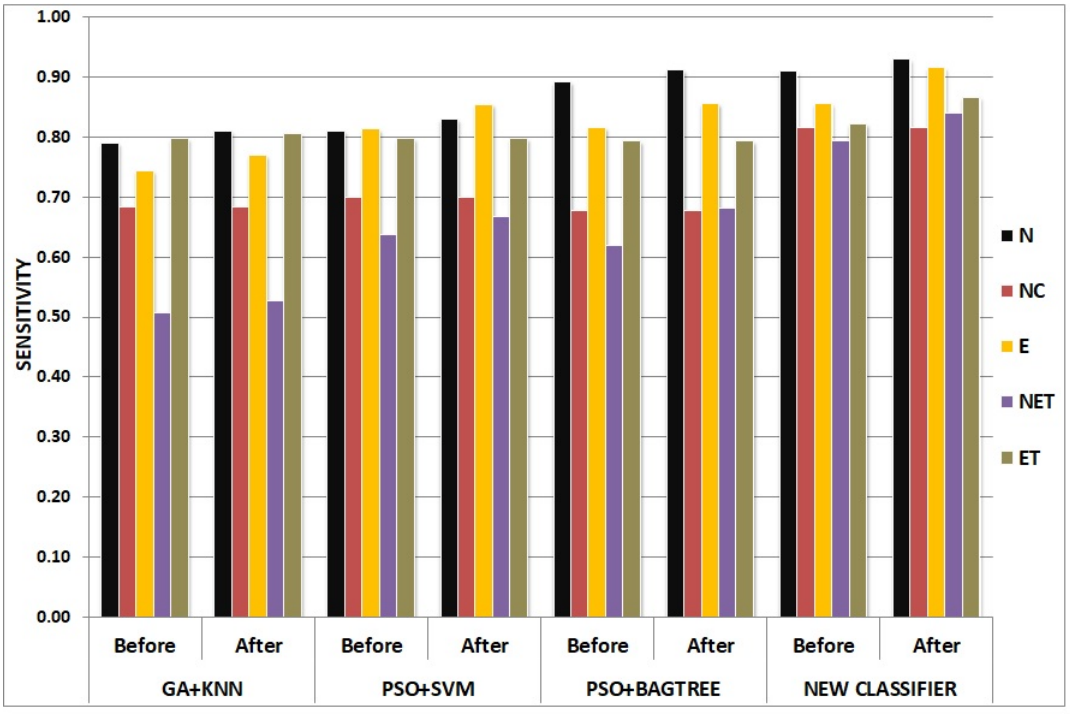

FIG. 6.7. Sensitivity Comparison of Various Classifiers Before and After the Application of Refinement Technique

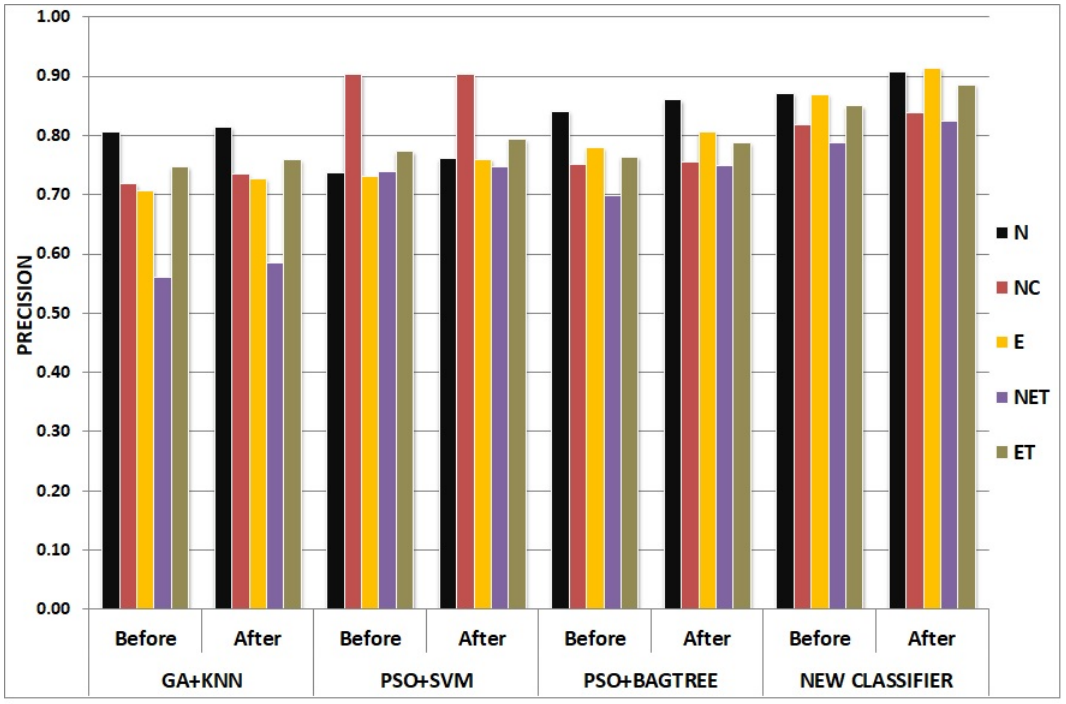

FIG. 6.8. Comparison of Precision of Various Classifiers Before and After the Application of Refinement Technique

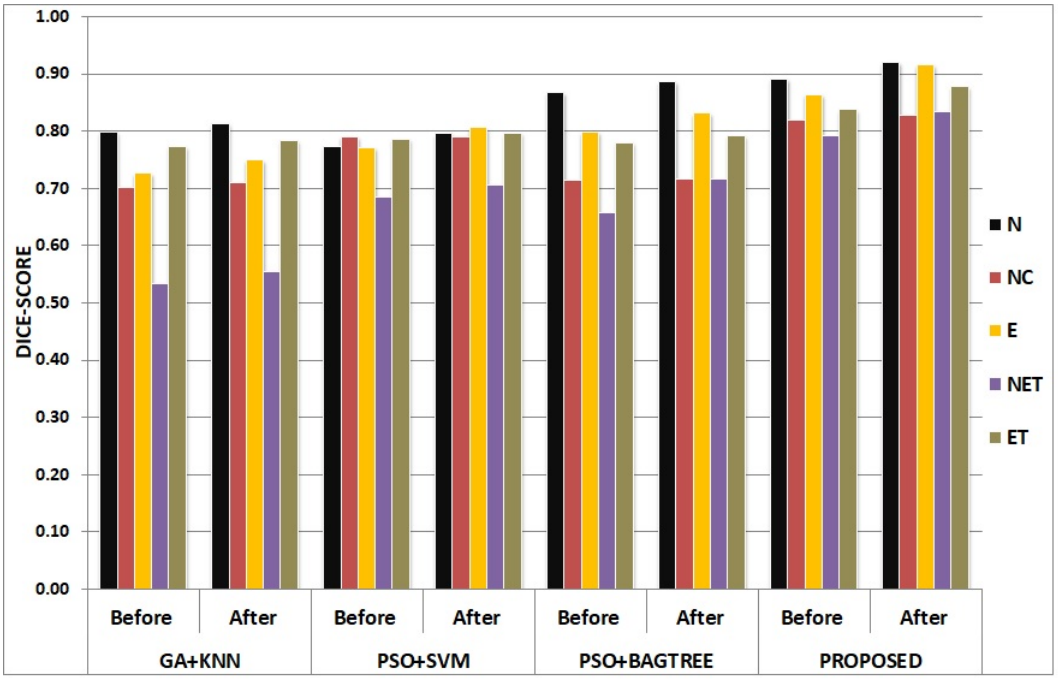

FIG. 6.9. Dice-Score Comparison of Various Classifiers Before and After the Application of Refinement Technique

6.5 Qualitative Results

The tumour sub-regions are labelled as shown in the sample image Fig. 6.10. The qualitative segmentation results obtained for five different cases is presented from Fig. 6.11 to 6.15. The features used for segmentation include the conventional features described in Chapter 3 and the newly developed MSPTF. The images from Fig. 6.11 (b) to 6.15 (b) and Fig. 6.11 (c) to 6.15 (c) represent the segmentation results corresponding to KNN classifier and the newly developed HAC based classifier respectively. The results after refinement are shown in Fig. 6.11 (d) to 6.15 (d). The ground truths are presented in the images from Fig. 6.11 (e) to 6.15 (e).

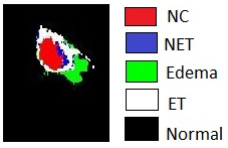

FIG. 6.10. Labels of Tumour Sub-regions

FIG. 6.11. Qualitative Results of Case 1.(a) FLAIR Image. (b) Result of KNN Classifier. (c) Result of Developed Classifier. (d) Result After the Refinement Technique. (e) Ground Truth

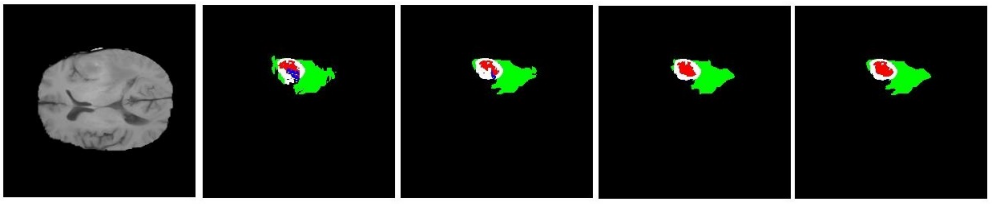

FIG. 6.12. Qualitative Results of Case 2.(a) T1 weighted Image. (b) Result of KNN Classifier. (c) Result of Developed Classifier. (d) Result After the Refinement Technique. (e) Ground Truth

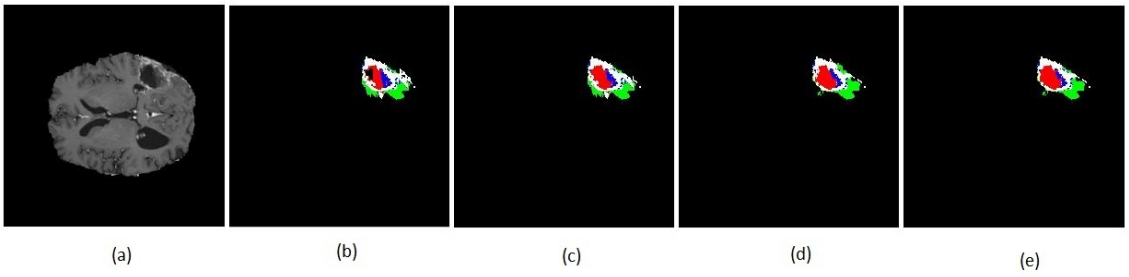

FIG. 6.13. Qualitative Results of Case 3.(a) T1 Contrast Image. (b) Result of KNN Classifier. (c) Result of Developed Classifier. (d) Result After the Refinement Technique. (e) Ground Truth

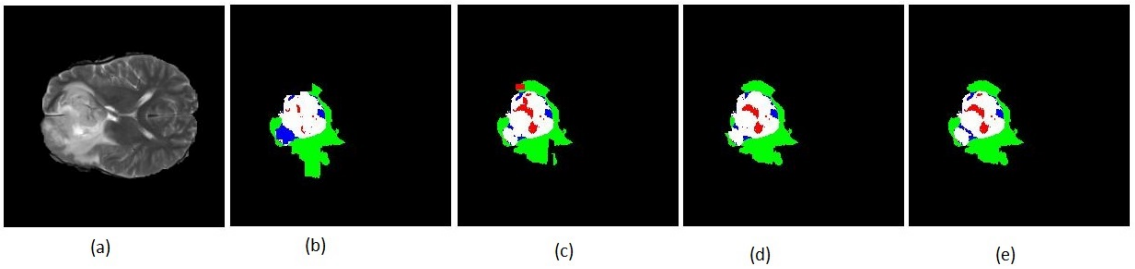

FIG. 6.14. Qualitative Results of Case 4.(a) T2 weighted Image. (b) Result of KNN Classifier. (c) Result of Developed Classifier. (d) Result After the Refinement Technique. (e) Ground Truth

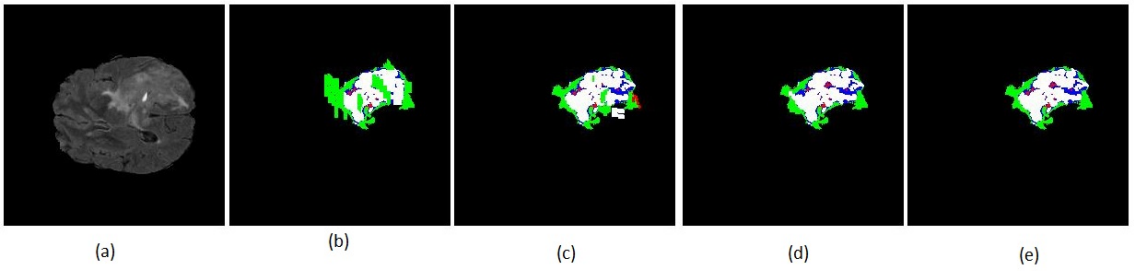

FIG. 6.15. Qualitative Results of Case 5.(a) FLAIR Image. (b) Result of KNN Classifier. (c) Result of Developed Classifier. (d) Result After the Refinement Technique. (e) Ground Truth

6.6 Comparison with State of the Art Methods

The time complexity of the developed algorithm during the various phases is given in Table 6.7. The testing phase was less complex than training phase. During training phase, along with MSPTF all the features mentioned in Chapter 3 were extracted. In testing phase only the selected features were extracted. The feature selection and creation of SVM models were carried out in training phase where as in testing phase the classification is done with the previously created SVM models.

TABLE 6.7: Time Complexity of the Developed Segmentation Algorithm

Machine Specification	**Phases**	**Training Time Complexity**	**Testing Time Complexity**
Processor: **Intel Core i3 with 1.8GHz speed** Internal RAM: **4GB**	Feature Extraction	1230 s	325 s
	HAC based Feature Selection and Classification	12900 s	432 s
	Refinement	1245 s	455 s

Comparison of the developed segmentation system with state of the art methods are shown in Table 6.8. Some methods segmented the whole tumour, which consists of edema, necrotic core, enhancing tumour and non-enhancing tumour. The four regions within the complete tumour are not separated by this method. Some literature segmented the tumour core which consists of non-enhancing tumour, enhancing tumour and necrotic core. Edema could be separated by these methods. In some literature enhancing tumour segmentation was also done. The developed method segments the entire image into 5 separate regions. In Table 6.8 the regions for which results are not available are marked as NA.

TABLE 6.8: Comparison of the Dice-Score values of the Developed Segmentation System with State of the Art Methods

Method	**Complete Tumour**	**Tumour Core**	**Enhacinng Tumour**
Localized Acive Contour Model [23]	0.91	NA	NA
Automatic Selection of Active Contour Models [24]	0.93	NA	NA
Active Contours Driven by Cockoo Search [28]	0.95	NA	NA
Outlier Detection with Random Walker [32]	NA	0.81	0.72
Convolutional Neural Network [38]	0.84	0.72	0.62
Multi-fractal Texture Features [40]	NA	0.9	NA
Sparse Representation [44]	0.8	0.56	0.56
Local Independent Projection [53]	0.84	0.68	0.58
Cellular Automata and Tumour Cut [65]	0.84	0.79	NA
Hybrid Clustering[66]	NA	0.88	NA
Concatenated and Connected Random Forest [71]	0.89	0.8	0.76
Ensemble of Multiple Models [92]	0.9	0.79	0.73
Cascaded Anisotropic CNN [93]	0.87	0.77	0.78
Conditional Adversarial Network [94]	0.7	0.55	0.4
Newly Developed Segmentation Scheme	**0.95**	**0.95**	**0.88**

6.7 Conclusion

The development of a refinement technique to further improve the classification result is discussed in this chapter. From the results it is evident that this technique

has improved the values of Precision, Sensitivity and Dice-Score of the newly developed classifier. In the case of other classifiers, the values have either improved or remained same for various sub-regions. The comparison of the developed method with state of art methods is also presented in this chapter.

Chapter 7

Conclusion and Future Work

The chapter presents the summary of the work carried out and the conclusions drawn. Important contributions of the thesis and the scope for further research in this area is also presented in this chapter.

7.1 Feature Extraction

Literature survey presented in Chapter 2 clearly indicates that conventional feature extraction techniques gather information from a single image. The feature extraction technique developed in Chapter 4 generates features considering multiple modalities of MRI. The difference of intensities of a particular pixel occurring in various modalities are converted into features. The intensity variations of a particular type of tissue in different modality make the newly proposed feature a strong one in discriminating the sub-regions of tumorous MRI. This is evident from the comparison tables of the new features with the conventional features.

7.2 Segmentation Through Classification

The newly developed segmentation algorithm is explained in detail in Chapter 5. This method is a combination of feature selection and classification. The final

classification is evolved through several layers of binary classifications. Thus the complexity of considering multiple classes in a single step is avoided. For each binary classification, the feature set and classification model used varies. The decomposition of multi-class classification problem into multiple binary classifications is attained through HAC. The classifier used for binary classification is SVM. Thus an algorithm which segments the Region Of Interest (ROI) is proposed using HAC based combined feature selection and classification. Comparison with conventional classifiers is carried out to reveal the efficiency of the proposed method.

7.3 Classification Refinement

Clinically it is seen that the brain tumour has the following pattern. A necrotic core followed by enhancing or non-enhancing tumour and an outer layer of edema. This knowledge is used to identify the misclassified pixels in the ROI which is segmented through the developed algorithm. This identification is made by generating an octonary tree for a particular pixel. The wrong sequences in the octonary tree are identified to compute the probability of misclassification of that pixel. Refinement is carried out and it is verified that the segmentation results are improved.

7.4 Research Contributions

1. Development of a new feature considering a fusion of multiple MRI modalities.

2. Development of a technique for combining feature selection and classification.

3. Development of a new supervised classifier for classifying multiple classes.

4. Development of a refinement technique for multi-class classification through wrong sequence identification.

5. Development of a new framework for the segmentation of brain tumour and its related sub-regions through fusion based methods.

6. Comparison of the developed method with state of the art methods.

7.5 Scope for Future Work

A few possible suggestions for future work are presented.

1. The work can be further extended to predict the nature of segmented tumour. Thus it may be possible to predict the survival rate of the patient using segmentation result.

2. The developed HAC based classifier can be applied for other classification problems involving multiple classes.

3. The developed refinement technique can be applied and verified for any other image segmentation problem if the sub-regions to be segmented follow a known pattern.

4. The developed HAC based classifier can be modified using some other classifier instead of SVM.

Appendix A

Illustration of MSPTF Algorithm

A.1 Distance Vector Calculation

The distances (intensity differences) of a pixel among the four modalities of MRI is calculated and a distance vector of size six is generated. Fig. A.1 shows the intensity differences of a Pixel $X_{i,j}$ in different MRI modalities. Pairwise distance between modalities are computed to get a six valued DV as depicted in Fig. A.2.

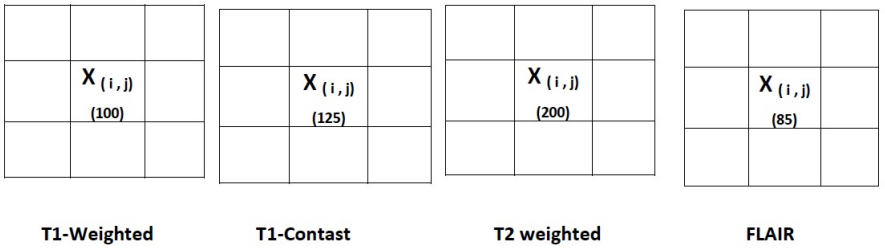

FIG. A.1. Intensities of a Pixel $X_{i,j}$ in Different MRI Modalities

-25	-100	+15	-75	+40	+115

FIG. A.2. DV of Pixel $X_{i,j}$ Calculated from Fig. A.1

A.2 Distance Vector Encoding

The DV in Fig. A.2 is encoded into a seven value vector using a lower threshold $\tau_1 = 20$, a middle threshold $\tau_2 = 50$ and an upper threshold $\tau_3 = 100$ to get an EDV. Encoding is done according to Equation A.1. EDV is shown in Fig. A.3.

$$EDV(i) = \begin{cases} 0, & \text{if } abs(DV(i)) < \tau_1 \\ +1, & \text{if } \tau_1 \leq DV(i) < \tau_2 \\ -1, & \text{if } \tau_1 \leq -(DV(i)) < \tau_2 \\ +2, & \text{if } \tau_2 \leq DV(i) < \tau_3 \\ -2, & \text{if } \tau_2 \leq -(DV(i)) < \tau_3 \\ +3, & \text{if } DV(i) \geq \tau_3 \\ -3, & \text{if } -(DV(i)) \geq \tau_3 \end{cases} \tag{A.1}$$

FIG. A.3. EDV of DV in Fig. A.2

A.3 Features from Encoded Distance Vector

The seven valued EDV in Fig. A.3 is decomposed into six vectors considering one value at a time and making others zero. The process is pictured in Fig. A.4.

1	0	0	0	0	0

Binary Vector for -1. All other Elements are made Zero

0	0	0	0	1	0

Binary Vector for +1. All other Elements are made Zero

0	0	0	1	0	0

Binary Vector for -2. All other Elements are made Zero

0	0	0	0	0	0

Binary Vector for +2. All other Elements are made Zero

0	1	0	0	0	0

Binary Vector for -3. All other Elements are made Zero

0	0	0	0	0	1

Binary Vector for +3. All other Elements are made Zero

FIG. A.4. Binary Vectors Corresponding to EDV in Fig. A.3

Appendix B

Learning Curves of Evolutionary Algorithms

B.1 Learning Curves of Genetic Algorithm

Based on the results obtained from HAC, Genetic Algorithm was executed to separate the classes through features. The learning curves of GA for separating the class pair (1,{5,2,3,4}) is shown in Fig. B.1. Fig. B.2 shows the GA learning curve for separating the class pair (5,{2,3,4}).

B.2 Learning Curves of PSO

Like GA, PSO was also executed to separate the classes through features. The learning curves of PSO for separating the class pair (1,{5,2,3,4}) is shown in Fig. B.3. Fig. B.4 shows the PSO learning curve for separating the class pair (5,{2,3,4}).

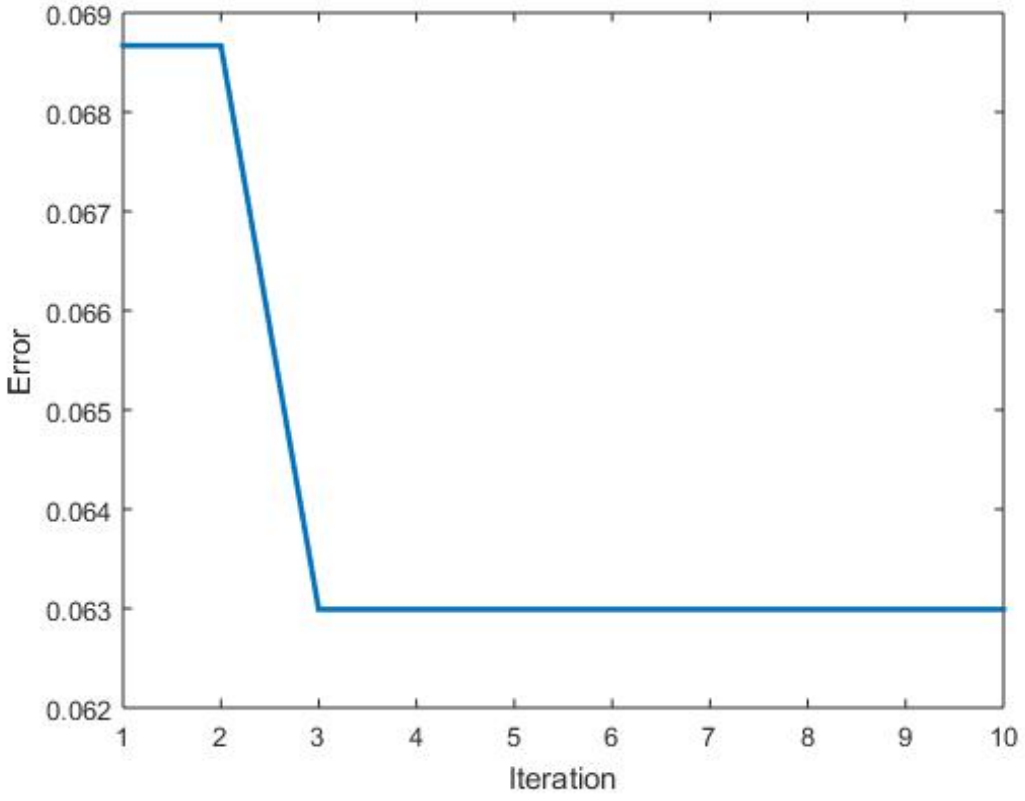

Fig. B.1. GA Learning for Separating Normal Class from Other Classes

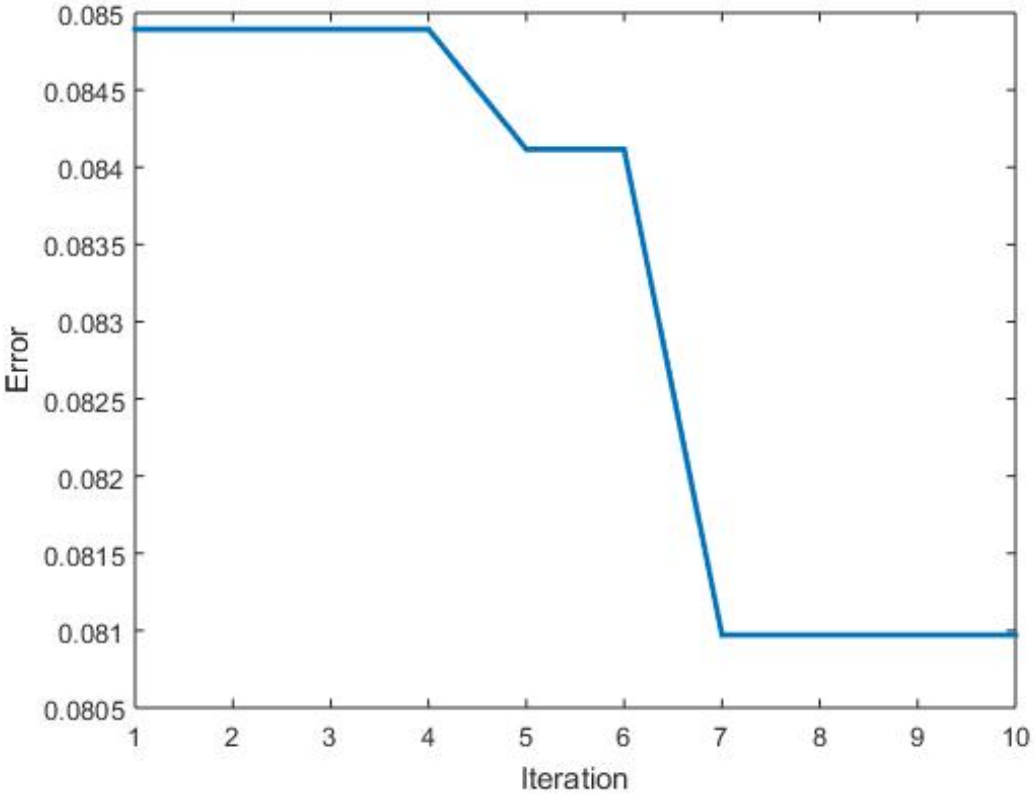

FIG. B.2. GA Learning Curve for separating ET Class from Other Affected Regions

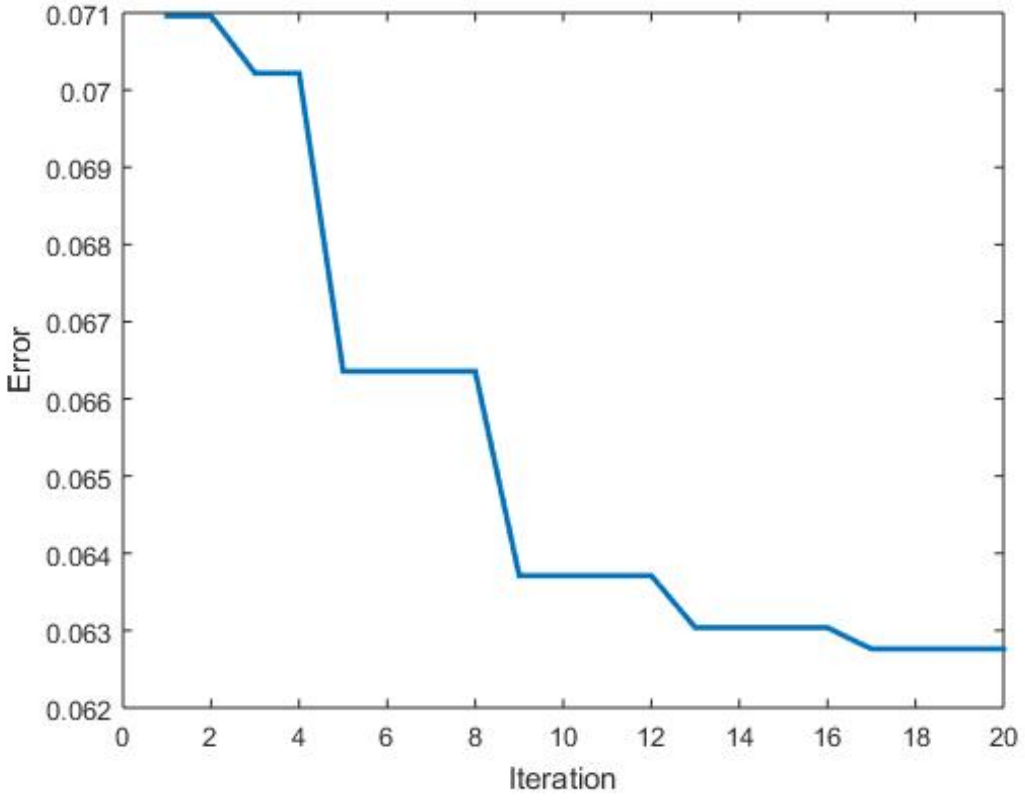

FIG. B.3. PSO Learning for Separating Normal Class from Other Classes

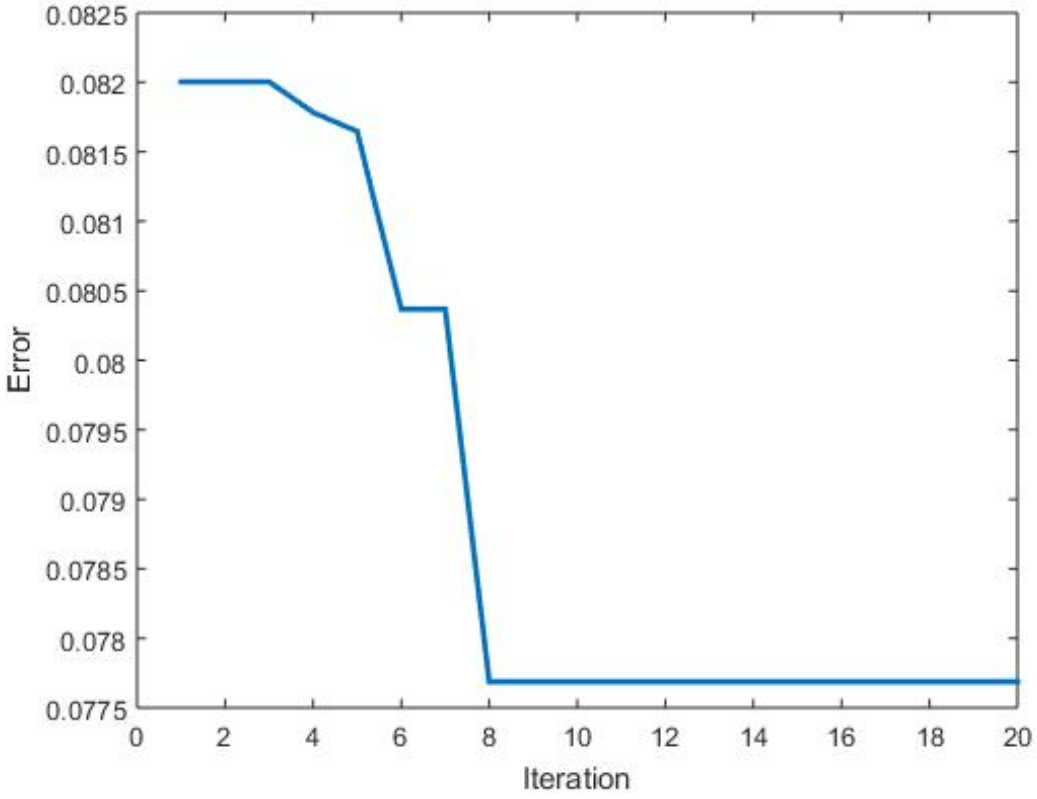

FIG. B.4. PSO Learning Curve for separating ET Class from Other Affected Regions

Appendix C

Wrong Sequence Identification in an Octonary Tree

C.1 List of All Possible Sequences

A list of all possible sequences of length 3 is shown in Table C.1. A knowledge about the nature of the sequence is also given in the table. The nature of the sequence depends on the pattern of occurrence of regions.

C.2 Sample Octonary Tree

A sample Octonary Tree with class labels are shown in Fig. C.1. The Wrong Sequences are marked in this figure. Here N-T-N is shown as a WS since the presence of tumour in between 2 normal pixels are not possible. For a similar reason N-T-E sequence is also considered as wrong.

Table C.1: List of All Possible Sequences of Length Three

No.	SEQUENCE	NATURE
1	N - N - N	Correct
2	N - N - E	Correct
3	N - N - T	Correct
4	N - E - N	Wrong
5	N - E - E	Correct
6	N - E - T	Correct
7	N - T - N	Wrong
8	N - T - E	Wrong
9	N - T - T	Correct
10	E - N - N	Correct
11	E - N - E	Wrong
12	E - N - T	Wrong
13	E - E - N	Correct
14	E - E - E	Correct
15	E - E - T	Correct
16	E - T - N	Wrong
17	E - T - E	Wrong
18	E - T - T	Correct
19	T - N - N	Correct
20	T - N - E	Wrong
21	T - N - T	Wrong
22	T - E - N	Correct
23	T - E - E	Correct
24	T - E - T	Wrong
25	T - T - N	Correct
26	T - T - E	Correct
27	T - T - T	Correct

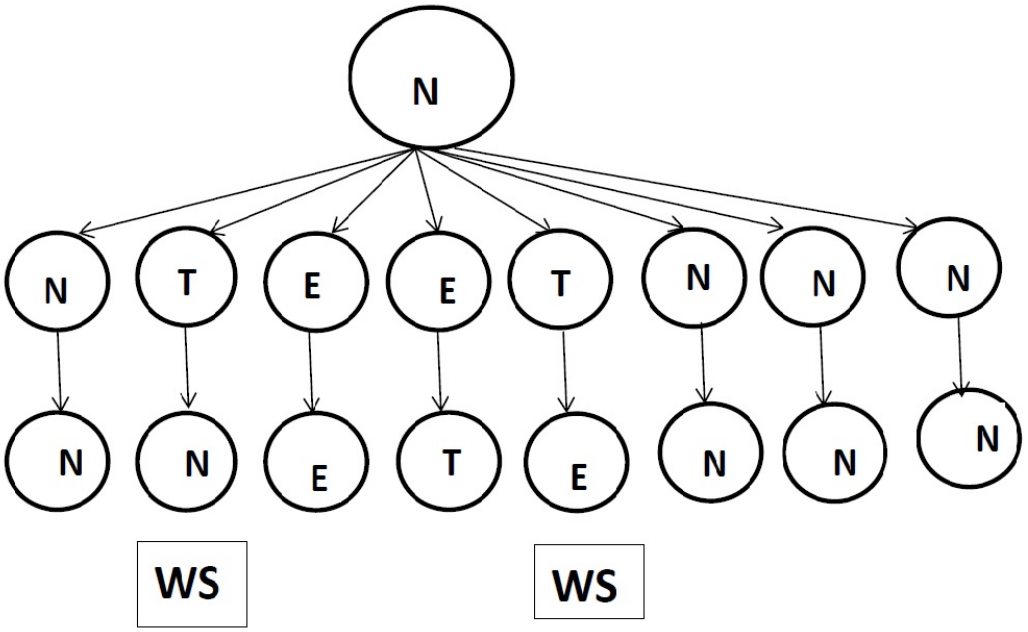

FIG. C.1. A Labelled Octonary Tree

Bibliography

[1] "Brain (Human Anatomy): Picture, Function, Parts, Conditions, and More", Jun 2019. URL https://www.webmd.com/brain/picture-of-the-brain#1. [Online; accessed 27. Jun. 2019].

[2] "Common Neurological Disorders | Norton Healthcare Louisville, Ky.", Jun 2019. URL https://nortonhealthcare.com/services-and-conditions/neurosciences/services/common-neurological-disorders. [Online; accessed 27. Jun. 2019].

[3] "About Cancer", Jul 2019. URL https://www.cancer.gov/about-cancer. [Online; accessed 28. Jul. 2019].

[4] T Haaga, CF Lanzieri, DJ Sartoris, EA Zerhouni, MA Rosenberg, R Schoenfeld, JK Amorosa, M Blacksin, and KC Cho. "Computed tomography and magnetic resonance imaging of the whole body". *AJR-American Journal of Roentgenology*, 165(4):884–885, 1995.

[5] "CT Scan Brain, Computed Tomography Scan Machine, GE CT Scanner Images", Jun 2019. URL http://www3.gehealthcare.in/en/products/categories/computed-tomography. [Online; accessed 27. Jun. 2019].

[6] Ronald Bracewell. *The Projection-Slice Theorem*, pages 493–504. Springer US, Boston, MA, 2003.

[7] "Computed Tomography (CT) | National Institute of Biomedical Imaging and Bioengineering", Jul 2019. URL https://www.nibib.nih.gov/science-education/science-topics/computed-tomography-ct#pid-1016. [Online; accessed 11. Jul. 2019].

[8] Catherine Westbrook and John Talbot. *MRI in Practice*. John Wiley & Sons, 2018.

[9] "MRI Machine stock illustration. Illustration of magnetic - 68441924", Jun 2019. URL https://www.dreamstime.com/stock-illustration-mri-machine-d-illustration-image68441924. [Online; accessed 27. Jun. 2019].

[10] "MRI Plane Mathematics", Jan 2018. URL https://my-ms.org/mri_planes.htm. [Online; accessed 27. Jun. 2019].

[11] "MRI Basics", May 2017. URL http://casemed.case.edu/clerkships/neurology/WebNeurorad/MRIBasics.htm.

[12] Marc C. Mabray, Ramon F. Barajas, Jr., and Soonmee Cha. "Modern Brain Tumor Imaging". *Brain Tumor Research and Treatment.*, 3(1):8–23, 2015.

[13] MC Papadopoulos, S Saadoun, DK Binder, GT Manley, S Krishna, and AS Verkman. "Molecular mechanisms of brain tumor edema". *Neuroscience*, 129(4):1009–1018, 2004.

[14] Jérôme Badaut and Nikolaus Plesnila. *Brain Edema: From Molecular Mechanisms to Clinical Practice*. Academic Press, 2017.

[15] Han Soo Chang. "Peritumoral edema". In *Meningiomas*, pages 565–571. Springer, 2009.

[16] Shaan M Raza, Frederick F Lang, Bharat B Aggarwal, Gregory N Fuller, David M Wildrick, and Raymond Sawaya. "Necrosis and glioblastoma: a friend or a foe? a review and a hypothesis". *Neurosurgery*, 51(1):2–13, 2002.

[17] Dorothy I Wallace and Xinyue Guo. "Properties of tumor spheroid growth exhibited by simple mathematical models". *Frontiers in Oncology*, 3, 2013.

[18] N Upadhyay and AD Waldman. "Conventional MRI evaluation of gliomas". *The British Journal of Radiology*, 84(special_issue_2):S107–S111, 2011.

[19] Neeraj Sharma and Lalit M Aggarwal. "Automated medical image segmentation techniques". *Journal of medical physics/Association of Medical Physicists of India*, 35(1):3, 2010.

[20] "Worldwide data — World Cancer Research Fund International", 2019. URL http://www.wcrf.org/int/cancer-facts-figures/worldwide-data.

[21] "Understanding Brain Tumors", Jun 2019. URL https://braintumor.org/brain-tumor-information/understanding-brain-tumors. [Online; accessed 27. Jun. 2019].

[22] "Cancer Statistics for the UK", May 2015. URL https://www.cancerresearchuk.org/health-professional/cancer-statistics-for-the-uk. [Online; accessed 11. Jul. 2019].

[23] Elisee Ilunga Mbuyamba, Juan Gabriel Avina-Cervantes, Arturo Garcia-Perez, Rene de Jesus Romero-Troncoso, Hugo Aguirre-Ramos, Ivan Cruz-Aceves, and Claire Chalopin. "Localized active contour model with background intensity compensation applied on automatic MR brain tumor segmentation". *Neurocomputing*, 220:84–97, 2017.

[24] Elisee Ilunga Mbuyamba, Juan Gabriel Avina-Cervantes, Jonathan Cepeda-Negrete, Mario Alberto Ibarra-Manzano, and Claire Chalopin. "Automatic selection of localized region-based active contour models using image content analysis applied to brain tumor segmentation". *Computers in Biology and Medicine*, 91:69–79, 2017.

[25] Chunming Li, Chiu-Yen Kao, John C Gore, and Zhaohua Ding. "Implicit active contours driven by local binary fitting energy". In *2007 IEEE Conference on Computer Vision and Pattern Recognition*, pages 1–7. IEEE, 2007.

[26] Li Wang, Lei He, Arabinda Mishra, and Chunming Li. "Active contours driven by local gaussian distribution fitting energy". *Signal Processing*, 89(12):2435–2447, 2009.

[27] Shawn Lankton and Allen Tannenbaum. "Localizing region-based active contours". *IEEE Transactions on Image Processing*, 17(11):2029–2039, 2008.

[28] Elisee Ilunga Mbuyamba, Jorge Mario Cruz-Duarte, Juan Gabriel Avina-Cervantes, Carlos Rodrigo Correa-Cely, Dirk Lindner, and Claire Chalopin. "Active contours driven by cuckoo search strategy for brain tumour images segmentation". *Expert Systems with Applications*, 56:59–68, 2016.

[29] V Rajinikanth, Suresh Chandra Satapathy, Steven Lawrence Fernandes, and S Nachiappan. "Entropy based segmentation of tumor from brain MR images–a study with teaching learning based optimization". *Pattern Recognition Letters*, 94:87–95, 2017.

[30] Andac Hamamci, Nadir Kucuk, Kutlay Karaman, Kayihan Engin, and Gozde Unal. "Tumor-cut: segmentation of brain tumors on contrast enhanced MR images for radiosurgery applications". *IEEE Transactions on Medical Imaging*, 31(3):790–804, 2011.

[31] P Shanthakumar and P Ganeshkumar. "Performance analysis of classifier for brain tumor detection and diagnosis". *Computers & Electrical Engineering*, 45: 302–311, 2015.

[32] Vasileios G Kanas, Evangelia I Zacharaki, Evangelos Dermatas, Anastasios Bezerianos, Kyriakos Sgarbas, and Christos Davatzikos. "Combining outlier detection with random walker for automatic brain tumor segmentation". In *IFIP International Conference on Artificial Intelligence Applications and Innovations*, pages 26–35. Springer, 2012.

[33] Leo Grady. "Random walks for image segmentation". *IEEE Transactions on Pattern Analysis and Machine Intelligence*, 28(11):1768–1783, 2006.

[34] Vasileios G Kanas, Evangelia I Zacharaki, Christos Davatzikos, Kyriakos N Sgarbas, and Vasileios Megalooikonomou. "A low cost approach for brain tumor segmentation based on intensity modeling and 3D random walker". *Biomedical Signal Processing and Control*, 22:19–30, 2015.

[35] Sima Taheri, Sim Heng Ong, and VFH Chong. "Level-set segmentation of brain tumors using a threshold-based speed function". *Image and Vision Computing*, 28(1):26–37, 2010.

[36] Jingxin Nie, Zhong Xue, Tianming Liu, Geoffrey S Young, Kian Setayesh, Lei Guo, and Stephen TC Wong. "Automated brain tumor segmentation using spatial accuracy-weighted hidden Markov random field". *Computerized Medical Imaging and Graphics*, 33(6):431–441, 2009.

[37] Hassan Khotanlou, Olivier Colliot, Jamal Atif, and Isabelle Bloch. "3D brain tumor segmentation in MRI using fuzzy classification, symmetry analysis and spatially constrained deformable models". *Fuzzy Sets and Systems*, 160(10): 1457–1473, 2009.

[38] Sérgio Pereira, Adriano Pinto, Victor Alves, and Carlos A Silva. "Brain tumor segmentation using convolutional neural networks in MRI images". *IEEE Transactions on Medical Imaging*, 35(5):1240–1251, 2016.

[39] Atiq Islam, Syed MS Reza, and Khan M Iftekharuddin. "Multifractal texture estimation for detection and segmentation of brain tumors". *IEEE Transactions on Biomedical Engineering*, 60(11):3204–3215, 2013.

[40] S Reza and Khan M Iftekharuddin. "Multi-fractal texture features for brain tumor and edema segmentation". In *Medical Imaging 2014: Computer-Aided Diagnosis*, volume 9035, page 903503. International Society for Optics and Photonics, 2014.

[41] Iván Cabria and Iker Gondra. "MRI segmentation fusion for brain tumor detection". *Information Fusion*, 36:1–9, 2017.

[42] Irem Ersoez Kaya, Ayça Çakmak Pehlivanlı, Emine Gezmez Sekizkardeş, and Turgay Ibrikci. "PCA based clustering for brain tumor segmentation of T1w MRI images". *Computer Methods and Programs in Biomedicine*, 140:19–28, 2017.

[43] Nooshin Nabizadeh and Miroslav Kubat. "Brain tumors detection and segmentation in MR images: Gabor wavelet vs. statistical features". *Computers & Electrical Engineering*, 45:286–301, 2015.

[44] Yuhong Li, Fucang Jia, and Jing Qin. "Brain tumor segmentation from multimodal magnetic resonance images via sparse representation". *Artificial Intelligence in Medicine*, 73:1–13, 2016.

[45] G Vishnuvarthanan, M Pallikonda Rajasekaran, P Subbaraj, and Anitha Vishnuvarthanan. "An unsupervised learning method with a clustering approach for tumor identification and tissue segmentation in magnetic resonance brain images". *Applied Soft Computing*, 38:190–212, 2016.

[46] Chih-Tang Chang, Jim ZC Lai, and Mu-Der Jeng. "A fuzzy k-means clustering algorithm using cluster center displacement.". *J. Inf. Sci. Eng.*, 27(3):995–1009, 2011.

[47] Stephen M Smith. "Fast robust automated brain extraction". *Human Brain Mapping*, 17(3):143–155, 2002.

[48] Solmaz Abbasi and Farshad Tajeripour. "Detection of brain tumor in 3D MRI images using local binary patterns and histogram orientation gradient". *Neurocomputing*, 219:526–535, 2017.

[49] Nicholas J Tustison, Brian B Avants, Philip A Cook, Yuanjie Zheng, Alexander Egan, Paul A Yushkevich, and James C Gee. "N4itk: improved n3 bias correction". *IEEE Transactions on Medical Imaging*, 29(6):1310–1320, 2010.

[50] Terry S Yoo, Michael J Ackerman, William E Lorensen, Will Schroeder, Vikram Chalana, Stephen Aylward, Dimitris Metaxas, and Ross Whitaker. "Engineering and algorithm design for an image processing api: a technical report on itk-the insight toolkit". *Studies in Health Technology and Informatics*, pages 586–592, 2002.

[51] Nobuyuki Otsu. "A threshold selection method from gray-level histograms". *IEEE Transactions on Systems, Man, and Cybernetics*, 9(1):62–66, 1979.

[52] Mohammad Havaei, Axel Davy, David Warde-Farley, Antoine Biard, Aaron Courville, Yoshua Bengio, Chris Pal, Pierre-Marc Jodoin, and Hugo Larochelle. "Brain tumor segmentation with deep neural networks". *Medical Image Analysis*, 35:18–31, 2017.

[53] Meiyan Huang, Wei Yang, Yao Wu, Jun Jiang, Wufan Chen, and Qianjin Feng. "Brain tumor segmentation based on local independent projection-based classification". *IEEE Transactions on Biomedical Engineering*, 61(10):2633–2645, 2014.

[54] Quratul Ain, M Arfan Jaffar, and Tae-Sun Choi. "Fuzzy anisotropic diffusion based segmentation and texture based ensemble classification of brain tumor". *Applied Soft Computing*, 21:330–340, 2014.

[55] E Candès, L Demanet, D Donoho, and L Ying. "Fast discrete curvelet transforms: Siam , 5,". *Multiscale Modeling and Simulation*, 5:861–899, 2006.

[56] Jianzhong Wang, Jun Kong, Yinghua Lu, Miao Qi, and Baoxue Zhang. "A modified FCM algorithm for MRI brain image segmentation using both local and non-local spatial constraints". *Computerized Medical Imaging and Graphics*, 32(8):685–698, 2008.

[57] Vida Harati, Rasoul Khayati, and Abdolreza Farzan. "Fully automated tumor segmentation based on improved fuzzy connectedness algorithm in brain MR images". *Computers in Biology and Medicine*, 41(7):483–492, 2011.

[58] Hongmin Cai, Ragini Verma, Yangming Ou, Seung-koo Lee, Elias R Melhem, and Christos Davatzikos. "Probabilistic segmentation of brain tumors based on multi-modality magnetic resonance images". In *Biomedical Imaging: From Nano to Macro, 2007. ISBI 2007. 4th IEEE International Symposium on*, pages 600–603. IEEE, 2007.

[59] Matthew C Clark, Lawrence O Hall, Dmitry B Goldgof, Robert Velthuizen, F Reed Murtagh, and Martin S. Silbiger. "Automatic tumor segmentation using knowledge-based techniques". *IEEE Transactions on Medical Imaging*, 17(2):187–201, 1998.

[60] C Jaspin Jeba Sheela and G Suganthi. "Automatic brain tumor segmentation from MRI using greedy snake model and fuzzy C-means optimization". *Journal of King Saud University-Computer and Information Sciences*, 2019.

[61] Marcel Prastawa, Elizabeth Bullitt, Sean Ho, and Guido Gerig. "A brain tumor segmentation framework based on outlier detection". *Medical Image Analysis*, 8(3):275–283, 2004.

[62] Ali Gooya, Kilian M Pohl, Michel Bilello, Luigi Cirillo, George Biros, Elias R Melhem, and Christos Davatzikos. "Glistr: glioma image segmentation and registration". *IEEE Transactions on Medical Imaging*, 31(10):1941–1954, 2012.

[63] Shaheen Ahmed, Khan M Iftekharuddin, and Arastoo Vossough. "Efficacy of texture, shape, and intensity feature fusion for posterior-fossa tumor segmentation in MRI". *IEEE Transactions on Information Technology in Biomedicine*, 15(2):206–213, 2011.

[64] T Ramakrishnan and B Sankaragomathi. "A professional estimate on the computed tomography brain tumor images using SVM-SMO for classification and MRG-GWO for segmentation". *Pattern Recognition Letters*, 94:163–171, 2017.

[65] Chaiyanan Sompong and Sartra Wongthanavasu. "An efficient brain tumor segmentation based on cellular automata and improved tumor-cut algorithm". *Expert Systems with Applications*, 72:231–244, 2017.

[66] Eman Abdel-Maksoud, Mohammed Elmogy, and Rashid Al-Awadi. "Brain tumor segmentation based on a hybrid clustering technique". *Egyptian Informatics Journal*, 16(1):71–81, 2015.

[67] Vasupradha Vijay, AR Kavitha, and S Roselene Rebecca. "Automated brain tumor segmentation and detection in MRI using enhanced Darwinian particle swarm optimization (EDPSO)". *Procedia Computer Science*, 92:475–480, 2016.

[68] Nooshin Nabizadeh, Nigel John, and Clinton Wright. "Histogram-based gravitational optimization algorithm on single MR modality for automatic brain lesion detection and segmentation". *Expert Systems with Applications*, 41(17): 7820–7836, 2014.

[69] Jason J Corso, Eitan Sharon, Shishir Dube, Suzie El-Saden, Usha Sinha, and Alan Yuille. "Efficient multilevel brain tumor segmentation with integrated bayesian model classification". *IEEE Transactions on Medical Imaging*, 27(5): 629–640, 2008.

[70] Abhishek Bal, Minakshi Banerjee, Amlan Chakrabarti, and Punit Sharma. "MRI brain tumor segmentation and analysis using rough-fuzzy C-Means and shape based properties". *Journal of King Saud University-Computer and Information Sciences*, 2018.

[71] Chao Ma, Gongning Luo, and Kuanquan Wang. "Concatenated and connected random forests with multiscale patch driven active contour model for automated brain tumor segmentation of MR images". *IEEE Transactions on Medical Imaging*, 37(8):1943–1954, 2018.

[72] Adel Kermi, Khaled Andjouh, and Ferhat Zidane. "Fully automated brain tumour segmentation system in 3D-MRI using symmetry analysis of brain and level sets". *IET Image Processing*, 12(11):1964–1971, 2018.

[73] Zhenyu Tang, Sahar Ahmad, Pew-Thian Yap, and Dinggang Shen. "Multi-atlas segmentation of MR tumor brain images using low-rank based image recovery". *IEEE Transactions on Medical Imaging*, 37(10):2224–2235, 2018.

[74] Isabelle Guyon, Steve Gunn, Masoud Nikravesh, and Lofti A Zadeh. *Feature extraction: foundations and applications*, volume 207. Springer, 2008.

[75] Robert M Haralick, Karthikeyan Shanmugam, *et al.* "Textural features for image classification". *IEEE Transactions on systems, man, and cybernetics*, 6: 610–621, 1973.

[76] Fritz Albregtsen *et al.* "Statistical texture measures computed from gray level coocurrence matrices". *Image Processing Laboratory, Department of Informatics, University of Oslo*, 5, 2008.

[77] Mary M Galloway. "Texture analysis using grey level run lengths". *NASA STI/Recon Technical Report N*, 75, 1974.

[78] Xiaoou Tang. "Texture information in run-length matrices". *IEEE Transactions on Image Processing*, 7(11):1602–1609, 1998.

[79] Joan S Weszka, Charles R Dyer, and Azriel Rosenfeld. "A comparative study of texture measures for terrain classification". *IEEE Transactions on Systems, Man, and Cybernetics*, (4):269–285, 1976.

[80] Kenneth I Laws. "Rapid texture identification". In *Image processing for missile guidance*, volume 238, pages 376–382. International Society for Optics and Photonics, 1980.

[81] Timo Ojala, Matti Pietikainen, and David Harwood. "Performance evaluation of texture measures with classification based on kullback discrimination of distributions". 1:582–585, 1994.

[82] T Yamasaki and K Aizawa. "Texture Classification Using Local Pattern Based on Vector Quantization". *IEEE Transaction on Image Processing*, 24(12):2006–2009, 2006.

[83] Chung-Ming Wu, Yung-Chang Chen, and Kai-Sheng Hsieh. "Texture features for classification of ultrasonic liver images". *IEEE Transactions on Medical Imaging*, 11(2):141–152, 1992.

[84] VL Jaya, Preetha Basu, and R Gopikakumari. "SMRT: A new placement approach of 2-d unique MRT coefficients for N a power of 2". In *India Conference (INDICON), 2012 Annual IEEE*, pages 233–237. IEEE, 2012.

[85] B Manju, VL Jaya, K Meenakshy, and R Gopikakumari. "8× 8 SMRT based texture descriptors". *Lecture Notes on Software Engineering*, 3(4):295, 2015.

[86] SN Sivanandam and SN Deepa. "Genetic algorithms". In *Introduction to genetic algorithms*, pages 15–37. Springer, 2008.

[87] SN Sivanandam and SN Deepa. *Principles of Soft Computing*. John Wiley & Sons, 2007.

[88] Padraig Cunningham and Sarah Jane Delany. "k-nearest neighbour classifiers". *Multiple Classifier Systems*, 34(8):1–17, 2007.

[89] Shigeo Abe. *Support vector machines for pattern classification*, volume 2. Springer, 2005.

[90] "BRATS - SICAS Medical Image Repository", Jul 2019. URL https://www.smir.ch/BRATS/Start2015. [Online; accessed 1. Jul. 2019].

[91] Gareth James, Daniela Witten, Trevor Hastie, and Robert Tibshirani. *An introduction to Statistical Learning*, volume 7. 2000.

[92] Konstantinos Kamnitsas, Wenjia Bai, Enzo Ferrante, Steven McDonagh, Matthew Sinclair, Nick Pawlowski, Martin Rajchl, Matthew Lee, Bernhard Kainz, Daniel Rueckert, *et al.* "Ensembles of multiple models and architectures for robust brain tumour segmentation". In *International MICCAI Brainlesion Workshop*, pages 450–462. Springer, 2017.

[93] Guotai Wang, Wenqi Li, Sébastien Ourselin, and Tom Vercauteren. "Automatic brain tumor segmentation using cascaded anisotropic convolutional neural networks". In *International MICCAI Brainlesion Workshop*, pages 178–190. Springer, 2017.

[94] Mina Rezaei, Konstantin Harmuth, Willi Gierke, Thomas Kellermeier, Martin Fischer, Haojin Yang, and Christoph Meinel. "A conditional adversarial network for semantic segmentation of brain tumor". In *International MICCAI Brainlesion Workshop*, pages 241–252. Springer, 2017.

List of Publications

Journal Publications

- Maya, U.C. and Meenakshy, K. "Hierarchical Agglomerative Clustering Based Combined Feature Selection and Multi-Class Support Vector Machine for Brain Tumour Classification". Journal of Medical Imaging and Health Informatics, 7(8), pp.1714-1722, 2017.

- Maya, U.C and Meenakshy, K. "Brain Tumor Segmentation Using Asymmetry Based Histogram Thresholding and K-Means Clustering." Int. Journal of Research in Eng. and Tech, 3(15), pp.62-65, 2014.

Conference Publication

- Maya, U. C., and K. Meenakshy. "Unified model based classification with FCM for brain tumour segmentation." 2015 IEEE International Conference on Power, Instrumentation, Control and Computing (PICC), GEC Thrissur, December 2015.